Advanced Composites and Hybrid Materials (2026) 9:159
https://doi.org/10.1007/s42114-026-01674-1

REVIEW

Zinc oxide photocatalysis for pollutant degradation: a review of elemental doping, morphology, and microstructure, integrated with machine learning-based performance modelling

Amir Hossein Navidpour[1,2] · Amir Dashti[1] · Ebrahim Alipanahpour Dil[2] · Peyman Asadi[3] · John L. Zhou[1,5] · Alireza Moshfegh[2,4] · Ali Altaee[1]

Received: 14 May 2025 / Revised: 23 January 2026 / Accepted: 29 January 2026

Abstract
ZnO nanoparticles are effective photocatalysts for the degradation of organic pollutants; however, there are gaps of knowledge about the effects of their morphology, microstructure, doping elements, and estimation of photocatalytic performance. Accordingly, the effects of morphology, microstructure, and elemental doping are reviewed first. Notably, ZnO microstructure is an important parameter influencing its photocatalytic performance. Specifically, the wurtzite phase, which is the most stable phase of ZnO, has been widely utilized in photocatalytic applications. However, the rocksalt phase of ZnO, a metastable phase, could exhibit higher photocatalytic activity than both wurtzite ZnO and anatase TiO_2. In addition to the review study, robust machine learning algorithms, including coupled simulated annealing-least square support vector machine, decision tree-particle swarm optimization, random forest- particle swarm optimization, and extreme gradient boosting-particle swarm optimization, were used to predict the photodegradation yield of various pollutants. The prediction is based on various parameters, including the molecular weight of the pollutants and dopants, topological polar surface area, hydrogen bond donor count, hydrogen bond acceptor count of the pollutants, initial concentration of pollutant, solution pH, light source, weight ratio of doping element to Zn, dosage of catalyst, and reaction time, using ZnO-based photocatalysts. A comprehensive dataset of 1176 entries was gathered from 22 different sources. To the best of our knowledge, for the first time in the field of photocatalysis, a web-based model using extreme gradient boosting-particle swarm optimization method has been developed in Python. This model can be easily accessed online to predict the photodegradation efficiency of various pollutants using ZnO-based photocatalysts.

Keywords Machine learning · Microstructure · Photocatalyst · Pollutant · ZnO

✉ John L. Zhou
john.zhou@nottingham.edu.cn

✉ Alireza Moshfegh
moshfegh@sharif.edu

[1] Centre for Green Technology, School of Civil and Environmental Engineering, University of Technology Sydney, Sydney, NSW 2007, Australia

[2] Department of Physics, Sharif University of Technology, Tehran 11155-9161, Iran

[3] Department of Medical Nanotechnology, School of Advanced Medical Sciences and Technologies, Shiraz University of Medical Sciences, Shiraz, Iran

[4] Center for Nanoscience and Nanotechnology - Institute for Convergent Science & Technology (ICST), Sharif University of Technology, Tehran 14588-8969, Iran

[5] Faculty of Science and Engineering, University of Nottingham Ningbo China, Ningbo 315100, China

1 Introduction

Environmental pollution and water shortage are two main global issues nowadays [1]. The application of semiconductor materials for organic pollutant degradation has rapidly attracted attention, due to the increased concern over the environmental issues [2]. Wastewater treatment processes are classified into physical, biological and chemical methods [3]. Notably, various methods like adsorption, separation, ozonation, clotting, chlorination, and chemical deposition are used for the treatment of industrial wastewaters [1], and each method has its own advantages and limitations. Physical treatments are usually considered phase changing technologies where pollutants are transferred from one phase to another [4], therefore, pollutant degradation

Published online: 11 March 2026

is still required [5]. Unlike physical methods, biological processes are capable of degrading organic wastes, but pH, temperature, and aeration for microbes should be optimized [5]. Although traditional biological processes are still used for the removal of pollutants, complete eradication of contaminants cannot be obtained using these methods [5]. Notably, treating large amount of organic matters with biological processes is relatively slow and difficult at low pH conditions [5]. It is well established that advanced oxidation processes (AOPs) have been successfully applied for industrial wastewater treatment [3, 6]. AOPs, which can enable bridging the gap between biological methods and common physicochemical processes, are considered one of the most efficient and appealing options for pollutant removal [5]. Noteworthily, they have been used for the elimination of pollutants from water [7]. Compared with custom treatment processes, sulfate and hydroxyl radicals, which could be produced by various AOPs, are the primary oxidants, resulting in the superiority of AOPs [8]. In general, heterogeneous and homogenous processes are considered two different types of AOPs [9]. Ozone oxidation, Fenton oxidation, electrochemical oxidation, photolysis, photocatalysis, sonolysis, and radiation are among different types of AOPs [7]. Solar energy is used for various applications like CO_2 photoreduction, decomposition of organic pollutants, nitrogen photo-fixation, photocatalytic water splitting, and photovoltaic technologies [10]. Semiconductor photocatalysis technology is considered an environmentally-friendly process that can take advantages of strong oxidation capacity and mild working conditions, introducing it as a potential alternative to traditional disinfection processes [11]. Moreover, it has been considered a promising strategy to convert photo energy into chemical energy [12, 13], where solar energy conversion using mild-light driven chemical reactions is of high importance to develop sustainable and green energy supply [14]. Production of photocatalysts with fine grains and high specific surface area could be considered the core of photocatalysis technology [15]. Despite several advantages of photocatalysis technology, photocatalysts could suffer from their low efficiency, high cost, and complexity [11]. An ideal photocatalyst requires features such as stability [16], strong solar light absorption [16, 17], and suitable redox potentials [16, 17]. Numerous metal oxides, including ZnO [18–21], TiO_2 [19, 21–24], CuO [25], Cu_2O [26], Fe_2O_3 [27, 28], ZrO_2 [29, 30], WO_3 [31–34], and SnO_2 [35], have been studied for photocatalytic applications, in addition to polymeric materials like g-C_3N_4 [36]. Due to their high efficiency, as well as technical and commercial aspects, TiO_2 and ZnO are the most commonly used semiconductors for dye degradation [37]. Owing to its high oxidation capacity and chemical stability, low toxicity, tunable size, and simple preparation, n-type ZnO is considered an effective photocatalyst for decomposition of organic contaminants [38]. In addition, it shows long-term photo-stability [39]. After iron oxide, ZnO is considered the most plentiful metal oxide [40]. Notably, ZnO has found numerous applications in UV detection, solar panels, ultraviolet resistant materials, fluorescent materials, light emitting diodes (LEDs), disinfection, targeted vectors, battery anodes, reinforcement (for resin composites, cement, and rubber), image recording, gas sensors, surface acoustic wave devices, varistors, supercapacitors, anti-wear and friction-reducing agents, antioxidant materials, and photocatalysis [41]. Overall, ZnO, with its wide direct band gap energy, is regarded as the second most widely used photocatalyst [42]. ZnO-based photocatalysts have been used for the degradation of numerous pollutants, including Orange G [43], Norfloxacin [44], Methylene Blue [45–51], Phenol [52, 53], Benzoic Acid [52], Methyl Orange [48, 54–56], Congo Red [48, 56], Rhodamine B [48], Malachite Green [57], Rose Bengal [51, 58], Bromocresol Green [51], Direct Black 38 [56], 2-Chlorophenol [59], Dichlorvos [60], Diazinon [61], Reactive Black 5 [62], Reactive Orange 4 [62], 2,4-Dichlorophenol [63], and Monocrotophos [64]. The widespread applications of ZnO are illustrated in Fig. 1.

A number of process parameters including the pollutant concentration, oxidizing agent, reaction temperature, photocatalyst concentration, light intensity, and pH of the solution have a substantial impact on the efficient photodegradation of organic pollutants in wastewater [45, 65, 66], and numerous studies have been conducted to determine the optimum circumstances of these parameters that allow for the organic pollutant photodegradation. For example, Sohrabi et al. [67] reported that the dose of the photocatalyst, phenol concentration, and contact time showed a significant influence on the photodegradation of phenol by Cu-doped TiO_2. After the process parameters optimization by response surface approach, phenol degradation efficiency reached 52.2% at optimum conditions of 158.75 mg L^{-1} of phenol, 0.52 g L^{-1} of photocatalyst and 179.50 min of reaction time. Another study reported that the oxidant concentration, initial phenol concentration, and photocatalyst loading influenced the usage of TiO_2/GAC photocatalyst for degradation of phenol in wastewater [68]. Using response surface methodology to optimize the process, 95.5% of phenol in the wastewater was degraded under optimum circumstances (326.90 mg L^{-1} for H_2O_2 concentration, 34.44 mg L^{-1} of initial phenol concentration). According to Chen et al. [69], Abdullah et al. [70], and Liu et al. [71], process parameter optimization can reveal the maximum degradation of different organic pollutants. However, there is a complex non-linear relationship among the process variables and their corresponding output in a real-life scenario (in a real-world setting). Experimental design cannot be used to study and investigate these complex non-linear relationships [72]. A powerful machine

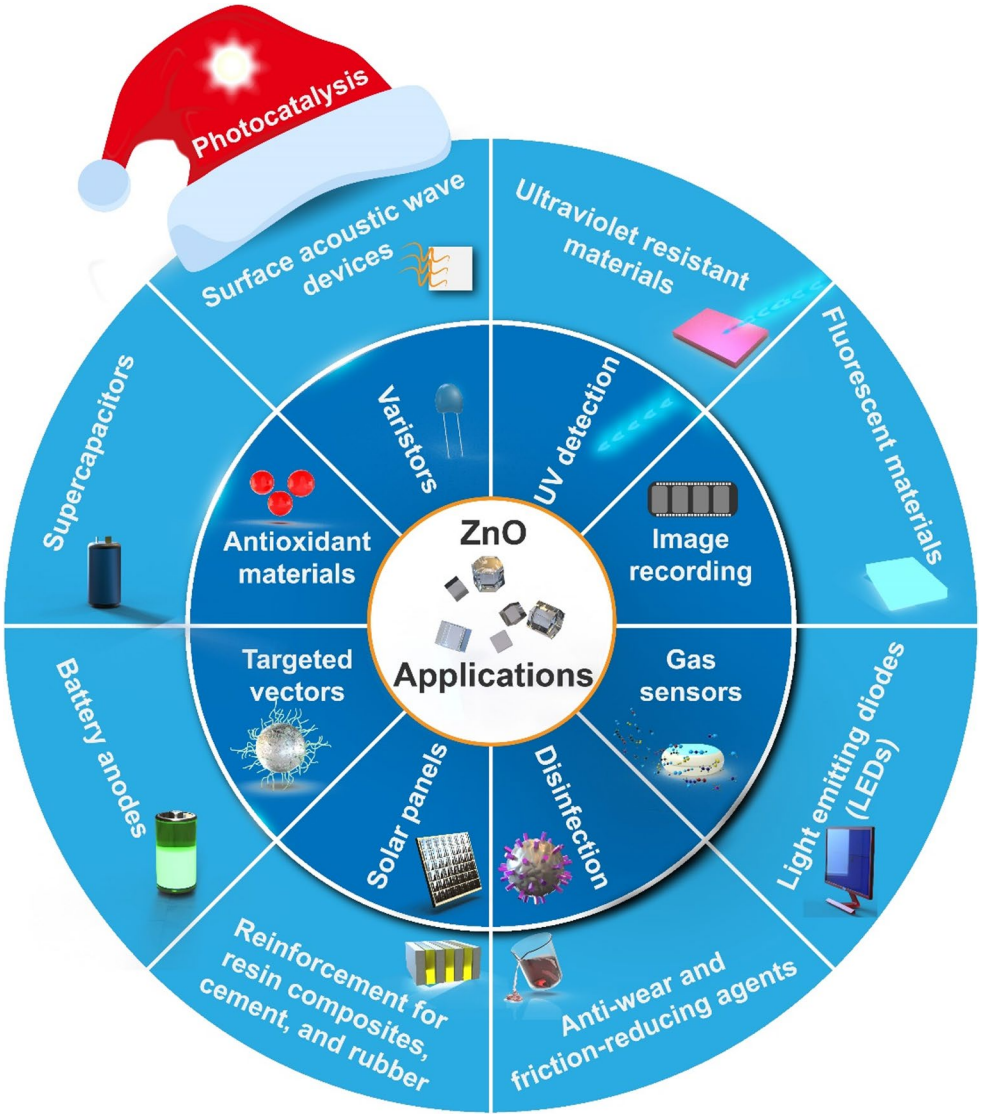

Fig. 1 Applications of ZnO in different technologies and industries

learning (ML) method for modeling the complex non-linear relationship among the process variables and their outputs is Artificial Neural Networks (ANN), which is less expensive, time-efficient, and rigorous than an experimental design [72]. Oladipo et al. [73] reported modeling and estimating degradation of organophosphorus pesticides in a binary and single system by using ANN.

ML algorithms are progressively used to improve waste management and support sustainable development since they are good at representing complex nonlinear processes [74, 75]. Large datasets can be processed by these algorithms, which can also discover previously hidden patterns and discernible relationships through conventional analytical techniques. Predictive models for wastewater treatment and waste management have frequently been developed using machine learning algorithms such as decision trees, support vector machines, artificial neural networks, and genetic algorithms [76–80]. Historical data on the performance of catalysts as well as other relevant variables like pH, temperature and pollutants concentration are used to train these models [76, 81–85]. Once trained, these models can precisely forecast how well organic pollutants would degrade catalytically, enabling engineers and researchers to optimize the design and selection of catalysts for effective treatment of wastewater [86–88].

There are several advantages by integrating ML algorithms with wastewater treatment procedures [89]. It could increase the effectiveness and overall efficiency of the treatment method, resulting in high rates of contaminant degradation. Additionally, ML algorithms can be applied to optimize wastewater treatment plant performance, and reduce operating expenses and energy consumption [90]. Furthermore, ML algorithms can offer insightful information on the dynamics and behavior of wastewater, facilitating improved waste management strategies and decision-making [91–96]. By supporting the adoption and

implementation of environmentally appropriate wastewater treatment practices, this combination also contributes to the advancement of ecological conservation [97]. ML algorithms can help to identify the best triggers, optimize their performance and reduce the impact of organic pollutants on the environment [85, 98–100]. ML approaches enable researchers to optimize and enhance photocatalytic degradation processes by using computational power to evaluate and analyze complicated data, making predictions and identifying patterns [97]. Consequently, ML approaches have been widely used in the field of photocatalysis. For instance, ML has been employed to accelerate the screening of effective metal oxides for photocatalytic water splitting [101]. In addition, Masood et al. [102] used ML to accelerate the discovery of solar photocatalysts. Moreover, chemical hardness-driven, interpretable ML algorithms were employed to identify the photocatalysts quickly [103]. Furthermore, Wang et al. [104] studied ML-assisted computational methods to screen 2D materials for photocatalytic water splitting. Wen et al. [105] studied the application of ML algorithms in designing single-atom catalysts, while Mai et al. [106] used ML for the quick design of photocatalysts based on Mn_3O_4. More specifically, ML models have found numerous applications in photocatalysis using various semiconductors (bare, doped, or composite) including TiO_2 [107, 108], ZnO [109–111], $BiVO_4$ [112], and g-C_3N_4 [113–115]. It is noteworthy that, in addition to photocatalysis, ML models have\ been applied to the design of metal oxide photoanodes for photoelectrochemical water splitting [116].

This article reviews the potential of ZnO semiconductor in photocatalytic applications with respect to its morphology and microstructure. In addition, it clarifies the capability of ML algorithms to predict the elimination of different types of organic pollutants under light irradiation using this prominent photocatalyst. In this study, ML algorithms of coupled simulated annealing-least square support vector machine (CSA-LSSVM), decision tree-particle swarm optimization (DT-PSO), random forest- particle swarm optimization (RF-PSO), and extreme gradient boosting-particle swarm optimization (XGB-PSO) were used to accurately estimate the removal of various pollutants using a ZnO photocatalyst, based on input parameters. The input parameters considered include the molecular weight (MW) of the pollutants and dopants (g/mol), topological polar surface area (TPSA, Å²), hydrogen bond donor count (HBDC), hydrogen bond acceptor count (HBAC) of the pollutants, initial concentration of pollutant (C_0, mg L^{-1}), solution pH, light source (UV or visible), weight ratio of doping element to Zn (Dopant/Zn), dosage of catalyst (mg L^{-1}), and reaction time (min). A user-friendly web-based application was developed that can be easily accessed online to predict the degradation of different pollutants using ZnO-based photocatalysts.

2 ZnO properties

It should be noted that large-scale water treatment using TiO_2 is not economical, whereas ZnO, with its lower price compared to TiO_2, could be considered a substantial alternative [117]. However, on the downside, photocorrosion under UV irradiation, resulted by the hybrid effect [118], and dissolution at high pH are among the drawbacks of ZnO [119]. Notably, TiO_2 and ZnO have comparable band gap energies [120]. Nevertheless, ZnO shows higher photo-absorption ability across a larger fraction of the solar spectrum [121]. In addition, ZnO possesses a higher electron mobility (200–300 $cm^2\ V^{-1}\ s^{-1}$) than TiO_2 (0.1–4.0.1.0 $cm^2\ V^{-1}\ s^{-1}$) [42]. ZnO, with its sufficient positive VB potential, is among promising semiconductors for photodegradation of organic pollutants via production of hydroxyl radicals [122]. Notably, commercial ZnO powder presented a higher photocatalytic activity than Degussa P25 TiO_2 for Acid Blue 14 degradation under solar light [123]. The main factors affecting the photocatalytic activity of ZnO-based photocatalysts are presented in Fig. 2. The features of ZnO are provided in detail in the following section.

Although the most common natural form of zinc is zinc sulfide (ZnS), ZnO is one of the most widely studied compounds in the experimental and computational material science [124]. Due to its direct wide band gap energy, approximately 3.3 eV at 300 K, zinc oxide is of high interest for optoelectronics applications. It has some applications in common with GaN which is a semiconductor with wide band gap energy of around 3.4 eV at 300 K. Notably, GaN is commonly used in the construction of green, white, and blue-ultraviolet light-emitting devices [125]. On the upside, its large exciton biding energy and the availability of bulk single crystals with high quality, have discriminated ZnO from GaN [125]. Pure ZnO is rarely observed in nature (as the mineral zincate), whereas ZnS is very common and generally appears as the mineral sphalerite [124]. Zinc oxide is odorless, insoluble in water, and has a bitter taste [126]. Notably, zinc oxide nanoparticles have attracted remarkable interest in different biomedical applications including antimicrobial, antibacterial, anticancer, antidiabetic, antioxidant, and anti-inflammatory activities [127]. They have also found applications in bioimaging, wound healing, food additives, and drug delivery [127]. It is considered that zinc oxide nanoparticles, below 100 nm, are relatively biocompatible [127, 128], bio-safe [128], and nontoxic [128]. Because of its promising features, such as wide and direct band gap energy, high photocatalytic performance, high free-exciton binding energy, and high oxidation capability, zinc oxide has received remarkable attention for photocatalytic purposes [126]. Moreover, it takes advantage of facile synthesis [129], facile doping processes [130], chemical and

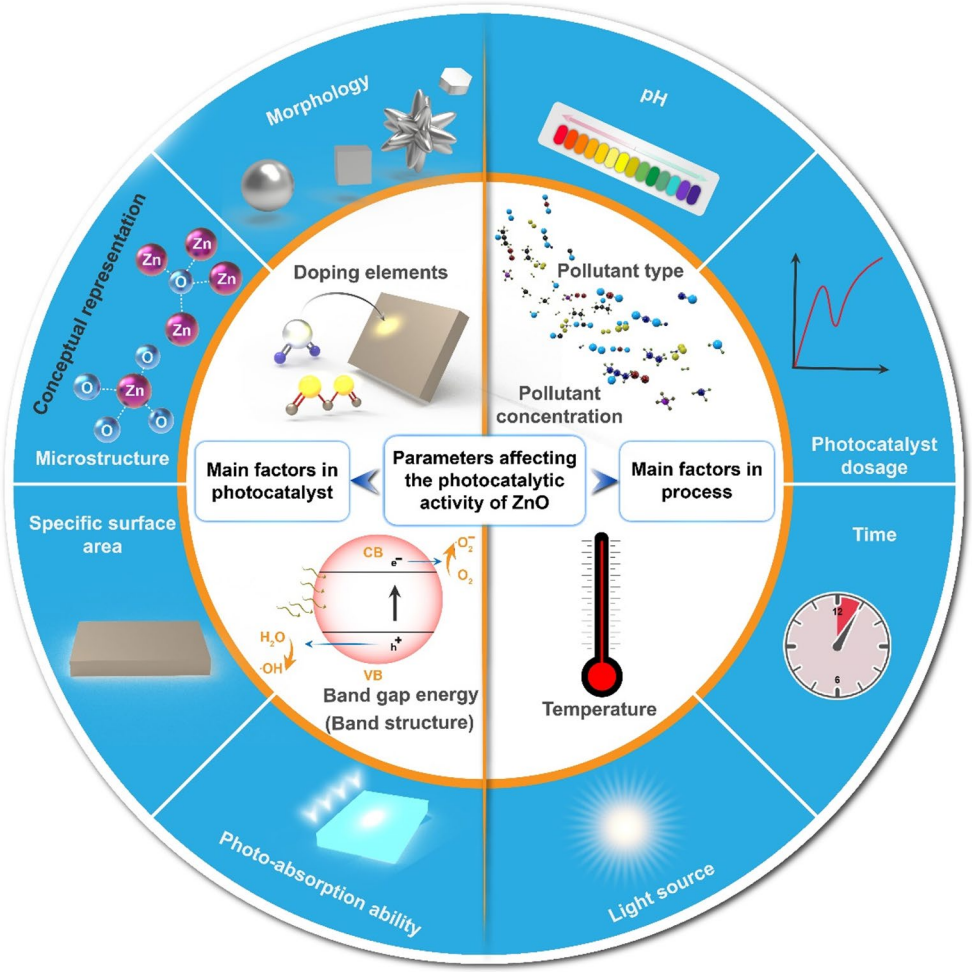

Fig. 2 Main parameters affecting the photocatalytic performance of ZnO-based photocatalysts

thermal stability [131], cost effectiveness [129], and non-hazardous nature [129]. However, lack of control over its electrical conductivity has resulted in the limited applications as a promising photoelectrode [126].

2.1 ZnO crystal structures

Zinc oxide can form three distinct crystal structures: wurtzite (hexagonal), zinc blende (cubic), and rocksalt (cubic) [126, 132]. Polarization force is among the main factors that could affect the crystal growth of zinc oxide during its synthesis [133]. In wurtzite ZnO, each Zn or O possesses four nearest neighbors [134]. Compared to the pristine rocksalt and zinc blende phases, wurtzite is the most stable phase of zinc oxide and the most often utilized polymorph for photocatalytic applications, benefiting from its simple manufacturing process [135]. Owing to its $P6_3mc$ space group, it possesses a lack of center of inversion symmetry that offers piezoelectricity in zinc oxide [134]. In some instances, wurtzite zinc oxide has demonstrated greater photocatalytic activity than TiO_2 [136–139]. However, the metastable phases of ZnO could be intriguing due to their unpredictable physical and chemical characteristics [135]. Thus, the photocatalytic properties of its metastable polymorphs are worth studying.

Notably, rocksalt ZnO should be synthesized at relatively high pressures; therefore, this polymorph is quite rare [126]. In rocksalt ZnO, each Zn or O possess six nearest neighbors [134]. The volume of rocksalt ZnO phase (B1) is about 18% smaller than that of wurtzite ZnO phase (B4) at ambient condition [140]. Besides, the band gap energy of rocksalt ZnO (1.2–2.6 eV) is lower than that of wurtzite ZnO [141]. The equilibrium transition pressure of the transformation of wurtzite ZnO to rocksalt ZnO is around 6 GPa [142, 143]. Notably, the transition pressure is dependent on both grain size and temperature [144]. Koster et al. [145] stated that the surface energy of rocksalt ZnO phase, 0.63 Jm^{-2}, is remarkably lower than that of zinc blend and wurtzite ZnO phases. They suggested that pure rocksalt ZnO phase could be stable in nanocrystals smaller than 1.6 nm. It has been shown that the addition of Mg can significantly enhance the range of stability of rocksalt ZnO phase [145]. It should be noted that metastable rocksalt $Me^{II}O$-ZnO solid solutions (Me^{II} = Co^{2+}, Fe^{2+}, Ni^{2+}, Mn^{2+}, and Mg^{2+}) with high content of ZnO (up to 0.8 molar fraction) could be recovered from 7 GPa

and 1400–1600 K owing to the stabilization effect of foreign cations. Due to the effect of grain size, using nanocrystalline wurtzite ZnO to synthesize rocksalt ZnO, necessitates the use of high pressures [144]. Surface energy discrepancy, ratio of volume collapse, and internal energy discrepancy could affect the transition pressure at nanocrystals (though at varying degrees), where Jiang et al. [146] showed that a high pressure of 15.1 GPa is required for the transformation of wurtzite ZnO to rocksalt ZnO, which has been mainly attributed to the remarkable contribution of surface energy. The reverse transition of microcrystalline rocksalt ZnO to wurtzite ZnO could occur at 2 GPa under decompression at room temperature that makes it impossible to maintain single phase of rocksalt ZnO [144].

Rocksalt ZnO is a metastable phase at ambient condition [135, 147, 148], and its photocatalytic activity has not been widely studied. High-Pressure Torsion (HPT) technique was employed by Razavi-Khosroshahi et al. [141] to create nanostructured rocksalt ZnO with a high density of oxygen vacancies. Phase diagram of ZnO, schematic image of HPT, and XRD patterns of samples (before and after HPT) are shown in Figs. 3**(a)–3(c)**. They concluded that the synthesized nanostructured rocksalt ZnO could be stable at ambient conditions even after 220 days, signifying the potential of using simultaneous pressure and strain for stabilization of this phase. The use of HPT technique could not only introduce rocksalt phase, but also create oxygen vacancies, as confirmed by the Raman spectra (Fig. 3**(d)**). Electron

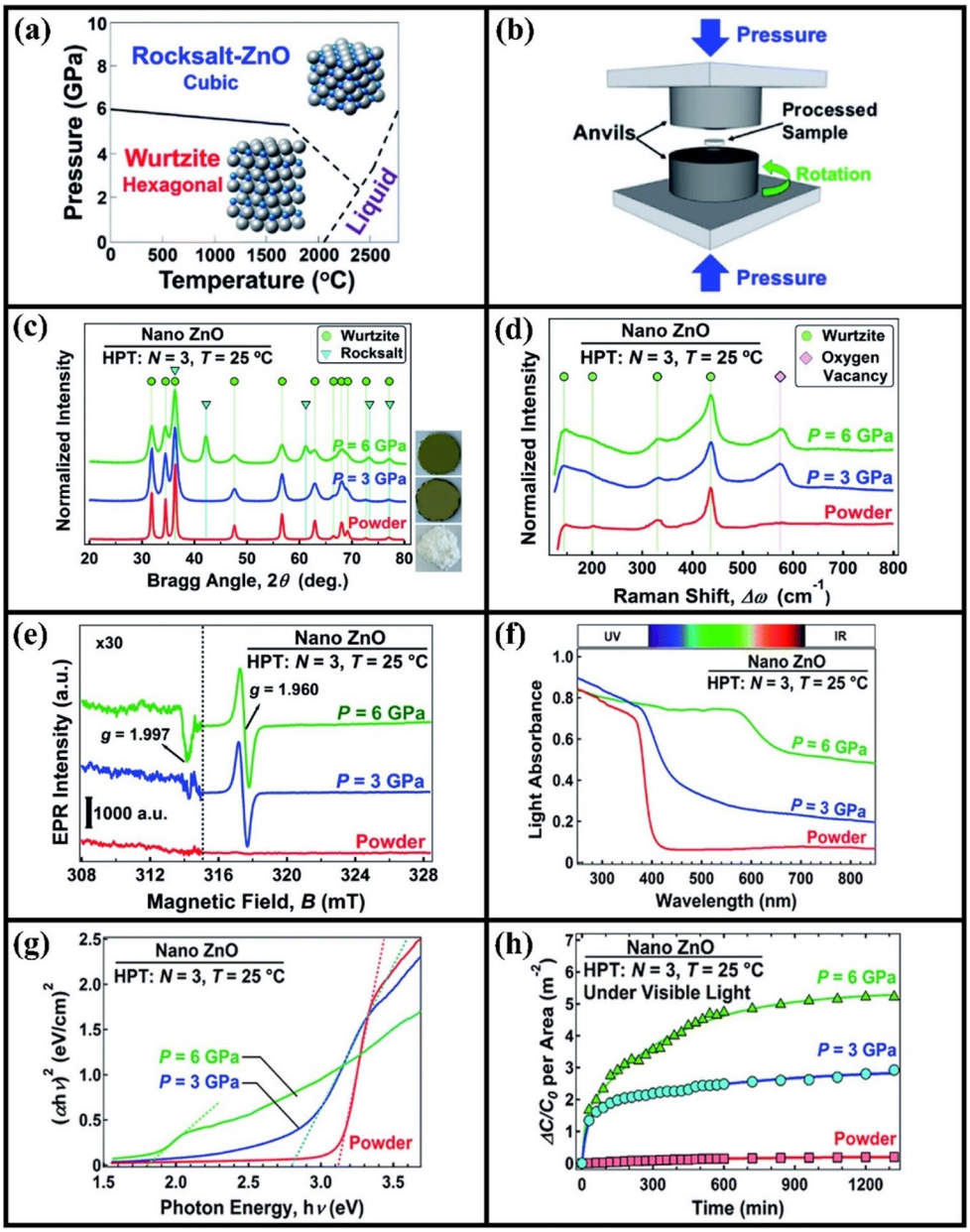

Fig. 3 (**a**) ZnO phase diagram, (**b**) schematic image of HPT, (**c**) XRD of samples (before and after HPT), (**d**) Raman spectra of ZnO (before and after HPT), (**e**) EPR spectra of ZnO (before and after HPT), (**f**) DRS spectra of ZnO (before and after HPT), (**g**) Calculation of band gap energies using Kubelka–Munk theory, and (**h**) photocatalytic activity of ZnO (before and after HPT) for RhB degradation under visible light (ΔC = amount of degradation of RhB, C_0 = initial concentration, N = turns of rotation of the lower anvil versus the upper one). Reproduced with permission from Ref. [141]. Copyright 2017 Royal Society of Chemistry (https://doi.org/10.1039/C7TA05262F)

Paramagnetic Resonance (EPR) spectra of samples (before and after HPT) are compared in Fig. 3**(e)**. Notably, unlike ZnO powder, two major g values of 1.960 and 1.997 were observed for the HPT-processed samples. Despite the uncertainty for the origin of the g value of 1.960, that of 1.997 is usually devoted to the presence of oxygen vacancies [141]. Photo-absorption ability of the initial wurtzite ZnO and the samples processed by HPT method under the pressures of 3 and 6 GPa are shown in Fig. 3**(f)**. With its high concentration of oxygen vacancies, it is evident that the sample treated at 6 GPa exhibited higher light-harvesting efficiency than the other samples. The comparison of the band gap energies for the samples is shown in Fig. 3**(g)**. Sample treatment under the pressure of 6 GPa exhibited the minimum band gap energy that could be originated from the high concentration of oxygen vacancies and formation of the rocksalt ZnO phase. Figure 3**(h)** compares the photocatalytic activity of the samples for Rhodamine B (RhB) degradation under visible light irradiation. The sample processed at 6 GPa exhibited the highest efficiency because of its high potential for light harvesting, the creation of the rocksalt ZnO phase, and the formation of oxygen vacancies. The rocksalt ZnO also showed higher photocatalytic activity than anatase TiO_2 and wurtzite ZnO. Overall, the stabilization of the rocksalt ZnO phase at ambient conditions using the HPT method, without the assistance of elemental doping, offers a potential plastic strain-induced pathway to remarkably narrow the wide band gap energy of pure ZnO, reaching as low as 1.8 eV, thereby enabling visible-light photocatalysis. Importantly, both the formation of the rocksalt phase and the presence of oxygen vacancies are responsible for the significant reduction in the band gap energy of ZnO samples processed by the HPT method [141].

Shundo et al. [149] stabilized oxygen vacancy-rich high-pressure ZnO rocksalt phase using an HPT method (300 K, 6 GPa) for photocatalytic production of H_2. The simultaneous effects of rocksalt phase and oxygen vacancies significantly increased photocatalytic H_2 production, due to active sites for photocatalysis and increasing light absorbance, clarifying the potential of high-pressure phases for photocatalytic H_2 production. Figure 4**(a-e)** shows TEM HR images of starting material (ZnO wurtzite nanopowder) and samples treated by the HPT method with 1/16, 1/4, 1, and 4 rotations, where the copresence of rocksalt and wurtzite ZnO phases was observed after severe HPT processing. The improved photocatalytic H_2 production of the sample prepared by the severe HPT treatment is shown in Fig. 4**(f)**. XPS spectra of Zn 2p, and O 1 s along with peak deconvolution are shown in Figs. 4**(g)** and **4(h)**, respectively. As evident, there is not any significant changes in the XPS spectra of Zn 2p before and after HPT treatment, but the XPS spectra of O 1 s obviously changes, where an increase in shoulder intensity at a higher energy level could signify an increase in the fraction of oxygen vacancy. Overall, the high-pressure phase of ZnO (i.e., the rocksalt phase), stabilized by the HPT method with the simultaneous introduction of oxygen vacancies, is considered very promising for improving the photocatalytic activity of ZnO (under ambient pressure) to levels comparable to that of P25 TiO_2, without adversely effecting charge carrier recombination [149].

The zinc blende ZnO crystal structure could be stabilized only when grown on cubic substrates [125]. Cubic zinc blende ZnO which has very similar physical properties and a close band gap energy to wurtzite ZnO could cover the same applications [150]. In general, zinc blende materials are completely covalent [134]. In zinc blende ZnO, each Zn or O possesses four nearest neighbors [134]. The total energy of zinc blende ZnO is higher than that of wurtzite ZnO by 50 meV, signifying the possibility of creating metastable zinc blende ZnO [134]. Zinc blende structure has higher crystallographic symmetry and lower ionicity, and is thus expected to have lower carrier scattering and higher doping efficiency [134]. Although various methods were used to synthesize pristine zinc blende ZnO, phase mixing is a strategy to improve the activity of a photocatalyst nanoparticle under visible light [135]. The band gap energy of ZnO phases ranged between 3.19 eV and 3.27 eV for zinc blend and wurtzite phases, respectively, restricting the application of ZnO when exposed to visible light [135]. Rajbongshi et al. [135] indicated the higher photocatalytic activity of biphasic Co-doped ZnO (with wurtzite and zincblende phases) than those of monophasic wurtzite ZnO (Co-doped and undoped) for the methylene blue and phenol degradation in the presence of visible light irradiation.

2.2 ZnO nanostructures and their photocatalytic applications

Nanostructures are highly important for photocatalytic purposes and are generally divided into three-dimensional (3D), two-dimensional (2D), one-dimensional (1D) and zero-dimensional (0D) nanostructures [151]. These major morphologies could be subdivided into ordered, planar, elongated, and quantum dot arrays, respectively [151]. In 0D nanostructures, all dimensions (x, y and z) are less than 100 nm and tunable optical properties and surface reactivity could be achieved using these materials [152]. Nanoparticles [153], nanospheres [154], quantum dots [153, 155], and fullerenes [153] are classified as 0D nanostructures. In 1D nanostructures, the dimensions in the x and y directions are less than 100 nm and unique electrical and mechanical properties could be offered using these materials [152]. Nanorods [153], nanofibers [153], nanowires [153, 156], nanotubes [153], nanohorns [153], and nanopillars [157]

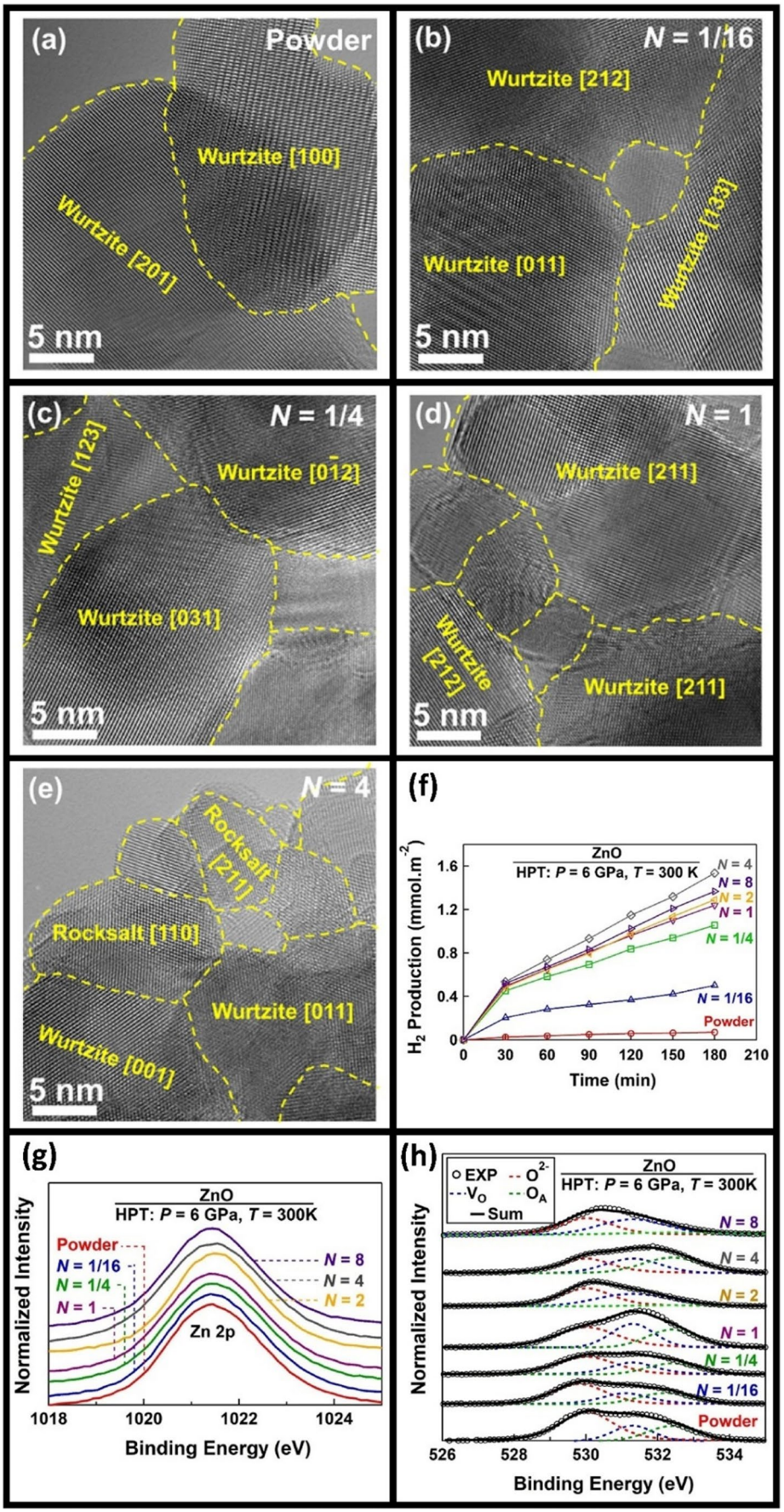

Fig. 4 TEM high-resolution images of (**a**) starting material and samples processed by HPT with (**b**) $N = 1/16$, (**c**) $N = 1/4$, (**d**) $N = 1$, and (**e**) $N = 4$ rotations. (**f**) Photocatalytic generation of H_2 per surface area of the starting powder and the samples processed by HPT with $N = 1/16$, 1/4, 1, 2, 4, and 8 rotations (under irradiation of Xe lamp). (**g**) XPS spectra of Zn 2p and (**h**) XPS spectra of O 1 s along with peak deconvolution for ZnO samples before and after the HPT process. Reproduced with permission from Ref. [149]. Copyright 2024 Elsevier

are classified as 1D nanostructures. A detailed review on 1D ZnO nanomaterials for photocatalysis is described [158]. In 2D nanostructures, only one dimension is less than 100 nm and exceptional mechanical strength and electrical conductivity could be introduced using these materials, such as graphene [152]. Nanosheets [153] and nanoplates [154] are classified as 2D nanostructures. In 3D nanostructures, all dimensions exceed 100 nm [152]. These nanomaterials exhibit hierarchical nanostructures that incorporate 0D, 1D and 2D architectures, enabling growth in all directions and leading to the development of multifunctional materials [152]. Notably, the method of preparation could highly affect the crystal structure of ZnO (cubic/hexagonal) and its morphology (nanotubes, nanobelts, nanorods, nanowires, disks, and flower-like) [159]. ZnO nanostructures have been synthesized in various architectures, ranging from 0D to 3D [152]. Nanoflowers, with several layers of petals and a structure resembling a plant flower on nm scale, are a type of tiny particles that provides a small structure with a large surface area. Effective charge transfer and high surface-to-volume ratios can lead to high surface reaction efficiency in the 3D structures such as nanoflowers [160]. Additionally, during photocatalysis, reduced nanoparticle agglomeration could occur [161]. Furthermore, compared to 0D and 1D nanostructures, 3D nanostructures could achieve improved photo-absorption ability. For instance, nanostar-like ZnO structures exhibited higher efficiency than ZnO nanorods and nanoparticles for MB degradation, owing to their improved photo-absorption ability (resulting from repeated photon scattering through the branches) and a higher number of active sites [162].

Mourya et al. [163] synthesized 3D hierarchical ZnO nanostructures with different morphologies (hollow spheres made up of nanowalls, nanospindles, nanoleaves, nanotetrapods, agglomerates of nanobuds, nanorods, nanocoral reefs, nanoflowers, and porous nanoflakes) for RhB photodegradation under UV irradiation. SEM images of the synthesized ZnO nanostructures with various morphologies (obtained using different zinc precursors, templates, and bases under microwave irradiation) and the photocatalytic activities of the calcined Z1-Z11 samples are shown in Fig. 5. Among these, ZnO with a nanotetrapod morphology (Z9) exhibited the highest photocatalytic activity (~99% in 100 min), whereas ZnO with a nanoflower morphology (Z3) decomposed approximately 83% of RhB within the same timeframe. Their findings demonstrated the crucial role of using a strong base (i.e., KOH) in combination with CTAB (as a template) to develop the tapered rod structure when using $ZnCl_2$ as the zinc precursor [163]. It has been stated that the exposure of [101] facet to large percentages could be accounted for the superior efficiency of Z9 sample compared to other ZnO nanostructures. The BET_{SSA} values of the Z1-Z11 samples were 54.52, 38.24, 58.11, 29.045, 38.670, 8.93, 19.69, 33.266, 19.752, 27.931, and 17.908 $m^2\ g^{-1}$, respectively [163]. The BET_{SSA} value of Z9 was lower than Z4, but the photocatalytic activity of Z9 was considerably higher than Z4. Overall, between surface area and crystallinity, the dominant factor influencing photocatalytic activity was crystallinity. The Z9 tetrapod showed the highest degradation rate despite having the lowest BET_{SSA}, clearly indicating that photocatalytic activity does not necessarily correlate with BET_{SSA}. This highlights the important role of morphology in photocatalysis, as the Z9 tetrapod achieved ~ 99% RhB degradation [163]. By performing scavenging experiments on Z9 sample, Mourya et al. [163] suggested that $^{\bullet}OH$ and $^{\bullet}O_2^-$ played a key role in RhB degradation.

Esbergenova et al. [162] synthesized nanostructured ZnO with three different morphologies (nanoparticles, nanostars, and nanorods) using hydrothermal method (without surfactants) via adjusting the ratio of $Zn(NO3)_2$•6 H_2O: KOH (Zn: KOH) to 1:2, 1:8, and 1:12. The probable growth mechanism of ZnO nanostructures at Zn: KOH ratios of 1:2, 1:8, and 1:12 is shown in Fig. 6**(a)**. The apparent rate constants of MB degradation under UV irradiation for ZnO nanoparticles, ZnO nanostars, and ZnO nanorods were 0.01193, 0.02994, and 0.00269 min^{-1}, respectively. The higher photocatalytic activity of ZnO nanostars was attributed to: (I) the generation of exposed (101) facets, resulting in a high number of defects related to oxygen vacancies; (II) the increase in photo-absorption ability due to multiple photon scattering inside the branches of nanostructured ZnO; and (III) the availability of numerous active sites gathered in a single structure. Noteworthily, compared to the (100) crystallographic plane, it has been suggested that the (101) crystallographic plane in the nanorod-like morphology of ZnO enabled the production of oxygen vacancy-related defects, by generating a shallow donor level below the CB of ZnO and capturing photogenerated electrons, which could facilitate the separation of charge carriers and improve the photocatalytic performance. Compared with ZnO nanoparticles and ZnO nanorods, the intensity of (101) reflection was more pronounced in the ZnO nanostars, as shown in the XRD patterns (Fig. 6**(b)**). The hydrothermal method used in this study to synthesize ZnO nanostructures without surfactants, by adjusting the ratio of $Zn(NO3)_2$•6 H_2O: KOH, enables the production of ZnO nanostructures with tunable morphologies and varying photocatalytic activities. Based on the scavenging experiments, hydroxyl radicals played a dominant role over photogenerated holes in MB degradation by ZnO nanostars. As confirmed by molecular dynamics simulation, the interaction of MB with an oxygen atom can result in the generation of OH groups in the molecule, enhancing its hydrophilicity. Additionally, this

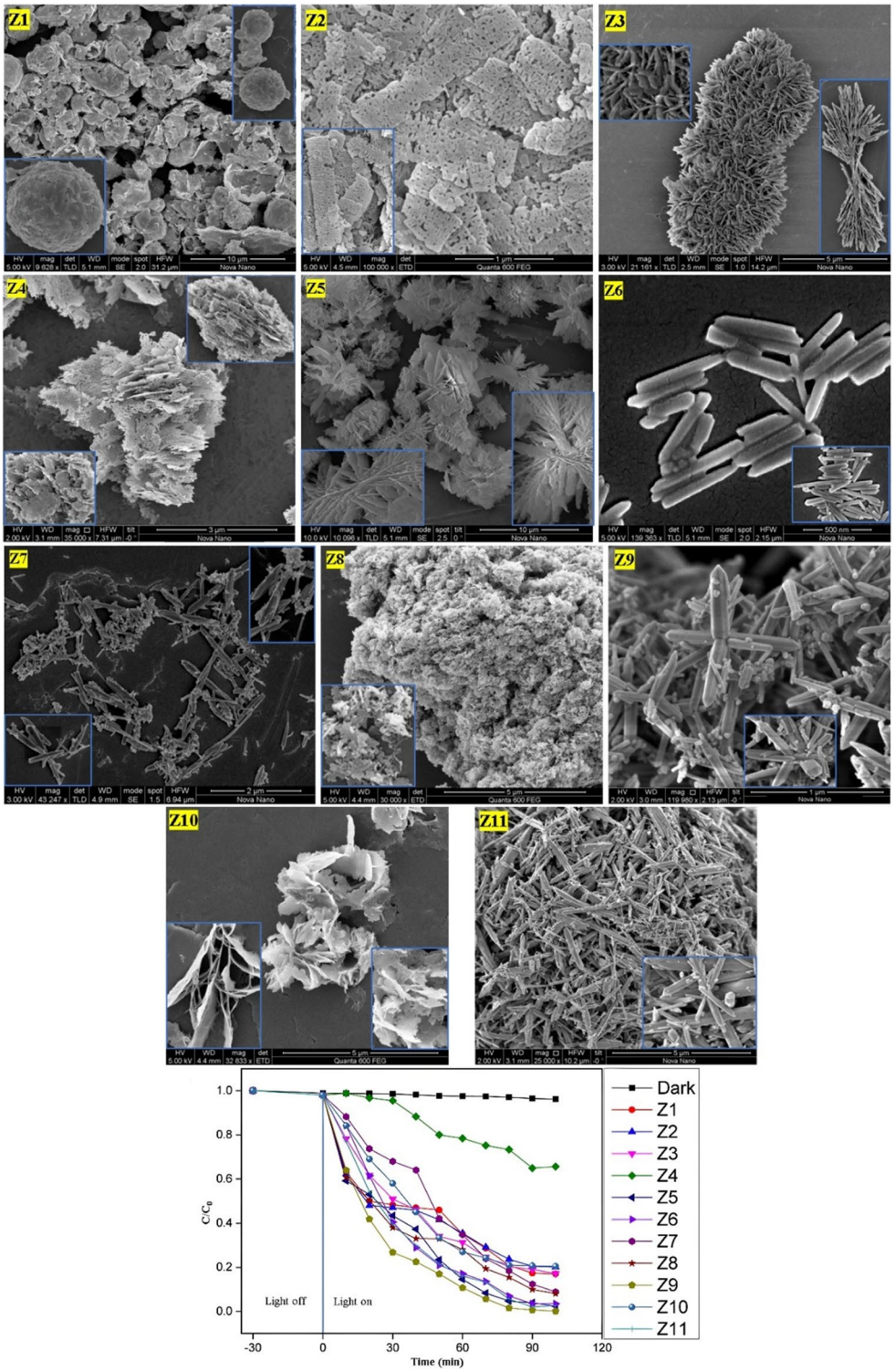

Fig. 5 SEM images of ZnO nanostructures: (Z1) Hollow spheres composed of nanowalls, (Z2) Porous nanoflakes, (Z3) Nanoflowers, (Z4) Nanocoral reefs, (Z5) Nanoflowers, (Z6) Nanorods, (Z7) Nanorods, (Z8) Agglomerates of nanobuds, (Z9) Nanotetrapods, (Z10) Nanoleaves, (Z11) Nanospindles; and the photocatalytic activity of calcined Z1-Z11 samples for decomposition of RhB. Reproduced with permission from Ref. [163] Copyright 2023 Elsevier

interaction could cause oxygen addition, ring expansion, or ring opening in MB, thereby contributing to its decolorization and degradation [162]. It should be noted that, in this context, the oxygen atoms were considered representative of hydroxyl radicals. The band-edge potentials of ZnO and MB photodecomposition by ZnO nanostars are shown in Fig. 6**(c)**.

Kedruk and coworkers [164] studied the morphology effect of different ZnO nanostructures (round-shaped nanoparticles, lamellar, and rods), produced by three low-cost and environmentally processes (direct thermal

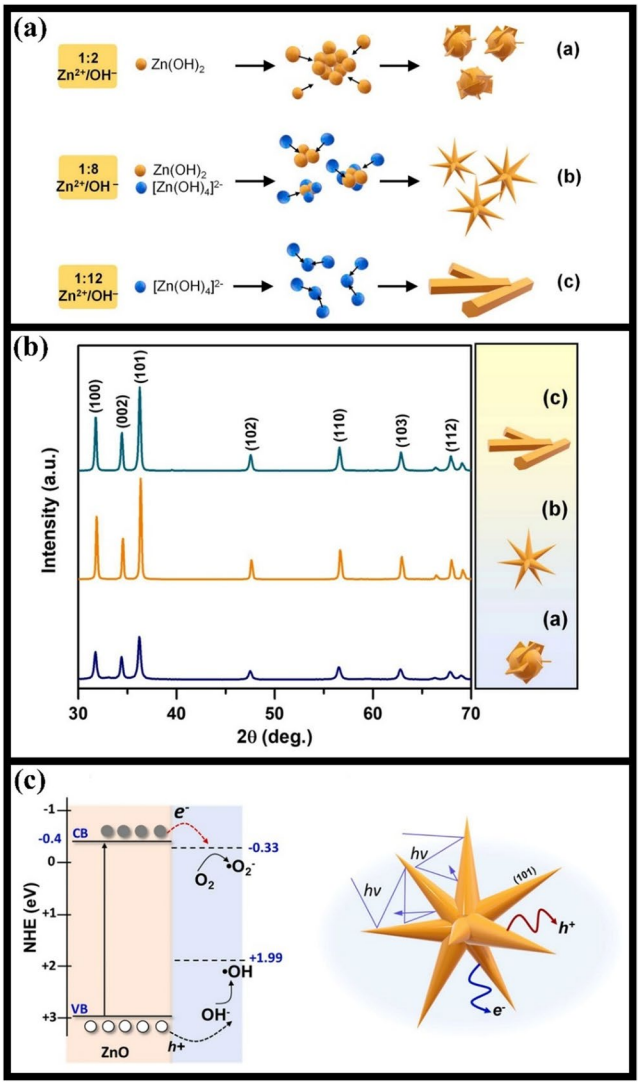

Fig. 6 (**a**) Schematic of the probable growth mechanism for nanostructured ZnO produced at different Zn: KOH ratios of 1:2, 1:8, and 1:12. (**b**) XRD patterns of nanostructured ZnO produced at different Zn: KOH ratios of 1:2, 1:8, and 1:12. (**c**) Schematic figure of the band-edge potentials of ZnO and MB photodecomposition over ZnO nanostars. Reproduced with permission from Ref. [162] Copyright 2023 Elsevier

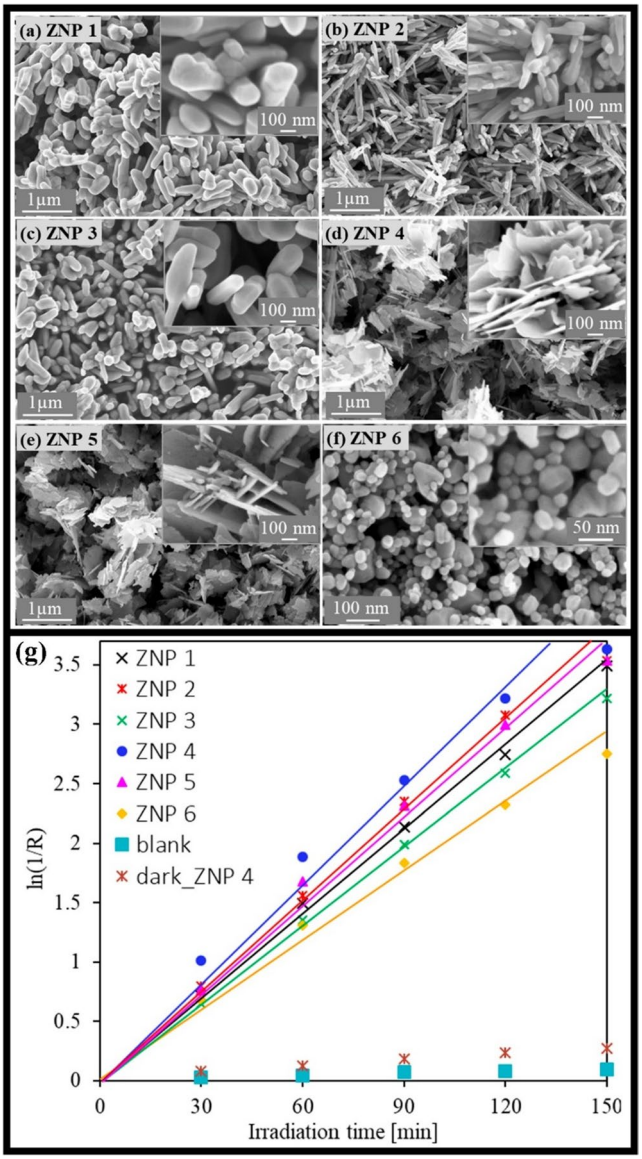

Fig. 7 FESEM images of (**a**) ZNP 1 (annealed at 700 °C for 10 h), (**b**) ZNP 2 (annealed at 400 °C for 10 h), (**c**) ZNP 3 (annealed at 700 °C for 6 h), (**d**) ZNP 4 (precipitation, [NaOH] = 0.4 M), (**e**) ZNP 5 (precipitation, [NaOH] = 0.7 M), and (**f**) ZNP 6 (microwave-assisted synthesis). (**g**) ln (1/R) against reaction time for the photocatalytic degradation of RhB under UV-vis irradiation (R stands for C/C_0). Reproduced with permission from Ref. [164] Copyright 2023 MDPI. This article is an open access article distributed under the terms and conditions of the Creative Commons Attribution (CC BY) license (https://creativecommons.org/licenses/by/4.0/)

decomposition method, low-temperature chemical precipitation, and microwave-assisted method), on the photocatalytic degradation of RhB and electrocatalytic reduction reaction of CO_2. ZnO samples with rod morphology, produced by direct thermal decomposition method, were denote as ZNP 1, ZNP 2, and ZNP 3. ZnO samples with lamellar morphology, produced by low-temperature chemical precipitation, were denote as ZNP 4 and ZNP 5. ZnO nanoparticles with round-shaped morphology were denoted as ZNP 6. FESEM analysis of the ZnO samples are shown in Fig. 7**(a-f)**, and the values of ln (C_0/C) versus t at different intervals for RhB photodegradation under UV-Vis irradiation over ZNP 1-ZNP 6 samples are shown in Fig. 7**(g)**. The aspect ratio (length/diameter) of ZNP 1, ZNP 2, ZNP 3, ZNP 4, ZNP 5 and ZNP 6 samples were 3.0, 9.2, 2.6, 38.2, 24.1 and 1 (spherical shape), respectively. Compared with ZnO nanorods and spherical ZnO nanoparticles, ZnO with a lamellar morphology showed the best performance in photocatalytic RhB degradation and electrocatalytic reduction of CO_2, due to the larger aspect ratio and greater number of active sites [164]. The trend in photocatalytic activity,

which closely correlates with the aspect ratio of ZnO nanostructures, highlights the key role of this morphological parameter in determining their photocatalytic activity. Interestingly, compared to the nanoparticle (ZNP 6) and nanorod (ZNP 1, ZNP 2, and ZNP 3) structures, ZnO electrodes with a lamellar structure (ZNP 4 and ZNP 5) exhibited significantly better performance in the electrocatalytic reduction reaction of CO_2, demonstrating the potential of lamellar ZnO nanostructures for both photocatalysis and CO_2 reduction reactions [164].

Altaf et al. [165] synthesized three different morphologies of ZnO (nano sponge (NS), nanoflower (NF), and nano urchin (NU)) using a mild hydrothermal method, which were then annealed at 300 °C, 600 °C and 800 °C (in air). SEM images of the synthesized ZnO nanostructures and the corresponding atomic percentages of Zn and O in the samples are shown in Fig. 8**(a)**, indicating that the amount of oxygen enhanced with increasing the temperature of annealing. As confirmed by electron paramagnetic resonance (EPR) measurements, the annealing temperature influenced core defect concentration; enhancing the annealing temperature from 600 °C to 800 °C significantly reduced core defect concentration, resulting in defect-free samples with improved homogeneity [165]. The apparent rate constants of RhB degradation under UV irradiation with respect to the morphology and the annealing temperature of ZnO samples are compared in Fig. 8**(b)**. Morphological changes remarkably affected the photocatalytic activity of the ZnO nanostructures, with ZnO NS exhibiting considerably higher performance than the others at different annealing temperatures of 300 °C, 600 °C, and 800 °C. Based on the scavenging experiments, regardless of the morphology of the ZnO nanostructures, O_2^- played a more dominate role than $^{\bullet}OH$ in RhB photodegradation process [165]. The average crystallite size and the full width at half maximum (FWHM) of ZnO samples, with respect to their morphology and annealing temperature, are presented in Fig. 8**(c)**. The FWHM decreased while the grain size increased with rising annealing temperature across different morphologies.

Leite et al. [44] examined the effect of precursor on hydrothermal synthesis of ZnO nanostructures for the UV photodegradation of antibiotic norfloxacin (NOR). It was shown that zinc precursor can significantly affect the morphology and size of ZnO nanostructures. Notably, various morphologies (e.g., nanogranules, ellipsoidal particles, and dumbbell-like structures) were achieved by varying the precursor of zinc in a mildly alkaline medium. The precursors used to synthesize ZnO nanostructures were zinc chloride, zinc nitrate hexahydrate, and zinc acetate dihydrate. The samples were labeled ZnO-Cl, ZnO-A, and ZnO-N to clarify the corresponding precursor. FESEM analysis of the synthesized ZnO nanostructures are displayed in Fig. 9**(a-f)**. Chloride, acetate, and nitrate precursors led to the creation of ZnO nanostructures with different morphologies of nanogranule, dumbbell-like, and ellipsoidal, respectively. The BET_{SSA} of ZnO-Cl, ZnO-A, and ZnO-N is compared in Fig. 9**(g)**. Notably, the smaller particle size of ZnO-Cl was associated with its greater BET_{SSA} than ZnO-N and ZnO-A samples. The photocatalytic activities of the ZnO-A, ZnO-Cl, and ZnO-N samples for NOR degradation at different catalyst dosages of 0.25, 0.5, and 1.0 g L^{-1} (pH 8 and initial concentration of 10 mg L^{-1}) are compared in Fig. 9**(h-j)**. Among the nanogranule, dumbbell-like, and ellipsoidal morphologies, ZnO nanogranules showed the best photocatalytic performance, achieving complete degradation of NOR within 70 min under UV-C irradiation. This superior activity is ascribed to the synergistic effects of a reduced recombination rate of charge carriers, a higher density of crystalline defects, and an enhanced surface area. The findings highlight the vital role of morphology in photocatalysis and emphasize the significant influence of the zinc precursor on the morphology and size of ZnO nanostructures synthesized via hydrothermal methods. It has been reported that chemical interactions between particles and ions considerably affect the adsorption of counterions along the particle growth direction, thereby affecting the morphology of ZnO nanostructures [44]. Compared to pH 6 and 10, the minimized electrostatic repulsion between the photocatalyst surface and the NOR molecule was suggested to contribute to the highest photocatalytic performance observed at this pH. It is notable that among $O_2^{\bullet-}$, $^{\bullet}OH$, e^-, and h^+, the greatest contribution to NOR degradation was attributed to $^{\bullet}OH$.

Fig. 8 (**a**) SEM images of the synthesized ZnO nanostructures and the corresponding atomic percentages of O and Zn. (**b**) Apparent rate constants of RhB degradation under UV irradiation depending on the morphology and annealing temperature of ZnO nanostructures. (**c**) FWHM and average crystallite size of ZnO nanostructures with respect to their morphology and annealing temperature. Reprinted with permission from Ref. [165] Copyright 2023 American Chemical Society (https://pubs.acs.org/doi/10.1021/acsomega.2c07412). Further permissions related to the material excerpted should be directed to the ACS.

2.3 Photocatalytic activity of doped ZnO

Element doping is considered an effective technique to increase the photocatalytic activity and/or improve the visible light absorption of semiconductors with wide band gap energies [166]. It has been stated that doping ZnO with nonmetals and metals can cause a red shift in its band gap energy, enabling visible light-activated photocatalysis [166]. Various metals and non-metals have been used as doping elements in ZnO [167], which are briefly discussed below.

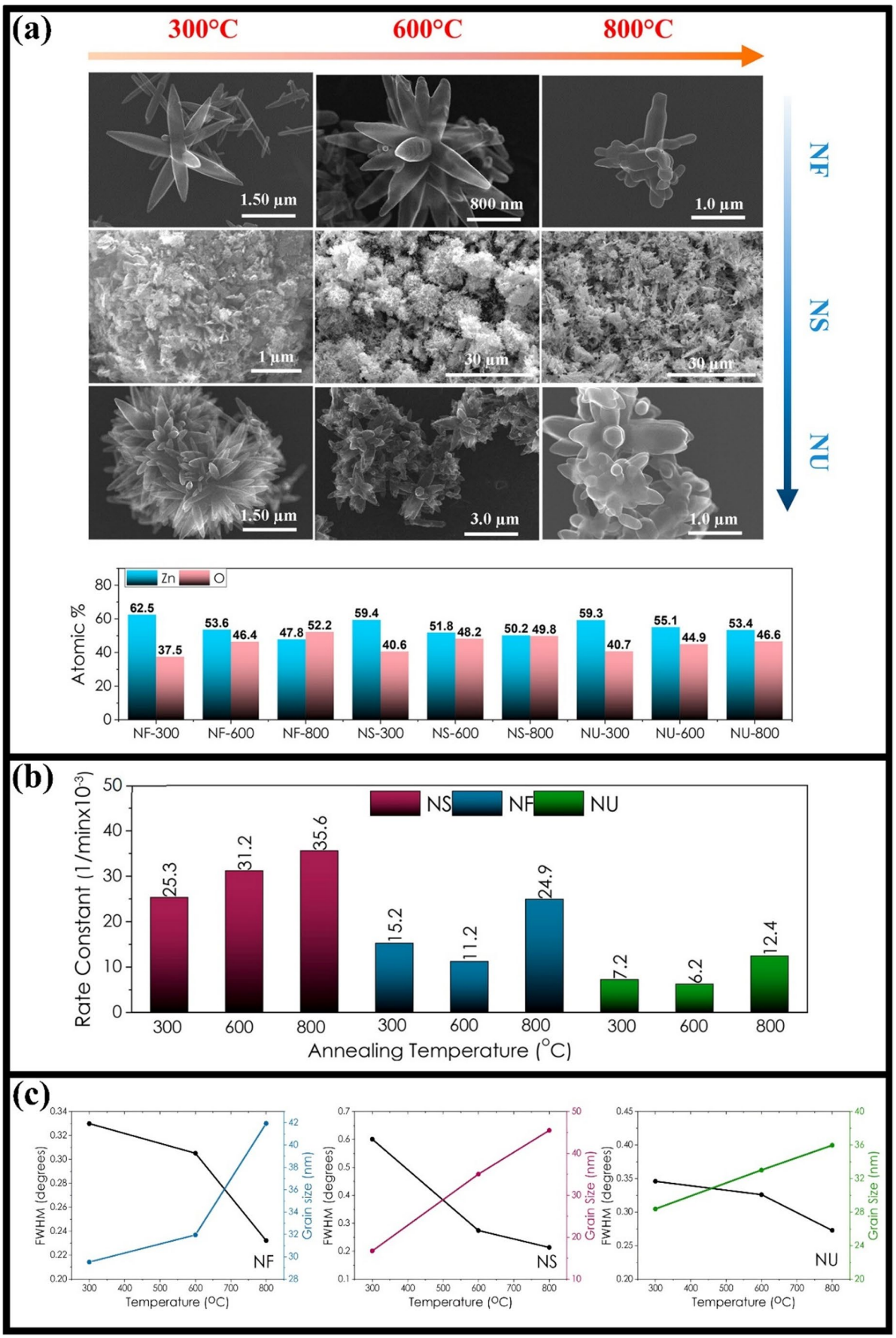
(a)
300°C
600°C
800°C
NF
NS
NU
1.50 μm
800 nm
1.0 μm
1 μm
30 μm
30 μm
1.50 μm
3.0 μm
1.0 μm
Zn
O
Atomic %
62.5
37.5
53.6
46.4
47.8
52.2
59.4
40.6
51.8
48.2
50.2
49.8
59.3
40.7
55.1
44.9
53.4
46.6
NF-300
NF-600
NF-800
NS-300
NS-600
NS-800
NU-300
NU-600
NU-800
(b)
Rate Constant (1/minx10-3)
NS
NF
NU
25.3
31.2
35.6
15.2
11.2
24.9
7.2
6.2
12.4
Annealing Temperature (°C)
(c)
FWHM (degrees)
Grain size (nm)
NF
NS
NU
Temperature (°C)

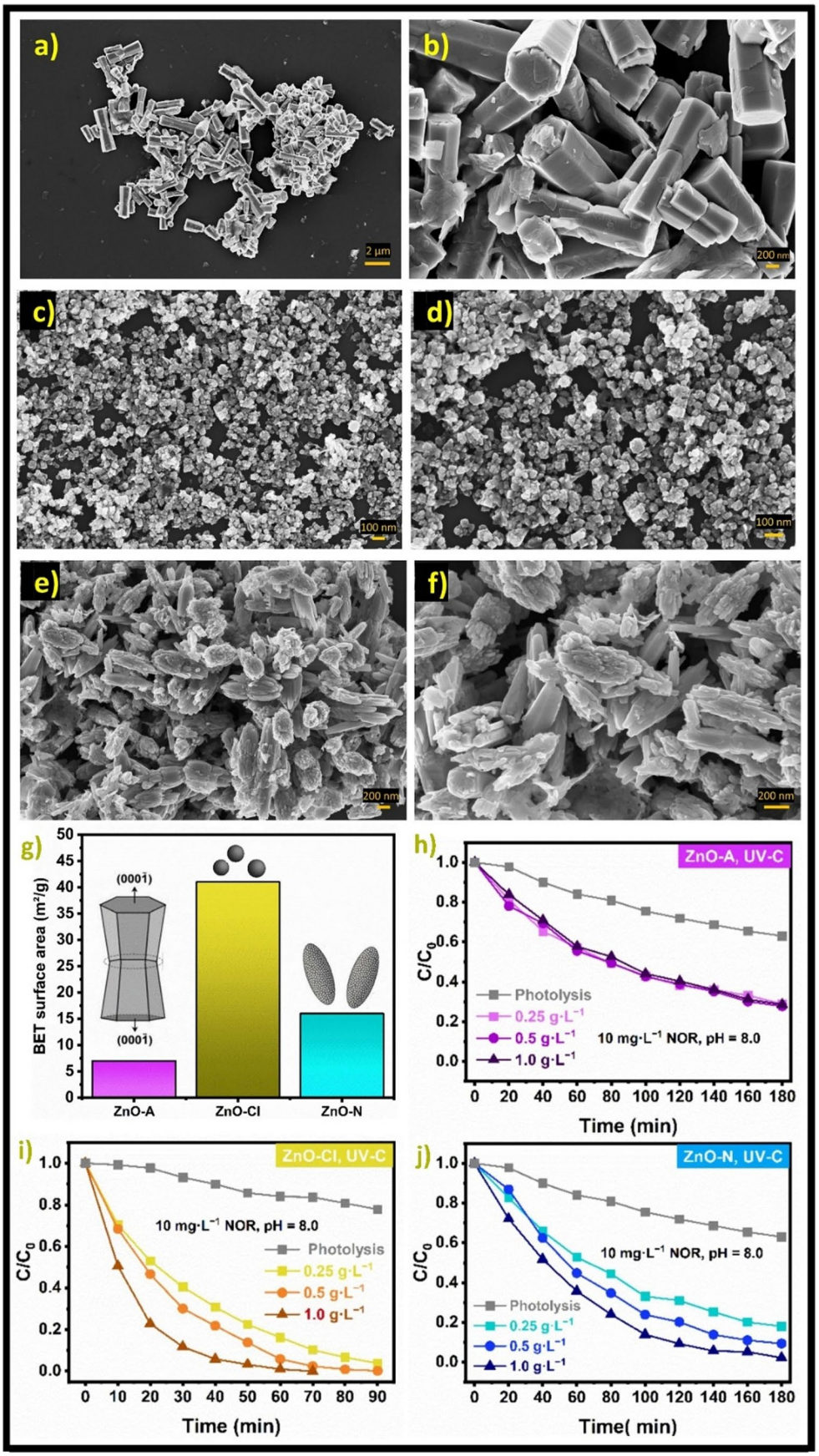

Fig. 9 FESEM images of (**a**, **b**) ZnO-A, (**c**, **d**) ZnO-Cl (**e**, **f**), and ZnO-N. (**g**) BET_{SSA} of ZnO-A, ZnO-Cl, and ZnO-N samples. Photocatalytic activity of (**h**) ZnO-A, (**i**) ZnO-Cl, and (**j**) ZnO-N for NOR degradation under UV-C irradiation at different catalyst dosages of 0.25 g L^{-1}, 0.5 g L^{-1}, and 1.0 g L^{-1} (C_0 = 10 mg L^{-1}, pH 8). Reproduced with permission from Ref. [44] Copyright 2024 Elsevier

2.3.1 Transition metal doped-ZnO

Low separation efficiency of charge carriers and low visible light absorption are among the disadvantages of ZnO as a potential photocatalytic material [126, 168]. Samadi et al. [169] synthesized MWCNT-doped ZnO electrospun nanofibers for the photocatalytic degradation of MB under both visible and UV irradiation. In addition to MWCNTs, metal doping of ZnO at an optimized level enhanced the lifetime of charge carriers by development of trapping cites [170]. Different transition metal dopants including Cu [171–173], Ni [174–176], Mn [177–179], Cr [180–183], Fe [184–186], Nb [187–189], and Co [190–192] have been used for metal doping of ZnO. Overall, substitution of Zn^{2+} ions with the transition metal ions could narrow the band gap energy of ZnO as the result of sp-d exchange interactions between d electron of transition metals and conduction band electrons of ZnO (4s4p orbitals) [193]. Some features of Mn and Co have enhanced their use for doping into ZnO lattice structure (compared with other transition metal elements) [194]. It has been shown that Mn doping of ZnO can drive visible light activated ZnO [179, 195, 196]. Moreover, Mn^{2+} ionic radius (0.80 ˚A) is near that of Zn^{2+} (0.74 ˚A); thus, Mn doping does not result in significant distortion of ZnO lattice structure [179]. In addition to Mn^{2+}, substitution of Zn^{2+} with Co^{2+} ions could lead to the creation of strong absorption peaks in the visible region [190]. Qiu et al. [197] observed a remarkable decrease in the band gap energy of ZnO by Co doping, as the ionic radius of Zn^{2+} is bigger than that of Co^{2+} that facilitates Co doping into the lattice of ZnO [192]. In addition to the approximate similarity of ionic radius, the covalent radii of Co^{2+} (1.16 ˚A) and Mn^{2+} (1.17 ˚A) are close to that of Zn^{2+} (1.25 ˚A) [194]. Notably, incorporation of transition metal cations into ZnO lattice could result in the formation of oxygen vacancies that could promote the separation efficiency of photo-induced e^-/h^+ pairs [192]. Li et al. [194] synthesized ZnO nanowires doped by Co or Mn for the photodegradation of methyl orange under visible light irradiation. SEM images of undoped ZnO (Fig. 10**(a**, **b)**), ZnO doped by Mn (Fig. 10**(c**, **d)**) and Co (Fig. 10**(e**, **f)**); and EDX spectra of ZnO doped by Mn (Fig. 10**(g)**) and Co (Fig. 10**(h)**) are displayed in Fig. 10. The atomic percentages of Co and Mn in the doped ZnO were 1.68% and 6.29%, respectively. Thus, incorporation of Mn was easier than that of Co into ZnO lattice structure. Moreover, the morphology of ZnO nanowires was not affected by Co or Mn doping; however, the doping significantly influenced the nanowire diameter, with diameters of approximately 80 nm and 200 nm for Mn-doped and Co-doped ZnO, respectively. Light-harvesting efficiency, band gap energy, photoluminescence spectra, and the photocatalytic activity of Co-doped ZnO, Mn-doped ZnO, and undoped ZnO are presented in Fig. 10**(i-l)**. As shown in Fig. 10**(i)**, both ZnO doped by Co and Mn provided higher photo-absorption ability than undoped ZnO. Compared to ZnO doped by Mn, ZnO doped by Co showed higher photo-absorption ability. Figure 10**(j)** confirms the narrowed band gap energy of ZnO by Co or Mn doping. Although the atomic percentage of Co was lower than that of Mn, it is obvious that doping of Co^{2+} ions could have more effect than Mn^{2+} ions on the optical properties of ZnO [194]. Overall, compared to undoped ZnO, both Co- and Mn-doped ZnO nanowires can present higher photocatalytic activity, as a result of their high photo-absorption capability and low rate of photoexcited charge carrier recombination. The incorporation of impurity energy levels within the ZnO band gap, resulting from Co^{2+} and Mn^{2+} doping, can modify the energy band structure of ZnO, promote the separation of charge carriers, and accelerate the production of reactive radicals ($O_2^{\bullet-}$ and $^{\bullet}OH$) for photocatalysis [194].

2.3.2 Rare Earth metal doped-ZnO

Various rare earth metal elements including Sm [198–200], Er [201–203], Nd [204–206], Ce [207–210], La [64, 211], Yb [212], Pr [213–215], Dy [216, 217], and Eu [54, 218–220] have been used as doping elements for ZnO photocatalyst. In addition to photocatalysis, metal-doped ZnO (such as Ce-doped ZnO) has been used for photoelectrochemical applications [221]. Alam et al. [216] synthesized La-, Nd-, Dy- and Sm-doped (1 at%) ZnO nanoparticles for MB and RhB photodegradation under UV photoirradiation. XRD patterns of pure ZnO and ZnO doped with rare earth metal are compared in Fig. 11**(a**, **b)**. The red shift observed for rare earth metal doped-ZnO could be related to the expansion of the unit cell due to the mismatch of ionic radii and/or incorporation of metals into the lattice structure of ZnO [216]. Figure 11**(c**, **d)** displays the TEM and HRTEM images of Nd-doped ZnO nanoparticles, synthesized using a simple sol-gel technique, where the plane of (101) of ZnO nanoparticles could be allocated to the lattice fringe with the inter-planar distance of 0.26 nm [216]. Figure 11**(e-h)** indicates light-harvesting efficiency, band gap energy, PL spectra, and photocatalytic efficacy of ZnO nanoparticles doped with rare earth metals. All ZnO nanoparticles doped with rare earth metal indicated higher photo-absorption ability than pure ZnO that could be correlated with the formation of impurity energy levels between the conduction and valence bands of ZnO (Fig. 11**(e)**). Notably, the maximum and minimum band gap energies are attributed to pure ZnO (3.25 eV) and Dy-doped ZnO (3.17 eV). ZnO nanoparticles doped with Nd exhibited the highest activity for both MB and RhB photodegradation, achieving approximately 98% MB and 88% RhB degradation within 25 min. In addition,

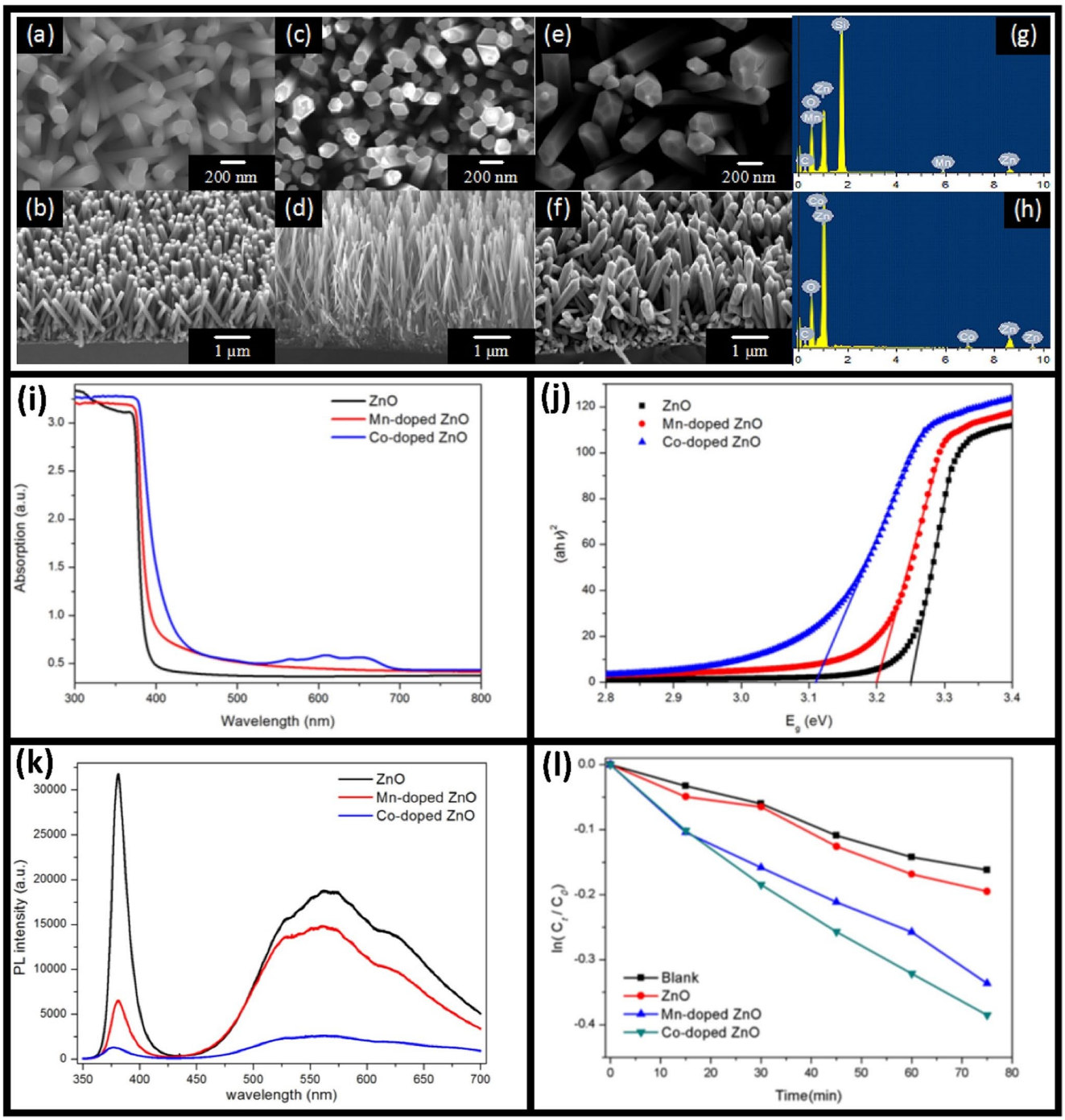

Fig. 10 SEM images from the top and the side view of (**a**, **b**) ZnO nanowires, (**c**, **d**) Mn-doped ZnO nanowires, and (**e**, **f**) Co-doped ZnO nanowires. EDX spectra of (**g**) Mn-doped ZnO and (**h**) Co-doped ZnO. (**i**) DRS spectra, (**j**) Estimated band gap energies, (**k**) PL spectra, and (**l**) photocatalytic activity of ZnO, Mn-doped ZnO, and Co-doped ZnO. Reproduced with permission from Ref. [194]. Copyright 2017 MDPI. This article is an open access article distributed under the terms and conditions of the Creative Commons Attribution (CC-BY) license (http://creativecommons.org/licenses/by/4.0/)

it exhibited 68% MB mineralization, as confirmed by TOC measurements (pH 10, t = 3 h, MB concentration = 100 ppm, and catalyst dosage = 4 g L^{-1}). Notably, Nd doping considerably increased the surface area from 30.31 m^2 g^{-1} for pure ZnO to 140.9 m^2 g^{-1} for the Nd-doped ZnO nanoparticles. Thus, the participation of Nd could enhance the adsorption of pollutants on the photocatalyst surface, leading to improved photocatalytic performance. Reusability experiments demonstrated the potential of rear earth metal-doped ZnO nanoparticles for MB degradation with good stability

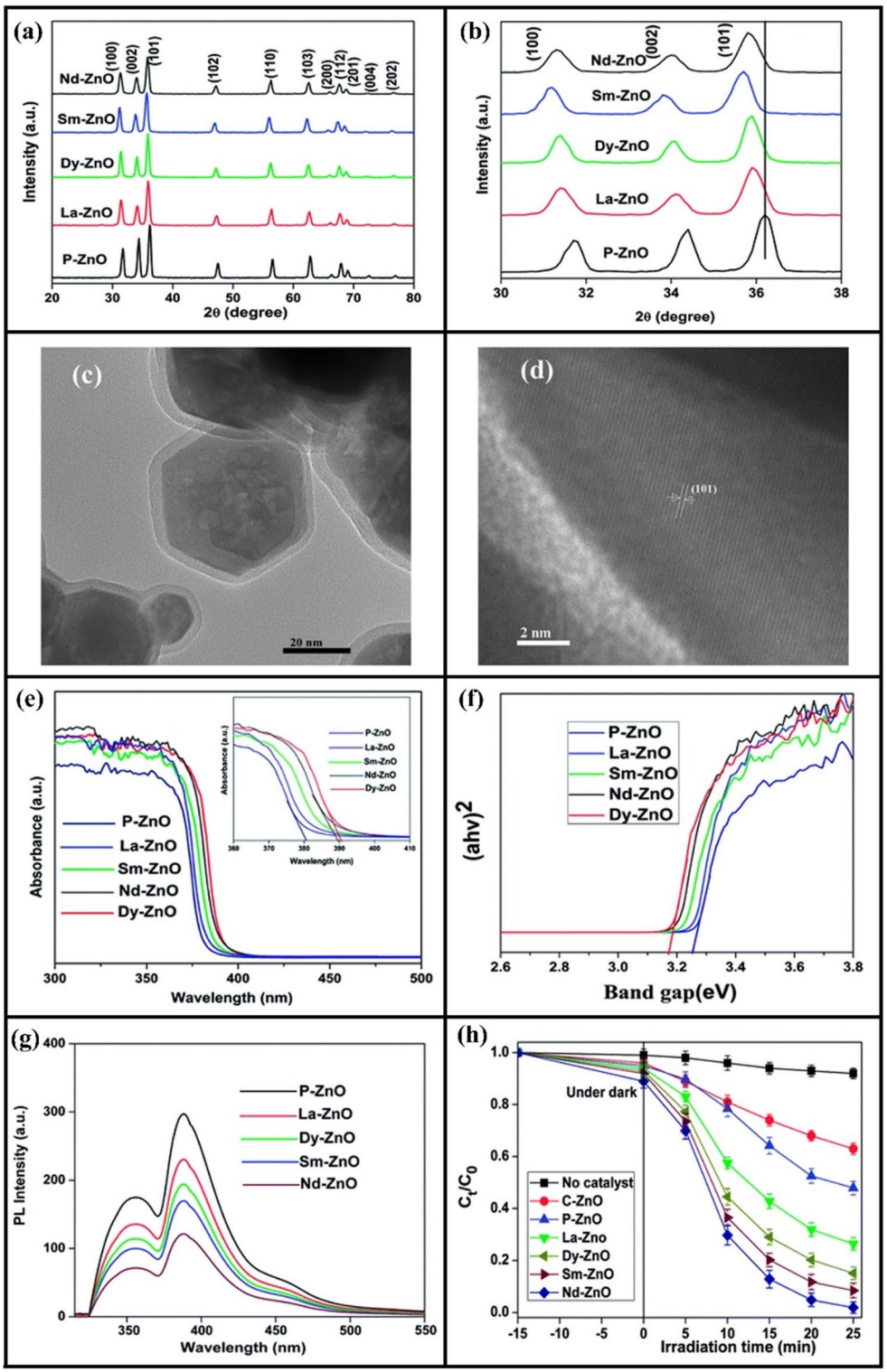

Fig. 11 (**a**, **b**) XRD patterns of pure ZnO and rare earth metal doped-ZnO. (**c**) TEM and (**d**) HRTEM images of Nd-doped ZnO nanoparticles. (**e**) Photoabsorption ability, (**f**) Band gap energy, (**g**) PL spectra, and (**h**) Photocatalytic efficiency of La-, Nd-, Dy-, and Sm-doped ZnO nanoparticles for MB degradation under UV photoirradiation (P-ZnO and C-ZnO stand for pure ZnO and commercial ZnO, respectively). Reproduced with permission from Ref. [216]. Copyright 2018 Royal Society of Chemistry (https://doi.org/10.1039/C8RA01638K)

over five successive runs, whereas a remarkable loss in photocatalytic activity was observed for pure ZnO nanoparticles. This could be attributed to ZnO photocorrosion caused by rapid charge carrier recombination, while rear earth metal doping can improve its stability. Notably, rear earth metals can capture photogenerated electrons from ZnO, preventing photocorrosion under UV irradiation [216]. Among the reactive species, $^{\bullet}OH$ played a major role in MB photodegradation, as confirmed by trapping experiments.

Pascariu et al. [222] synthesized Er-, Sm- and La-doped ZnO nanostructures (~1 at%) for Congo Red photodegradation. Interestingly, the band gap energies of La-, Er-, and

Sm-doped ZnO nanostructures were reported as 2.85 eV, 2.82 eV, and 2.81 eV, respectively, which are slightly higher than that of undoped-ZnO (2.80 eV). Such blue shifts could be attributed to Fermi levels shifting closer to the conduction band, leading to the increase of the carrier concentration [223]. Notably, these slight blue shifts could be the cause of several factors including crystallite size and structural defects (like oxygen vacancies) [222]. Among Er-, Sm- and La-doped ZnO nanostructures, Sm-doped ZnO presented the highest photocatalytic efficiency for the Conge Red removal [222]. Sordello et al. [212] synthesized La-, Ce-, Pr-, Er- and Yb-doped ZnO for Phenol photodegradation under UV irradiation. Yb doping into ZnO lattice structure fortified the accumulation of photoelectrons, whereas doping with Ce improved the rapid transfer of electrons and doping with Er promoted the photocurrent. Yb-doped ZnO showed a robust and effective photocatalytic performance; overall, better photocatalytic activity was linked to a larger accumulation of photoelectrons.

2.3.3 Non-metal doping

Different non-metal elements such as S [1], N [224], F [225] and C [226] have been used as dopants in ZnO for photocatalytic applications. Notably, incorporation of group-VA impurities like As, N, and P resulted in the generation of an acceptor state in ZnO (based on the substitution of oxygen (O)-site (O-site)) [227]. Among the group-VA impurities, N doping could result in the formation of p-type ZnO owing to the approximately similar ionic radius of oxygen (1.38 ˚A) and nitrogen (1.68 ˚A) [227]. Substitutional nitrogen for lattice oxygen highly depends on the crystallinity of ZnO [228]. Overall, among the non-metal elements, nitrogen is considered the most promising dopant because of its similarity with oxygen regarding electronegativity and ionic radius [229]. In addition, nitrogen doping is an effective approach for reducing the bandgap energy of semiconductors [230] and enabling visible light activation [231].

Sacco et al. [231] synthesized N-doped ZnO using the precipitation method for the photocatalytic degradation of Eriochrome Black T (EBT) as a model azo dye. N-doped ZnO was effective for EBT decomposition under visible light irradiation, while commercial ZnO was inactive. Pigosso et al. [232] developed a rapid and straightforward combustion technique to synthesize N-doped ZnO for the removal of tetracycline hydrochloride (TC-HCl), by modifying the urea-to-sucrose ratio and the oxide precursors. They found a considerable 40% increase in visible-light-driven TC-HCl degradation with the optimal N-doped ZnO nanoparticles, as compared to undoped ZnO. Moreover, the synergy between 50% urea and 50% sucrose increased the catalyst's surface area, reaching 25.93 $m^2\ g^{-1}$. Sucrose was applied to control the thermodynamics of the combustion reaction, while urea served as a dopant by providing nitrogen. Peter et al. [229] used a solvent-free method to synthesize N-doped ZnO nanoparticles for brilliant smart green (BG) photodegradation under visible irradiation, where BG removal by N-doped ZnO was considerably higher than by unmodified ZnO. Mandor et al. [224] synthesized N-doped TiO_2 beads (NTB) and N-doped ZnO beads (NZB) using ammonium acetate, urea and sol-gel technique for the photocatalytic degradation of phenol and ammonia under UV irradiation. The BET specific surface areas of these materials, are 24.911 $m^2\ g^{-1}$ (NTB) and 16.757 $m^2\ g^{-1}$ (NZB). Phenol degradation efficiency reached 44%, 36%, 57%, and 76% for ZnO, TiO_2, NTB, and NZB, respectively; and degradation efficiency of ammonia reached to 47%, 45%, 69%, and 73% for ZnO, TiO_2, NTB, and NZB, respectively. ZnO was more effective than TiO_2 and NZB was more effective than NTB, introducing ZnO as a potential alternative to TiO_2 for photocatalytic degradation of phenol and ammonia. Secondly, N doping significantly improved phenol and ammonia degradation over both ZnO and TiO_2, clarifying the potential of this procedure in improving the photocatalytic performance. N-doped TiO_2 and N-doped ZnO beads with the nitrogen-to-oxygen acceptor defect and the intrinsic donor defect of oxygen vacancy could be activated by the lower consumption of UV energy for proficient pollutant decomposition. For methylene blue photodegradation under visible or UV light irradiation, Prabakaran et al. [233] synthesized N-doped ZnO nanoparticles with cabbage morphology (N-ZnONCBs) using a hydrothermal technique (nitrogen source: hydrazine monohydrate and precursor: zinc acetate dihydrate). Notably, N-ZnONCBs showed narrower band gap energy than pure ZnO nanoparticles (2.9 eV against 3.28 eV, respectively). Compared with UV light, the N-ZnONCB photocatalyst exhibited higher performance in MB photodegradation within 50 min under visible light irradiation. In addition, the N-ZnONCB photocatalyst demonstrated good reusability and photostability, achieving approximately 93% MB degradation after four cycles.

3 Machine learning modeling

3.1 CSA-LSSVM

It is well established that pattern recognition and classification of input data could be performed using different ML algorithms, such as support vector machine (SVM) and least square support vector machine (LSSVM). To overcome the general difficulties of SVM algorithm, LSSVM method [234] has been developed as a new version of SVM. The error of regression is added to the constraints of

optimization in LSSVM method. Noteworthily, regression error is defined and mathematically solved in LSSVM algorithms, whereas it is optimized within the learning stage in SVM methods [234]. The potential function (Q) is defined as shown in Eq. (1) in LSSVM [234–237]:

$$Q_{LSSVM} = \frac{1}{2} w^T w + \gamma \sum_{k=1}^{N} e_k^2 \quad (1)$$

where w represents the weight vector, e_k is the regression error of N training objects, T denotes transpose matrix, and γ is the summation of regression errors. Equation (1) is subjected to the constraints shown in Eq. (2) [234]:

$$y_k = w^T \phi\ (x_k) + b + e_k\ ,\ k = 1,2,\ \ldots\ , N \quad (2)$$

The transpose matrix, the output vector of the model, the kernel function, and the bias or the intercept of linear regression are represented by the variables T, y, $\phi\ (x_k)$ and b in the above equation, respectively. The following equation is the normal expression for the w [234]:

$$w = \sum_{k=1}^{N} a_k x_k \quad (3)$$

where

$$\alpha_k = 2\gamma\, e_k \quad (4)$$

A reformulation of Eq. (2) using the LSSVM algorithm is represented by Eq. (5) [234–237]:

$$y = \sum_{k=1}^{N} a_k x_k^T x + b \quad (5)$$

As a result, Eq. (6) is the determination of the Lagrange multipliers [234]:

$$a_k = \frac{(y_k - b)}{x_k^T x + (2\gamma)^{-1}} \quad (6)$$

The following Kernel function can be used to rewrite the above linear regression equation [234]:

$$f\ (x) = \sum_{k=1}^{N} a_k K\ (x, x) + b \quad (7)$$

The Kernel function, which was defined by the dot product of x and x_k vectors, is shown in this equation as K(x, x_k). In fact, the dot product of $\Phi(x)^T$ and $\Phi(x_k)$ are K(x, x_k) as described below [234]:

$$K\ (x, x_k) = \varphi\ (x)^T + \varphi\ (x_k) \quad (8)$$

The radial basis Kernel function, one of the most well-known Kernel functions, was used in this study using the following expression:

$$K\ (x, x_k) = exp\ (-\parallel x_k - x\ \parallel^2 / \sigma^{\,2}) \quad (9)$$

where σ^2 is a tuning parameter in this equation that should be determined during the calculations using an optimization approach. In summary, throughout the training process, the two tuning parameters of LSSVM namely γ and σ^2 should be optimized using an external optimization tool. In this investigation, the LSSVM algorithm designed by Suykens and Vandewalle [234] and Pelckmans et al. [238] was employed. Coupled Simulated Annealing (CSA) was used to optimize the tuning variables, and the resulting model was named CSA-LSSVM [239].

3.2 DT

This algorithm for decision trees is tree-structured. There is a root, several branches, nodes, and leaves in a standard binary tree. Using a top-down methodology, decision trees split a dataset into numerous smaller subsets and decide on each one individually. There are decision nodes and leaf nodes in a decision tree. While leaf nodes describe decisions on targets, decision nodes describe features' attributes. The mean square error serves as the loss function for the regression decision tree [240, 241]. The method will determine the MSE of the subset as well as the anticipated value for each leaf node. The smallest MSE value is used to grow the regression decision tree. The decision tree's maximum depth dictates which branches will be cut the deeper they go. In low sample sizes and high latitude, overfitting can be effectively reduced by limiting the tree's depth [242].

3.3 RF

According to Liaw and Wiener [243], RF is an integrated learning technique for regression and classification. It is an additive model based on the bagging algorithm and is one of the representatives of ensemble learning. In contrast to bagging, RF employs a random sample predictor prior to each node segmentation during tree construction, potentially mitigating bias. It possesses the following qualities: (a) by adding two randomness, RF is less likely to overfit and has superior noise immunity; (b) it can handle high-dimensional (many-feature) data without feature selection; (c) it can be easily parallelized and has a quick training speed, making it relatively easy to implement [244, 245]. The literature provides more information about RF, as referenced in [246].

3.4 XGB

The shortcomings of traditional Gradient Boosting were addressed by the development of XGB, a tree-based ensemble learning approach. To lessen bias and variance, XGB builds a series of weak decision tree learners in succession [247]. The basic principle of XGB is to gradually improve weak learners in order to become a strong learner. With each new tree added, the model attempts to correct the errors made by the previously trained trees [248]. XGB builds trees sequentially while accounting for the flaws of the preceding trees, in contrast to Random Forest, which builds trees concurrently. In order to build its model, XGB optimizes the following objective function:

$$\mathrm{L}\left(\Phi\right) = \sum l(y_1, \widehat{y}_i) + \sum \Omega\ (f_k) \tag{10}$$

where $\widehat{y}_i$ represents the estimated result for the i-th observation, f_k represents the individual trees, $\Omega(f_k)$ indicates the model's complexity, $l\,(y_1, \widehat{y}_i)$ is the loss function that quantifies the difference between the estimated and the actual result, and L(Φ) is the objective function to be optimized [249]. The loss function $l\,(y_1, \widehat{y}_i)$ is usually selected to be a differentiable function, such as log loss for classification tasks or the squared error for regression tasks. The objective function also contains a regularization term $\Omega(f_k)$ that penalizes model complexity, aiding in the control of overfitting [250]. Furthermore, XGB can estimate out-of-bag errors by using a validation set in each iteration of the boosting process. Without the use of external test data, an objective calculation of generalization error may be calculated using just this subset [251]. Additionally, by lowering dimensionality, XGB's integrated feature significance measure enhances the model's performance on big datasets. The frequency with which a feature appears in the model's trees determines its feature importance score [252]. Due to its ability to handle sparse data well, its parallel processing capabilities, and its versatility in objective functions and evaluation measures, XGB can perform better than competing methods across a range of machine learning applications [253].

3.5 Data gathering

The Scopus database was used to locate the relevant experimental data. Numerous studies have reported the application of ZnO in photodegradation, enabling in-depth analysis and prediction. The physiochemical characteristics of pollutants and ZnO dopants; and photocatalytic parameters were compiled based on the information in the literature on the photocatalytic treatment of various pollutants. The process variables considered as inputs were initial pollutant concentration (C_0), solution pH, photocatalyst dosage (mg/L), weight ratio of doping elements to Zn (Dopant/Zn), light source (UV (1) and visible light (2)), and irradiation time (min). Additionally, the molecular weight of the pollutants and dopants (g/mol), TPSA (Å²), HBDC and HBAC of pollutants also were considered as the inputs, and they were extracted from PubChem (https://pubchem.ncbi.nlm.nih.gov). Table 1 displays the details of these parameters. Finally, by considering 19 different pollutants and their degradation by ZnO-based photocatalysts, without and with doping elements, a comprehensive dataset was produced. The WebPlotDigitizer software (https://automeris.io/) was used to extract the relevant data from the literature (**Table S1**).

Table 1 Properties of the pollutants and ZnO dopants used in this study

Pollutants	MW (g mol^{-1})	TPSA	HBDC	HBAC	Dopants of ZnO	MW (g mol^{-1})
Rose Bengal (RB)	1017.6	89.5	0	5	Mn	54.93
Methylene Blue (MB)	319.9	43.9	0	4	La	138.905
Bromocresol Green (BG)	698	92.2	2	5	W	183.84
Methyl Orange (MO)	327.34	93.5	0	6	Sb	121.76
Congo Red (CR)	696.7	233	2	12	Eu	151.964
Direct Black 38 (DB38)	781.78	304	4	16	Sm	150.4
Orange G (OG)	452.4	176	1	9	Without dopant	0
Norfloxacin (NOR)	319.33	72.9	2	7		
2-Chlorophenol (2-CP)	128.55	20.2	1	1		
Dichlorvos	220.97	44.8	0	4		
Diazinon	304.35	85.6	0	6		
Phenol	94.11	20.2	1	1		
Benzoic Acid	122.12	37.3	1	2		
Rhodamine B (RhB)	479	52.8	1	5		
Malachite Green	364.9	6.3	0	2		
Reactive Black 5 (RB5)	991.8	462	2	24		
Reactive Orange 4 (RO4)	781.5	284	1	16		
2,4-Dichlorophenol (2,4-DCP)	163	20.2	1	1		
Monocrotophos (MCP)	223.16	73.9	1	5		

Table S2 provides the photodegradation percentage (minimum and maximum values) and the details of the experimental conditions. Details regarding the extraction of data are provided in **Text S1** and **Table S3**. Notably, the specifications of the pollutants were not consistently provided in the publications. Moreover, each pollutant may be commercially available with different properties, as suppliers differ, and even a single supplier may offer different types of the same pollutant. Therefore, a specific pollutant used in different publications might not be entirely identical in terms of molecular weight, TPSA, HBAS, and HBDC. However, for a given pollutant across different publications, these were considered similar in our study for the sake of simplicity.

In order to create accurate machine learning models, 85% of the data points were selected at random to serve as the training set, while the remaining 15% of the data points were used as the test data to evaluate the models' accuracy. Measurable variables like mean absolute error (MAE), average absolute relative deviation (AARD), determination coefficient (R^2), and root-mean-square error (RMSE) were calculated to assess the statistical analysis. These variables are explained in the following equations:

$$R^2 = 1 - \frac{\sum_{i=1}^{n}[x_i^{predicted} - x_i^{experimental}]^2}{\sum_{i=1}^{n}[x_i^{experimental} - x^m]^2}, \quad x_m = \frac{\sum_{i=1}^{n} x_i^{experimental}}{n} \tag{11}$$

$$AARD\ (\%) = \frac{100}{n} \sum_{i=1}^{n} \frac{\left| x_i^{predicted} - x_i^{experimental} \right|}{x_i^{experimental}} \tag{12}$$

$$RMSE = \sqrt{\frac{1}{n} \sum_{i=1}^{n} (x_i^{experimental} - x_i^{predicted})^2} \tag{13}$$

$$MAE = \frac{1}{n} \sum_{i=1}^{n} \left| x_i^{experimental} - x_i^{predicted} \right| \tag{14}$$

Table 2 Hyperparameters of the selected models

Model	Hyperparameters
DT	Max depth = 11, min samples split = 5, min samples leaf = 2, max leaf nodes = 99
RF	n estimators = 131, max samples = 0.681554237, min samples split = 5, min samples leaf = 1, max depth = 11
XGB	N estimators = 290, learning rate = 0.162273782, subsample = 0.751916662, max depth = 13, min child weight = 7.498632011, gamma = 1.372125436, colsample by tree = 0.860322036
XGB (log of target data)	N estimators = 233, learning rate = 0.19231, subsample = 0.669023, max depth = 5, min child weight = 7.812104, gamma = 0.002698, colsample by tree = 0.806194
CSA-LSSVM	$\sigma^2 = 1.5357$, $\gamma = 102.7720$
PSO	Particles number = 10, iteration 100, c1 = 0.5, c2 = 0.3, w = 0.9

Validation of the model was evaluated using two fundamental methods: visual comparison plots and statistical analysis. The degree of alignment between the actual and predicted values is indicated by the statistical parameters.

3.6 ML modeling results

In machine learning, fine-tuning hyperparameters is crucial since it has a direct impact on the effectiveness and behavior of training models [254]. For hyperparameter modification, traditional approaches like Grid Search (GS) and Random Search (RS) are frequently used; nevertheless, each has inherent drawbacks that should be carefully considered [255]. These constraints include complex search spaces, high iteration computation time, and high result variability. On the other hand, Particle Swarm Optimization (PSO), a population-based metaheuristic inspired by nature and based on swarm intelligence, offers a straightforward yet effective method for finding near-optimal solutions in intricate, high-dimensional search spaces that mimic real-world situations. Notably, Eberhart and Kennedy developed PSO [256]. The PSO technique was used in this study to find the best hyperparameters for machine learning models. There are several control factors that influence the basic PSO approach. Iterative experimentation was used to determine the starting values for these parameters. Defining input variables and the output target, dividing the dataset into training and testing subsets, optimizing XGB, DT, and RF hyperparameters by PSO, and evaluating the model's prediction performance were the main steps of the modeling framework. To obtain accurate values, the LSSVM variables of σ^2 and γ were optimized using the CSA optimization approach. Finally, for the CSA-LSSVM model, the evaluated and optimized values of σ^2 and γ are 1.5357 and 102.7720, respectively. The hyperparameters of the developed model is shown in Table 2.

The obtained R^2 value for the test data is 0.8479, 0.7748, 0.917, and 0.9604 for RF-PSO, DT-PSO, CSA-LSSVM, and XGB-PSO models, respectively. As tabulated in Table 3, comparative statistics for AARD, RMSE, and MAE validate that the XGB-PSO calculation of the photocatalytic degradation of pollutants is accurate enough.

The actual photodegradation efficiencies for pollutants are compared with the output of the model, developed by ML, as demonstrated in Fig. 12. The more accurate the models are, the closer the data aligns with the bisector line. For the photodegradation framework, the developed XGB-PSO model provides reliable prediction. Relative degradation of the estimations by the developed models are shown in Fig. 13. XGB-PSO model has the lowest relative deviations among the other models.

For better comparison, an XGB-PSO model was developed to predict the logarithm of the target data as its output.

Table 3 Accuracy and error in Estimation of the photocatalytic activity (degradation percentage) by the models

Metrics	Dataset	RF-PSO	DT-PSO	CSA-LSSVM	XGB-PSO	XGB (log of target data)
R^2	Train	0.9271	0.8506	0.9591	0.9962	0.9802
	Test	0.8479	0.7748	0.9170	0.9604	0.9288
	Total	0.9154	0.8396	0.9529	0.9909	0.9723
RMSE	Train	7.2406	10.3667	5.4237	1.6518	0.0903
	Test	10.4614	12.7296	7.7260	5.3399	0.1746
	Total	7.8077	10.7534	5.8264	2.5666	0.1072
MAE	Train	5.5080	7.9002	2.8614	1.1632	0.0613
	Test	7.8897	9.5819	5.5564	3.6223	0.1079
	Total	5.8645	8.1518	3.2647	1.5312	0.0683
AARD (%)	Train	17.3382	22.0888	7.5178	3.1835	1.7012
	Test	26.0026	27.5978	18.7061	10.7545	3.1519
	Total	18.6349	22.9132	9.1922	4.3165	1.9183

As it can be seen in Figs. 12 and 13, by considering this model lower relative deviation are obtained and there is lower error distribution.

3.7 Influence of features on pollutant degradation

The XGB-PSO model, which shows the best performance among the four models in our study, is used to examine how features influence pollutant degradation by ZnO-based photocatalysts. The Embedded Feature Importance (EFI) bar chart, SHAP value summary plot, and partial dependence plot for the model's input variables are shown in Figs. 14 and 15. As shown in the EFI bar chart, TPSA and pollutant molecular weight, both pollutant-specific properties, have the highest importance among all variables in the model's prediction. It should be noted that larger organic molecules may require a greater number of charge carriers for mineralization [257]. Overall, pollutants exhibit structural differences [258], and their chemical structure influences photodegradation performance [259]. Additionally, effective adsorption of pollutants onto the catalyst surface can enhance their removal from solution [259]. Compared to organic pollutants with electron-donating groups, those containing electron-withdrawing groups tend to adhere more strongly to the catalyst surface, thereby facilitating their direct oxidation [259]. Aside from TPSA and pollutant molecular weight, irradiation time and catalyst dosage are among the most influential features in the model's prediction, as shown in the EFI bar chart (Fig. 14). Notably, the significant effects of irradiation time and catalyst dosage on photodegradation performance are well-established. For instance, OG degradation over ZnO was 8% at t = 5 min and 65% at t = 50 min [43]. In addition, increasing the irradiation time from 5 to 10 min raised the degradation percentage from approximately 8% to 18%, whereas extending the time from 45 to 50 min had little, with degradation remaining around 65% [43]. These results indicate that irradiation time highly affects pollutant degradation, with higher degradation percentages generally observed at longer exposure times. The SHAP value summary supports this trend, showing that extended irradiation times are associated with enhanced model output, reflecting higher degradation percentages at later stages. The partial dependence plot (Fig. 15**)** illustrates that increasing irradiation time positively influences the predicted pollutant degradation percentage, signifying that longer exposure enhances degradation efficiency. Regarding catalyst dosage, it is important to note that an optimum amount is required to achieve maximum photocatalytic performance. Although increasing the catalyst dosage can provide more active sites for pollutant degradation, excessive amounts may reduce photocatalytic activity. For instance, Garg et al. [43] investigated the effect of GO-ZnO nanocomposite dosage ranging from 0.4 to 1.0 g L^{-1}, and they found that increasing the dosage from 0.8 to 1.0 g L^{-1} decreased the efficiency of Orange G removal, likely due to restricted light penetration. The SHAP value summary shows that lower catalyst dosage values tend to enhance the predicted degradation percentage.

Based on the EFI bar chart, the weight ratio of the doping element to Zn, the dopant molecular weight, the solution pH, and the initial pollutant concentration have moderate importance in the model's prediction. Regarding dopants, it should be noted that their photocatalytic performance highly depends on both their type and concentration. In our study, the effects of six dopants (Mn, W, Sb, Eu, La, and Sm) were investigated; however, the weight ratio of these elements to Zn was in the range of 0.021–0.123. Noteworthily, the effect of pH on photodegradation efficiency depends heavily on both the photocatalyst and the pollutant type. For instance, Sakthivel et al. [123] studied the effect of pH (ranging from 3 to 11) on the photodegradation rate of acid brown 14 and found that pH 10 resulted in the highest rate. In contrast, Chen et al. [56] studied the effect of pH (ranging from 2 to 10) on the removal rates of MO, CR, and DB38, finding that the highest rates were achieved at pH 2, pH 2, and pH 4, respectively. Interestingly, Daneshvar

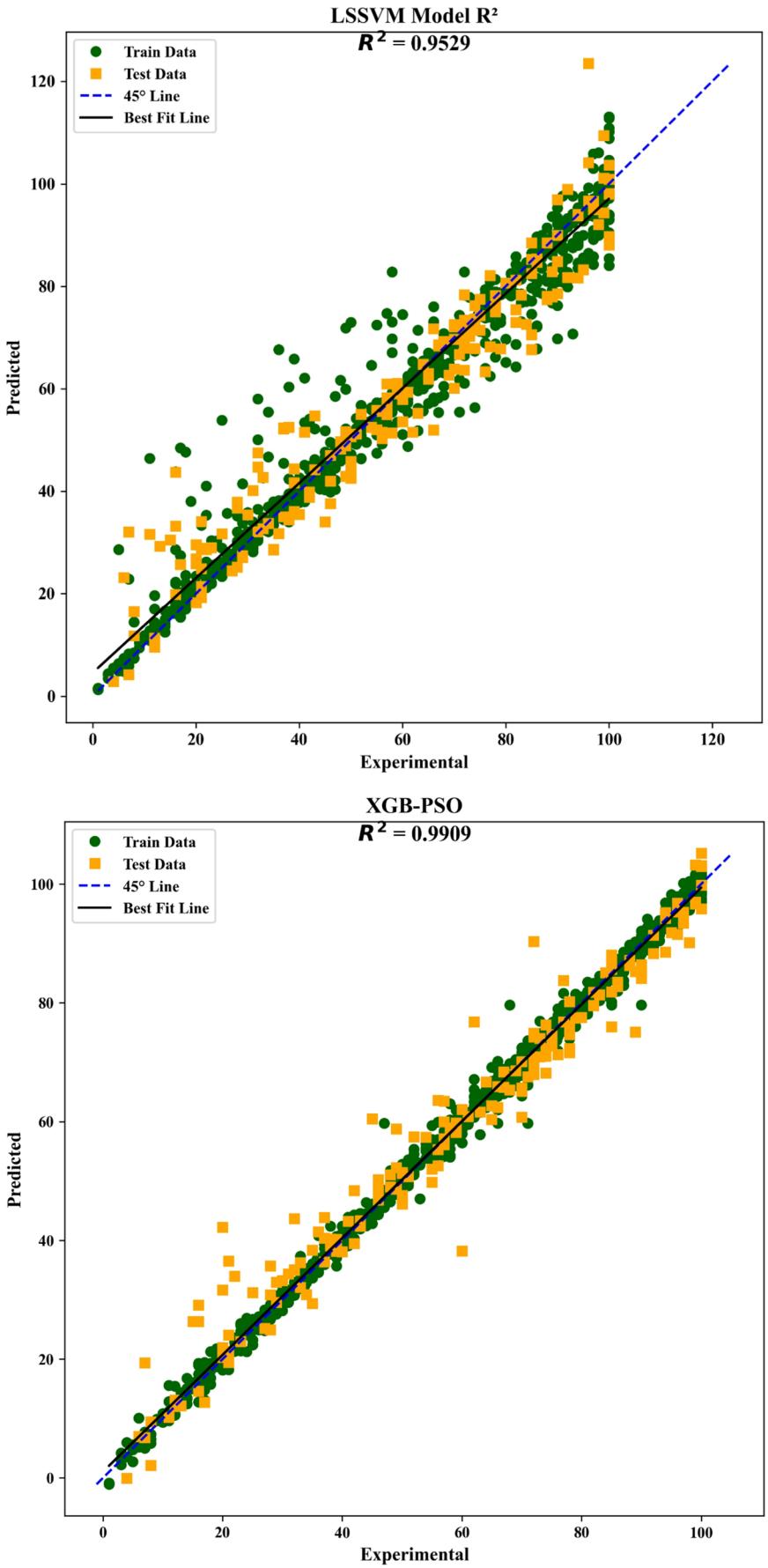

Fig. 12 Estimation of the pollutant photo-degradation percentage using the developed models compared to the experimental results

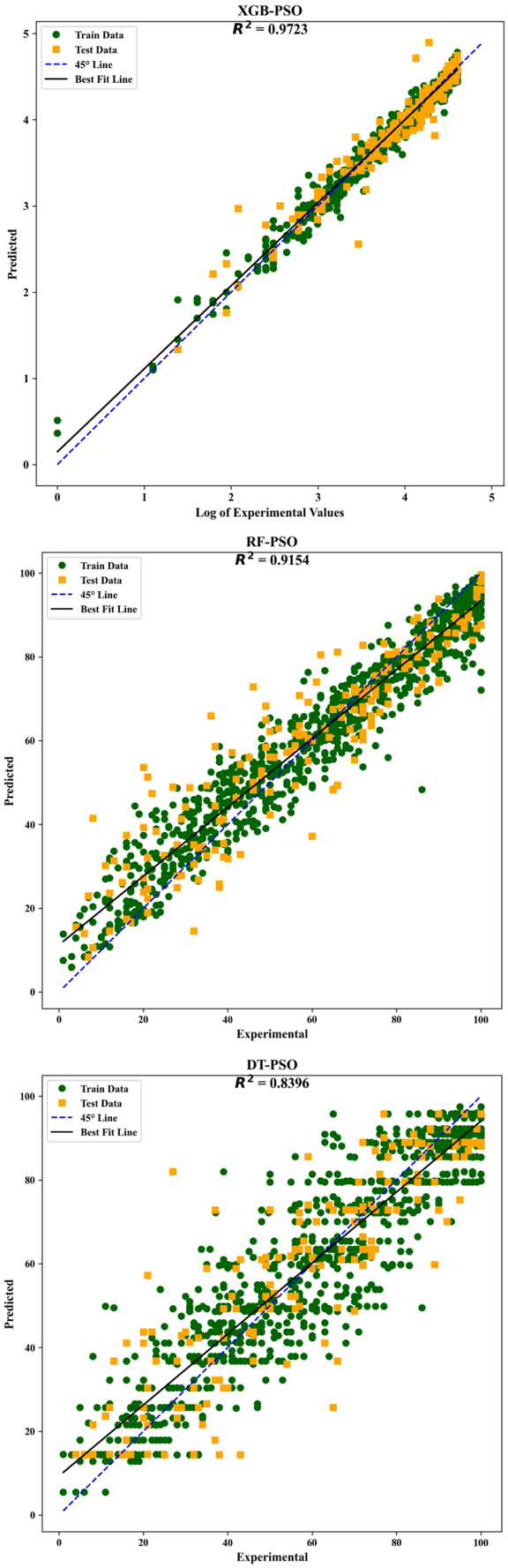

Fig. 12 (continued)

et al. [117] investigated the effect of pH (ranging from 4 to 12) on the photodegradation of acid red 14, reporting the highest efficiency at pH 7. It should be noted that the ZnO surface carries a negative charge in alkaline solutions and a positive charge in acidic aqueous solutions [260]. As a result, it preferentially adsorbs cationic and anionic organic pollutants, respectively [260]. Overall, the strong effects of solution pH and pollutant molecular complexity may result in considerably different photocatalytic performances [260]. Similar to catalyst dosage, an optimum initial pollutant concentration is required to achieve maximum photocatalytic performance. Garg et al. [43] studied the effect of initial OG concentration, ranging from 10 to 50 mg L^{-1}, on the photocatalytic activity of GO-ZnO nanocomposites. Increasing the OG concentration from 10 to 30 mg L^{-1} improved OG removal, whereas a further increase from 30 to 50 mg L^{-1} adversely affected the removal efficiency. It has been stated that high dye concentrations can restrict light penetration and reduce the number of active sites available on the catalyst surface [43]. Both the SHAP value summary and the partial dependence plot illustrate that higher levels of C_0 negatively impact the model output, signifying an adverse effect at elevated initial pollutant concentrations. As shown in the EFI bar chart, the light source has the least effect on the model's output among all input variables. This may be attributed to the limited variability of this feature, as only two levels were defined: UV (1) and visible light (2). The partial dependence plot (Fig. 15**)** exhibits that UV irradiation has a stronger positive impact on the model output (predicted degradation percentage). This aligns with the fact that ZnO is not effectively activated under visible light due to its wide band gap energy (~3.2 eV) [261]. Although some dopants have been introduced to improve visible light activation [233], the dataset is heavily skewed toward UV sources, as shown in **Table S1**. Consequently, both the SHAP and partial dependence plots reflect a greater model response to UV compared to visible light.

3.8 Web-based model

To easily calculate the pollutant degradation by ZnO-based photocatalysts using the XGB-PSO, a web-based app developed, click on the following link:

https://xgb-pso-degradation-app-k8ylxwzqdn3pwkfjfpvfqq.streamlit.app/.

As illustrated in Fig. 16, users can input data and obtain the predicted values of pollutant degradation.

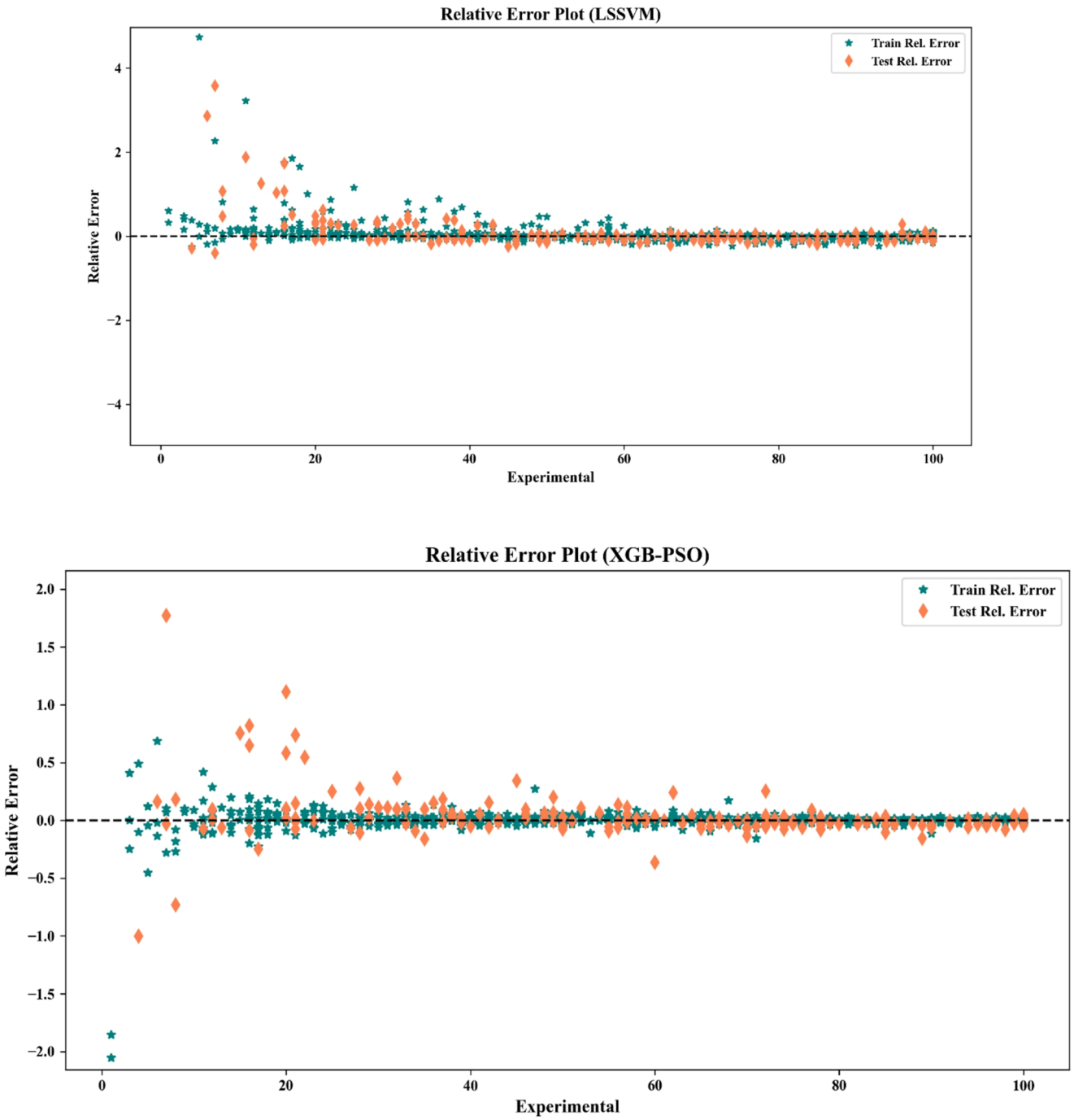

Fig. 13 Relative deviations of the estimation of photodegradation of pollutants using the developed models

4 Conclusions

As confirmed by the literature review in this study, ZnO microstructure is a key factor affecting its photocatalytic activity. Wurtzite ZnO is the most stable phase of ZnO which has been commonly used in photocatalytic degradation of organic pollutants. Rocksalt ZnO is a metastable phase, but it can produce a higher photocatalytic activity than anatase TiO_2 and wurtzite ZnO. Different non-metal and metal elements have been used as dopants to enhance the photocatalytic activity of ZnO, where nitrogen is considered very promising owing to its similarity of electronegativity and ionic radius to oxygen. Importantly, nitrogen doping could promote ZnO to be activated under visible light for EBT decomposition. In addition to microstructure, morphology can highly affect the photocatalytic activity

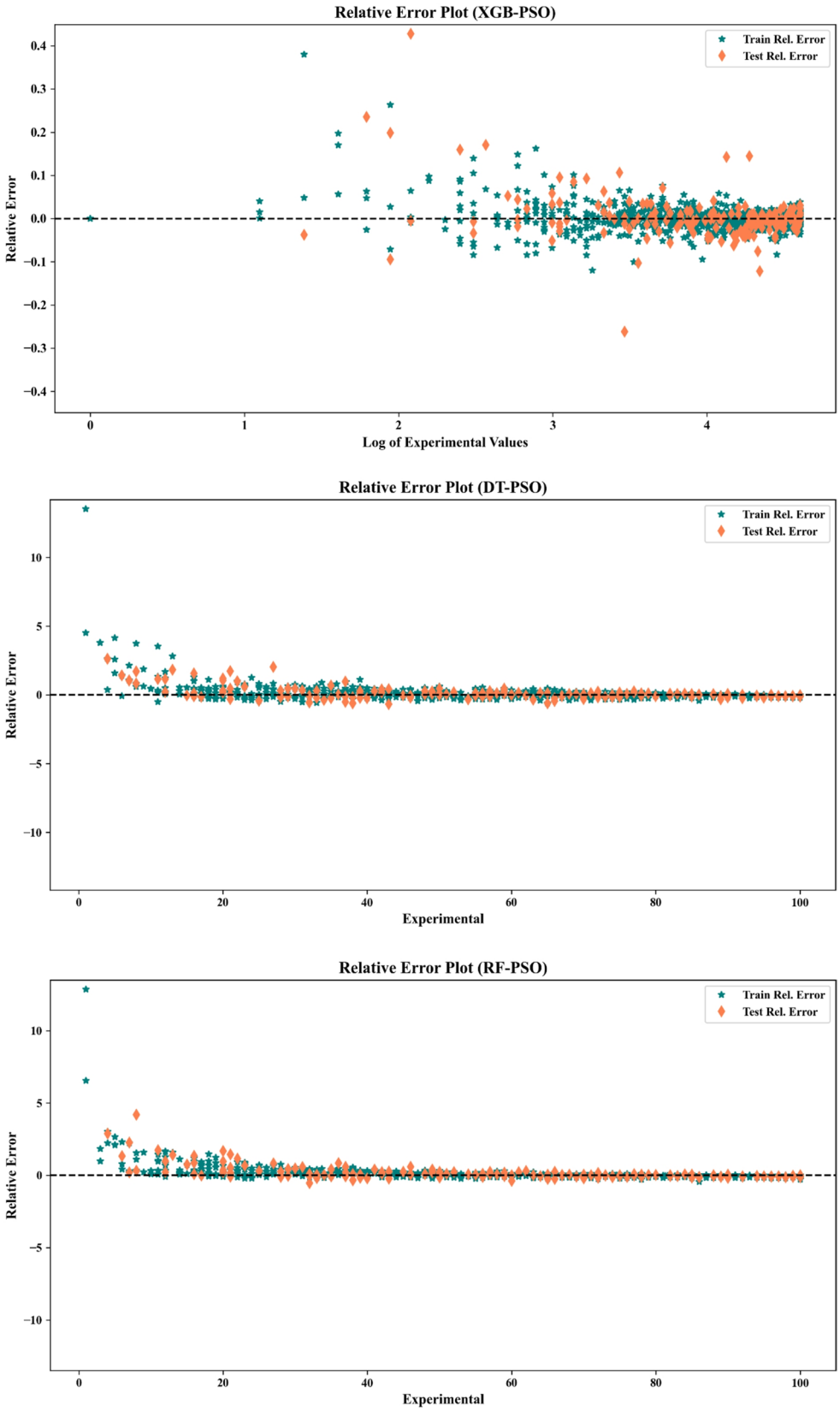

Fig. 13 (continued)

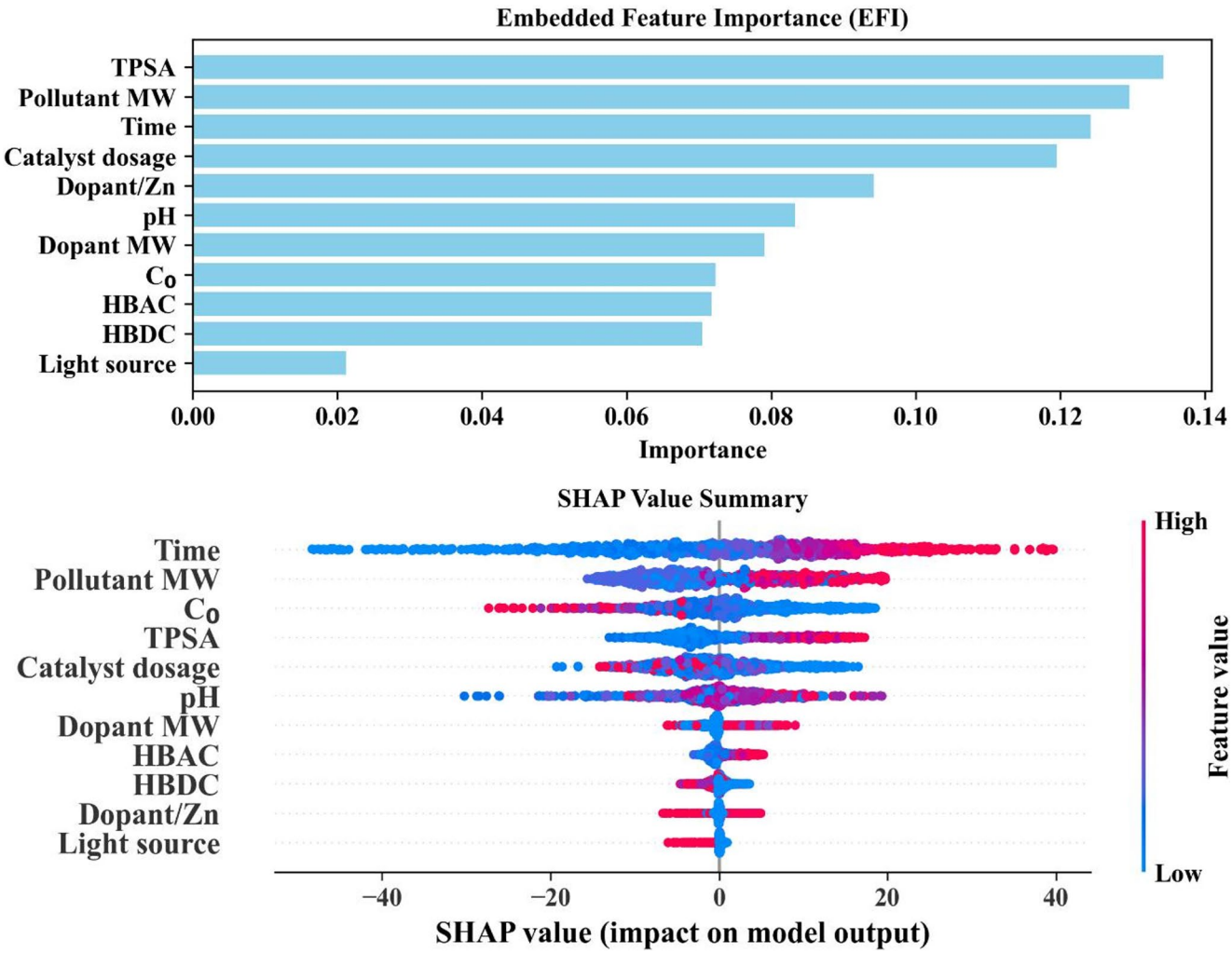

Fig. 14 EFI bar chart and SHAP value summary plot for the model's input variables

of ZnO. The aspect ratio is another important parameter which affects the photocatalytic activity of ZnO structures with regard to their morphology. In addition to the review study, a comprehensive dataset of 1176 entries (covering 19 different pollutants) was collected from the literature and modeled using the CSA-LSSVM, DT-PSO, RF-PSO, and XGB-PSO machine learning algorithms. The models accurately predicted the pollutant degradation by ZnO photocatalyst with R^2 of 0.8479, 0.7748, 0.917, and 0.9604 for RF-PSO, DT-PSO, CSA-LSSVM, and XGB-PSO models, respectively. The web-based app designed in this study is a valuable and easy to use tool by researchers to predict pollutant degradation by ZnO-based photocatalysts.

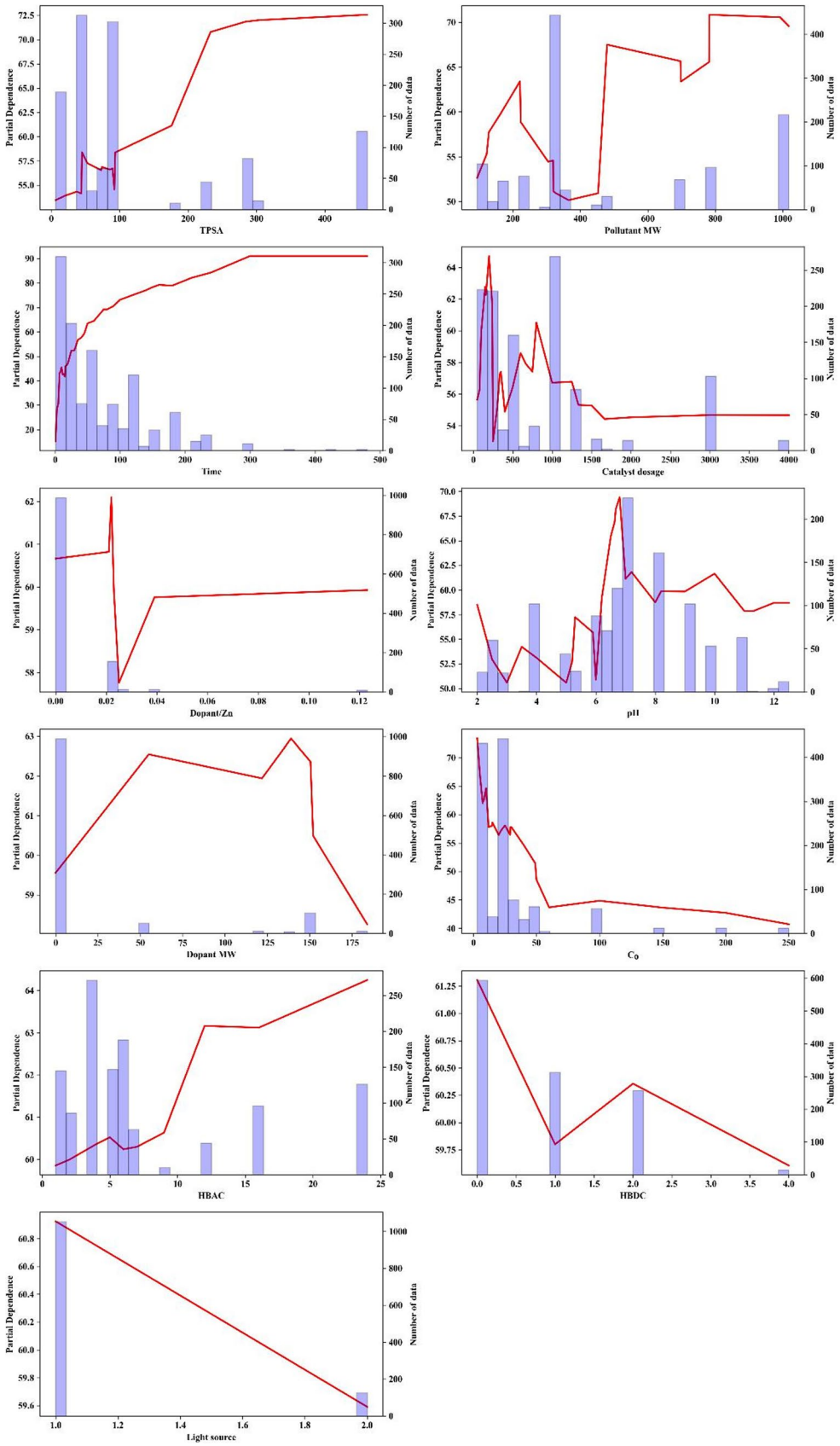

Fig. 15 Partial dependence plot for the model's input variables (in each graph, the blue bars show the feature value distribution, and the red line represents the partial dependence of each feature on the model output)

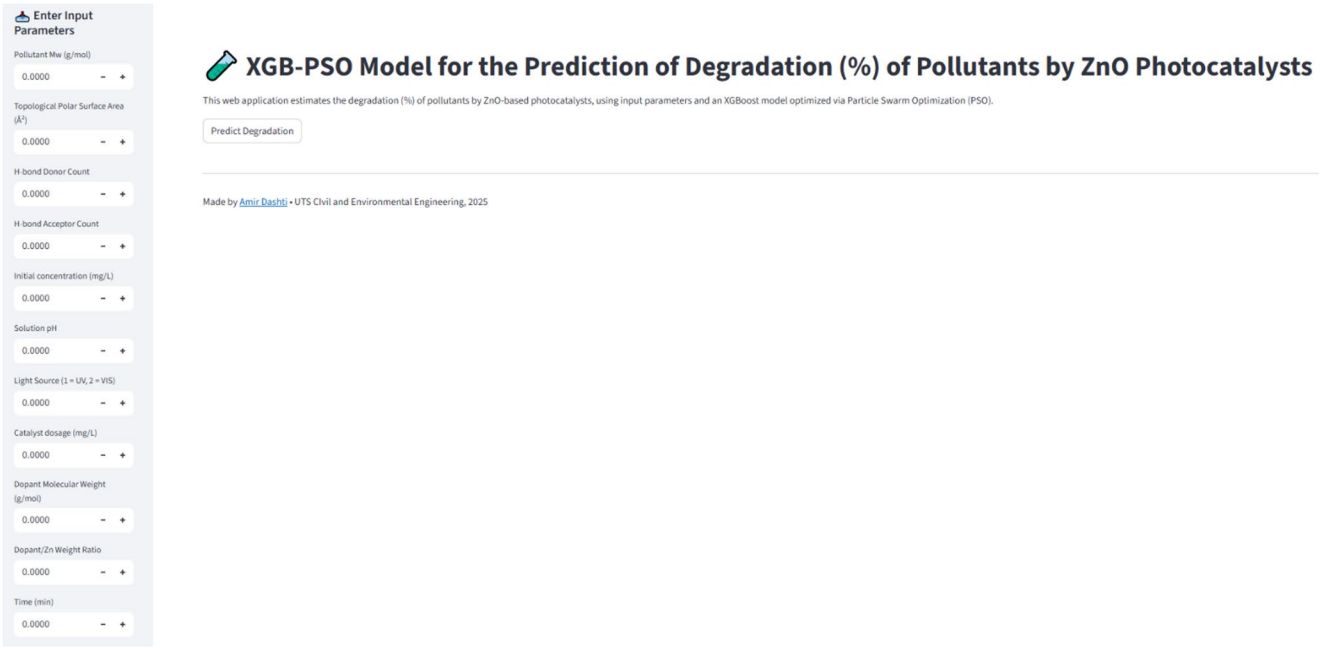

Fig. 16 View of the software developed

Supplementary Information The online version contains supplementary material available at https://doi.org/10.1007/s42114-026-01674-1.

Author contributions AHN: investigation, writing-original draft, writing-review and editing. AD: investigation, writing-original draft, writing-review and editing. EAD: writing-review and editing. PA: graphical designs, writing-review and editing. JLZ: supervision, writing-review and editing. AZM: supervision, writing-review and editing. AA: writing-review and editing.

Funding Open Access funding enabled and organized by CAUL and its Member Institutions. This work was supported by the University of Technology Sydney (UTS President's and International Scholarships). Sharif University of Technology and the financial support from Organization for Development of International Science and Technology Cooperation for the postdoctoral research program are also acknowledged.

Data availability The data and materials are available on request.

Declarations

Generative AI and AI-assisted technologies in the writing process During the preparation of this work, the author(s) used Google Translate, QuillBot, Grammarly, Gemini, and ChatGPT in order to check the grammar and improve clarity. After using these tools/services, the author(s) reviewed and edited the content as needed and take(s) full responsibility for the content of the publication.

Competing interests The authors declare no competing interests.

References

1. Mirzaeifard Z, Shariatinia Z, Jourshabani M, Rezaei Darvishi SM (2020) *ZnO* photocatalyst revisited: effective photocatalytic degradation of emerging contaminants using S-doped *ZnO* nanoparticles under visible light radiation. Ind Eng Chem Res 59:15894–15911. https://doi.org/10.1021/acs.iecr.0c03192
2. Qiu J, Liu Y, Cao M, Xie L, Liu Y, Li H, Lu J, Liang Q, Pan J, Li C (2024) Synthesis of MoS_2/MoO_3 nano-heterojunction towards enhanced photocatalytic activity under LED light irradiation via in situ oxidation sintering. RSC Adv 14:34606–34610. https://doi.org/10.1039/D4RA05673F
3. Sun J, Mu Q, Kimura H, Murugadoss V, He M, Du W, Hou C (2022) Oxidative degradation of phenols and substituted phenols in the water and atmosphere: a review. Adv Compos Hybrid Mater 5:627–640. https://doi.org/10.1007/s42114-022-00435-0
4. Ghazal H, Koumaki E, Hoslett J, Malamis S, Katsou E, Barcelo D, Jouhara H (2022) Insights into current physical, chemical and hybrid technologies used for the treatment of wastewater contaminated with pharmaceuticals. J Clean Prod 361:132079. https://doi.org/10.1016/j.jclepro.2022.132079
5. Kumari P, Kumar A (2023) ADVANCED OXIDATION PROCESS: a remediation technique for organic and non-biodegradable pollutant. Results Surf Interfaces 11:100122. https://doi.org/10.1016/j.rsurfi.2023.100122
6. Goodarzi N, Ashrafi-Peyman Z, Khani E, Moshfegh AZ (2023) Recent progress on semiconductor heterogeneous photocatalysts

in clean energy production and environmental remediation. Catalysts 13:1102. https://doi.org/10.3390/catal13071102
7. Saravanan A, Deivayanai VC, Kumar PS, Rangasamy G, Hemavathy RV, Harshana T, Gayathri N, Alagumalai K (2022) A detailed review on advanced oxidation process in treatment of wastewater: mechanism, challenges and future outlook. Chemosphere 308:136524. https://doi.org/10.1016/j.chemosphere.2022.136524
8. Scaria J, Nidheesh PV (2022) Comparison of hydroxyl-radical-based advanced oxidation processes with sulfate radical-based advanced oxidation processes. Curr Opin Chem Eng 36:100830. https://doi.org/10.1016/j.coche.2022.100830
9. Gopalakrishnan G, Jeyakumar RB, Somanathan A (2023) Challenges and emerging trends in advanced oxidation technologies and integration of advanced oxidation processes with biological processes for wastewater treatment. Sustainability 15:4235. https://doi.org/10.3390/su15054235
10. Sun Y, Meng X, Dall'Agnese Y, Dall'Agnese C, Duan S, Gao Y, Chen G, Wang X-F (2019) 2D MXenes as co-catalysts in photocatalysis: synthetic methods. Nano-Micro Lett 11:79. https://doi.org/10.1007/s40820-019-0309-6
11. Zhang X, Xu X, Li C, Dai L, Hao Z, Yu J, He H, Si C, Shen Z, Qiu Z, Wang J (2023) Metal-free graphitic carbon nitride/black phosphorus quantum dots heterojunction photocatalyst for the removal of ARG contamination. Adv Compos Hybrid Mater 6:145. https://doi.org/10.1007/s42114-023-00717-1
12. Lan J, Qu S, Ye X, Zheng Y, Ma M, Guo S, Huang S, Li S, Kang J (2024) Core–shell semiconductor-graphene nanoarchitectures for efficient photocatalysis: state of the art and perspectives. Nano-Micro Lett 16:280. https://doi.org/10.1007/s40820-024-01503-4
13. Tang J, Gao G, Luo W, Dai Q, Wang Y, Elzilal HA, Abo-Dief HM, Algadi H, Zhang J (2023) Z-scheme metal organic framework@graphene oxide composite photocatalysts with enhanced photocatalytic degradation of tetracycline. Adv Compos Hybrid Mater 6:190. https://doi.org/10.1007/s42114-023-00771-9
14. Wang K, Hu Z, Yu P, Balu AM, Li K, Li L, Zeng L, Zhang C, Luque R, Yan K, Luo H (2023) Understanding bridging sites and accelerating quantum efficiency for photocatalytic CO_2 reduction. Nano-Micro Lett 16:5. https://doi.org/10.1007/s40820-023-01221-3
15. Sun Z, Wang M, Fan J, Feng R, Zhou Y, Zhang L (2021) TiO_2@MIL-101(Cr) nanocomposites as an efficient photocatalyst for degradation of toluene. Adv Compos Hybrid Mater 4:1322–1329. https://doi.org/10.1007/s42114-021-00337-7
16. Yue S, Chen L, Zhang M, Liu Z, Chen T, Xie M, Cao Z, Han W (2021) Electrostatic field enhanced photocatalytic CO_2 conversion on $BiVO_4$ nanowires. Nano-Micro Lett 14:15. https://doi.org/10.1007/s40820-021-00749-6
17. Humayun M, Ullah H, Shu L, Ao X, Tahir AA, Wang C, Luo W (2021) Plasmon assisted highly efficient visible light catalytic CO_2 reduction over the noble metal decorated Sr-incorporated g-C_3N_4. Nano-Micro Lett 13:209. https://doi.org/10.1007/s40820-021-00736-x
18. Abou Zeid S, Leprince-Wang Y (2024) Advancements in ZnO-based photocatalysts for water treatment: a comprehensive review. Crystals 14:611. https://doi.org/10.3390/cryst14070611
19. Navidpour AH, Xu B, Ahmed MB, Zhou JL (2024) Immobilization of TiO_2 and ZnO by facile surface engineering methods to improve semiconductor performance in photocatalytic wastewater treatment: A review. Mater Sci Semicond Process 179:108518. https://doi.org/10.1016/j.mssp.2024.108518
20. Navidpour AH, Safaei J, Johir MAH, Ni B-J, Dashti A, Li X, Zhou JL (2024) Zinc oxide@citric acid-modified graphitic carbon nitride nanocomposites for adsorption and photocatalytic degradation of perfluorooctanoic acid. Adv Compos Hybrid Mater 7:53. https://doi.org/10.1007/s42114-024-00867-w
21. Navidpour AH, Hosseinzadeh A, Zhou JL, Huang Z (2023) Progress in the application of surface engineering methods in immobilizing TiO_2 and ZnO coatings for environmental photocatalysis. Catal Rev Sci Eng 65:822–873. https://doi.org/10.1080/01614940.2021.1983066
22. Garg S, Choudhary MK, Kataria J, Sharma S (2025) Biomimetic nanoarchitectonics of Ag@TiO_2/g-C_3N_4: unveiling kinetic and mechanistic pathways for enhanced photocatalysis. Chemosphere 373:144179. https://doi.org/10.1016/j.chemosphere.2025.144179
23. Molar J, Herckes P, Fraser MP (2025) Photocatalytic abatement of ambient NO_x by TiO_2 coated solar panels. RSC Sustain 3:963–972. https://doi.org/10.1039/D4SU00516C
24. Chai M, Yuan B, Ban Y, Guo J, Lou H, Kang H, Zhang Q, Liu Z, Zhang D (2025) Stable synthesis mechanism and photocatalytic properties of TiO_2 nanocrystals with different morphologies derived from potassium titanate nanowires. RSC Adv 15:6384–6399. https://doi.org/10.1039/D4RA08805K
25. Dastider A, Saha H, Anik MJF, Jamal M, Billah MM (2024) Second phase Cu_2O boosted photocatalytic activity of fluorine doped CuO nanoparticles. RSC Adv 14:11677–11693. https://doi.org/10.1039/D3RA08790E
26. Liu Z, Chang X, Shi Y, Zhao X (2025) Synergistic effects of Cu_7S_4@Cu_2O core-shell photocatalyst and S-scheme heterojunction in photocatalytic CO_2 reduction. J Alloys Compd 1010:177572. https://doi.org/10.1016/j.jallcom.2024.177572
27. Kalantarian K, Sheibani S (2024) Enhancement of photocatalytic efficiency of Fe_2O_3 through g-C_3N_4 nanosheet modification for degradation of organic and pharmaceutical pollutants and hydrogen production. Ceram Int 50:42818–42834. https://doi.org/10.1016/j.ceramint.2024.08.127
28. Song H, Zhang S, Cheng S, Fan Z, Gao H, Cheng F (2025) A photocatalytic superhydrophobic coating with p–n type BiOBr/α-Fe_2O_3 heterojunctions applied in NO degradation. RSC Adv 15:832–843. https://doi.org/10.1039/D4RA08085H
29. Florez J, Diaz-Uribe C, Vallejo W, Duran F, Puello E, Salazar J, Zarate X, Schott E (2025) Study of methylene blue removal and photocatalytic degradation on zirconia thin films modified with Mn-Anderson polyoxometalates. Dalton Trans 54:2471–2482. https://doi.org/10.1039/D4DT02782E
30. Aljawrneh B, Ocak YS, Albiss BA, Dwiri A, Tawalbeh M, Al-Othman A (2024) ZrO_2 nanoparticles for effective dye degradation in wastewater: synthesis, characterization, and photocatalytic performance under sunlight. J Alloys Compd 1008:176522. https://doi.org/10.1016/j.jallcom.2024.176522
31. Kanafin YN, Abduvalov A, Kaikanov M, Poulopoulos SG, Atabaev TS (2025) A review on WO_3 photocatalysis used for wastewater treatment and pesticide degradation. Heliyon 11:e40788. https://doi.org/10.1016/j.heliyon.2024.e40788
32. Zhou L, Zhang W, Huang Z, Hu F, Li P, Yao X (2025) Self-assembly strategy for synthesis of WO_3@TCN heterojunction: efficient for photocatalytic degradation and hydrogen production via water splitting. Molecules 30:379. https://doi.org/10.3390/molecules30020379
33. Longchin P, Gebremariam TT, Kunthakudee N, Thoumrungroj A, Sutthiphong T, Hunsom M (2025) Structural modification of defective WO_3 by g-C_3N_4 for photocatalytic gold recovery from non-cyanide-based plating effluent. Sci Rep 15:1806. https://doi.org/10.1038/s41598-024-81928-4
34. Sun X, Ohno T (2024) Synergistic enhancement of hydrogen peroxide generation: WO_3 photocatalyst modified with MXene and Au nanoparticles under visible light. Catal Sci Technol 14:3502–3513. https://doi.org/10.1039/D4CY00443D
35. Giancaspro M, Tancredi M, Di Fonzo RP, Lasala P, Milella A, Bianco GV, Sibillano T, Giannini C, Castaldo R, Gentile G, Dell'Edera M, Dibenedetto CN, De Pasquale I, Comparelli R, Panniello A, Madonia A, Striccoli M, Curri ML, Fanizza E

(2025) Multilevel characterization of SnO_2 nanostructures toward enhanced photocatalytic activity. MRS Bull 50:384–397. https://doi.org/10.1557/s43577-024-00830-6
36. Navidpour AH, Hao D, Li X, Li D, Huang Z, Zhou JL (2024) Key factors in improving the synthesis and properties of visible-light activated g-C_3N_4 for photocatalytic hydrogen production and organic pollutant decomposition. Catal Rev Sci Eng 66:1665–1736. https://doi.org/10.1080/01614940.2023.2228130
37. Jain B, Hashmi A, Sanwaria S, Singh AK, Susan MABH, Singh A (2020) An efficient and stable photocatalyst for water treatment through the Fenton process. Adv Compos Hybrid Mater 3:231–242. https://doi.org/10.1007/s42114-020-00153-5
38. Sun Y, Zhang W, Li Q, Liu H, Wang X (2023) Preparations and applications of zinc oxide based photocatalytic materials. Adv Sens Energy Mater 2:100069. https://doi.org/10.1016/j.asems.2023.100069
39. El Golli A, Contreras S, Dridi C (2023) Bio-synthesized ZnO nanoparticles and sunlight-driven photocatalysis for environmentally-friendly and sustainable route of synthetic petroleum refinery wastewater treatment. Sci Rep 13:20809. https://doi.org/10.1038/s41598-023-47554-2
40. Raha S, Ahmaruzzaman M (2022) ZnO nanostructured materials and their potential applications: progress, challenges and perspectives. Nanoscale Adv 4:1868–1925. https://doi.org/10.1039/D1NA00880C
41. Jiang Z, Liu B, Yu L, Tong Y, Yan M, Zhang R, Han W, Hao Y, Shangguan L, Zhang S, Li W (2023) Research progresses in preparation methods and applications of zinc oxide nanoparticles. J Alloys Compd 956:170316. https://doi.org/10.1016/j.jallcom.2023.170316
42. Turkten N, Bekbolet M (2020) Photocatalytic performance of titanium dioxide and zinc oxide binary system on degradation of humic matter. J Photochem Photobiol A Chem 401:112748. https://doi.org/10.1016/j.jphotochem.2020.112748
43. Garg R, Gupta R, Singh N, Bansal A (2021) Characterization and performance evaluation of synthesized ZnO nanoflowers, nanorods, and their hybrid nanocomposites with graphene oxide for degradation of Orange G. Environ Sci Pollut Res 28:57009–57029. https://doi.org/10.1007/s11356-021-14511-3
44. Resende Leite R, Colombo R, Eduardo Bimbi Júnior F, de Roberto Vasconcelos Lanza M, da Silva Barud H, Ramos Moreira Afonso C, Inês Basso Bernardi M (2024) Precursor effect on the hydrothermal synthesis of pure ZnO nanostructures and enhanced photocatalytic performance for norfloxacin degradation. Chem Eng J 496:154374. https://doi.org/10.1016/j.cej.2024.154374
45. Anju Chanu L, Joychandra Singh W, Jugeshwar Singh K, Nomita Devi K (2019) Effect of operational parameters on the photocatalytic degradation of methylene blue dye solution using manganese doped ZnO nanoparticles. Results Phys 12:1230–1237. https://doi.org/10.1016/j.rinp.2018.12.089
46. Bhapkar A, Prasad R, Jaspal D, Shirolkar M, Gheisari K, Bhame S (2023) Visible light driven photocatalytic degradation of methylene blue by ZnO nanostructures synthesized by glycine nitrate auto combustion route. Inorg Chem Commun 148:110311. https://doi.org/10.1016/j.inoche.2022.110311
47. Modi S, Yadav VK, Amari A, Alyami AY, Gacem A, Harharah HN, Fulekar MH (2023) Photocatalytic degradation of methylene blue dye from wastewater by using doped zinc oxide nanoparticles. Water 15:2275. https://doi.org/10.3390/w15122275
48. Dao TT, Le Na Vo T, Duong AT, Tran DT, Nguyen DL, Pham VV, Das R, Nguyen HT (2023) Highly photocatalytic activity of pH-controlled ZnO nanoflakes. Opt Mater 140:113865. https://doi.org/10.1016/j.optmat.2023.113865
49. Pavithra NS, Lingaraju K, Raghu GK, Nagaraju G (2017) *Citrus maxima* (Pomelo) juice mediated eco-friendly synthesis of ZnO nanoparticles: applications to photocatalytic, electrochemical sensor and antibacterial activities. Spectrochim Acta A Mol Biomol Spectrosc 185:11–19. https://doi.org/10.1016/j.saa.2017.05.032
50. Kalantari Bolaghi Z, Masoudpanah SM, Hasheminiasari M (2018) Photocatalytic properties of ZnO powders synthesized by conventional and microwave-assisted solution combustion method. J Sol-Gel Sci Technol 86:711–718. https://doi.org/10.1007/s10971-018-4658-2
51. Kazeminezhad I, Sadollahkhani A (2016) Influence of pH on the photocatalytic activity of ZnO nanoparticles. J Mater Sci Mater Electron 27:4206–4215. https://doi.org/10.1007/s10854-016-4284-0
52. Benhebal H, Chaib M, Salmon T, Geens J, Leonard A, Lambert SD, Crine M, Heinrichs B (2013) Photocatalytic degradation of phenol and benzoic acid using zinc oxide powders prepared by the sol–gel process. Alex Eng J 52:517–523. https://doi.org/10.1016/j.aej.2013.04.005
53. Sin J-C, Lam S-M, Lee K-T, Mohamed AR (2013) Preparation and photocatalytic properties of visible light-driven samarium-doped ZnO nanorods. Ceram Int 39:5833–5843. https://doi.org/10.1016/j.ceramint.2013.01.004
54. Zong Y, Li Z, Wang X, Ma J, Men Y (2014) Synthesis and high photocatalytic activity of Eu-doped ZnO nanoparticles. Ceram Int 40:10375–10382. https://doi.org/10.1016/j.ceramint.2014.02.123
55. Mohamed Isa ED, Che Jusoh NW, Hazan R, Shameli K (2021) Photocatalytic degradation of methyl orange using pullulan-mediated porous zinc oxide microflowers. Environ Sci Pollut Res 28:5774–5785. https://doi.org/10.1007/s11356-020-10939-1
56. Chen X, Wu Z, Liu D, Gao Z (2017) Preparation of ZnO photocatalyst for the efficient and rapid photocatalytic degradation of azo dyes. Nanoscale Res Lett 12:143. https://doi.org/10.1186/s11671-017-1904-4
57. Meena PL, Poswal K, Surela AK (2022) Facile synthesis of ZnO nanoparticles for the effective photodegradation of malachite green dye in aqueous solution. Water Environ J 36:513–524. https://doi.org/10.1111/wej.12783
58. C V, Prabha MNC, Raj MALA (2016) Green mediated synthesis of zinc oxide nanoparticles for the photocatalytic degradation of rose bengal dye. Environmental Nanotechnology, Monitoring & Management 6:134–138. https://doi.org/10.1016/j.enmm.2016.09.004
59. Rani S, Sharma A, Tabasum S, Malik AQ, Chaudhary S, Kumar D, Singh H, Singh PP (2023) Highly efficient photocatalytic properties of La-doped ZnO over pristine ZnO for degradation of 2-chlorophenol from aquatic agriculture waste. Chem Afr 6:1981–1990. https://doi.org/10.1007/s42250-023-00630-6
60. Evgenidou E, Fytianos K, Poulios I (2005) Semiconductor-sensitized photodegradation of dichlorvos in water using TiO_2 and ZnO as catalysts. Appl Catal B: Environ Energy 59:81–89. https://doi.org/10.1016/j.apcatb.2005.01.005
61. Daneshvar N, Aber S, Seyed Dorraji MS, Khataee AR, Rasoulifard MH (2007) Photocatalytic degradation of the insecticide diazinon in the presence of prepared nanocrystalline ZnO powders under irradiation of UV-C light. Sep Purif Technol 58:91–98. https://doi.org/10.1016/j.seppur.2007.07.016
62. Kansal SK, Kaur N, Singh S (2009) Photocatalytic degradation of two commercial reactive dyes in aqueous phase using nanophotocatalysts. Nanoscale Res Lett 4:709. https://doi.org/10.1007/s11671-009-9300-3
63. Sin J-C, Lam S-M, Lee K-T, Mohamed AR (2013) Photocatalytic performance of novel samarium-doped spherical-like ZnO hierarchical nanostructures under visible light irradiation for 2,4-dichlorophenol degradation. J Colloid Interface Sci 401:40–49. https://doi.org/10.1016/j.jcis.2013.03.043
64. Anandan S, Vinu A, Sheeja Lovely KLP, Gokulakrishnan N, Srinivasu P, Mori T, Murugesan V, Sivamurugan V, Ariga K

(2007) Photocatalytic activity of La-doped ZnO for the degradation of monocrotophos in aqueous suspension. J Mol Catal A: Chem 266:149–157. https://doi.org/10.1016/j.molcata.2006.11.008
65. Zhu C, Li Y, Yang Y, Chen Y, Yang Z, Wang P, Feng W (2020) Influence of operational parameters on photocatalytic decolorization of a cationic azo dye under visible-light in aqueous Ag_3PO_4. Inorg Chem Commun 115:107850. https://doi.org/10.1016/j.inoche.2020.107850
66. Ye Y, Feng Y, Bruning H, Yntema D, Rijnaarts HHM (2018) Photocatalytic degradation of metoprolol by TiO_2 nanotube arrays and UV-LED: effects of catalyst properties, operational parameters, commonly present water constituents, and photo-induced reactive species. Appl Catal B: Environ Energy 220:171–181. https://doi.org/10.1016/j.apcatb.2017.08.040
67. Sohrabi S, Akhlaghian F (2016) Modeling and optimization of phenol degradation over copper-doped titanium dioxide photocatalyst using response surface methodology. Process Saf Environ Prot 99:120–128. https://doi.org/10.1016/j.psep.2015.10.016
68. Sin J-C, Lam S-M, Mohamed AR (2011) Optimizing photocatalytic degradation of phenol by TiO_2/GAC using response surface methodology. Korean J Chem Eng 28:84–92. https://doi.org/10.1007/s11814-010-0318-0
69. Chen J, Li G, Huang Y, Zhang H, Zhao H, An T (2012) Optimization synthesis of carbon nanotubes-anatase TiO_2 composite photocatalyst by response surface methodology for photocatalytic degradation of gaseous styrene. Appl Catal B: Environ Energy 123–124:69–77. https://doi.org/10.1016/j.apcatb.2012.04.020
70. Abdullah AH, Moey HJM, Yusof NA (2012) Response surface methodology analysis of the photocatalytic removal of methylene blue using bismuth vanadate prepared via polyol route. J Environ Sci 24:1694–1701. https://doi.org/10.1016/S1001-0742(11)60966-2
71. Liu H-L, Chiou Y-R (2005) Optimal decolorization efficiency of reactive red 239 by UV/TiO_2 photocatalytic process coupled with response surface methodology. Chem Eng J 112:173–179. https://doi.org/10.1016/j.cej.2005.07.012
72. Ayodele BV, Alsaffar MA, Mustapa SI, Cheng CK, Witoon T (2021) Modeling the effect of process parameters on the photocatalytic degradation of organic pollutants using artificial neural networks. Process Saf Environ Prot 145:120–132. https://doi.org/10.1016/j.psep.2020.07.053
73. Oladipo AA, Vaziri R, Abureesh MA (2018) Highly robust $AgIO_3$/MIL-53 (Fe) nanohybrid composites for degradation of organophosphorus pesticides in single and binary systems: application of artificial neural networks modelling. J Taiwan Inst Chem Eng 83:133–142. https://doi.org/10.1016/j.jtice.2017.12.013
74. Liu D, Sun N (2023) Prospects of artificial intelligence in the development of sustainable separation processes. Front Sustain 4:1210209. https://doi.org/10.3389/frsus.2023.1210209
75. Saad AH, Nahazanan H, Yusuf B, Toha SF, Alnuaim A, El-Mouchi A, Elseknidy M, Mohammed AA (2023) A systematic review of machine learning techniques and applications in soil improvement using green materials. Sustainability 15:9738. https://doi.org/10.3390/su15129738
76. 76. Dashti A, Navidpour AH, Amirkhani F, Zhou JL, Altaee A (2024) Application of machine learning models to improve the prediction of pesticide photodegradation in water by ZnO-based photocatalysts. Chemosphere 362:142792. https://doi.org/10.1016/j.chemosphere.2024.142792
77. 77. Hashimoto DA, Witkowski E, Gao L, Meireles O, Rosman G (2020) Artificial intelligence in anesthesiology: Current techniques, clinical applications, and limitations. Anesthesiology 132:379–394.
78. Dashti A, Raji M, Riasat Harami H, Zhou JL, Asghari M (2023) Biochar performance evaluation for heavy metals removal from industrial wastewater based on machine learning: application for environmental protection. Sep Purif Technol 312:123399. https://doi.org/10.1016/j.seppur.2023.123399
79. 79. Ahmed SF, Alam MSB, Hassan M, Rozbu MR, Ishtiak T, Rafa N, Mofijur M, Shawkat Ali ABM, Gandomi AH (2023) Deep learning modelling techniques: current progress, applications, advantages, and challenges. Artif Intell Rev 56:13521–13617. https://doi.org/10.1007/s10462-023-10466-8
80. 80. Dashti A, Noushabadi AS, Asadi J, Raji M, Chofreh AG, Klemeš JJ, Mohammadi AH (2021) Review of higher heating value of municipal solid waste based on analysis and smart modelling. Renew Sustain Energy Rev 151:111591. https://doi.org/10.1016/j.rser.2021.111591
81. Schlexer Lamoureux P, Winther KT, Garrido Torres JA, Streibel V, Zhao M, Bajdich M, Abild-Pedersen F, Bligaard T (2019) Machine learning for computational heterogeneous catalysis. ChemCatChem 11:3581–3601. https://doi.org/10.1002/cctc.201900595
82. Marinho BA, Suhadolnik L, Likozar B, Huš M, Marinko Ž, Čeh M (2022) Analytical methods, mechanisms, simulations, catalysts and reactors. J Clean Prod 343:131061. https://doi.org/10.1016/j.jclepro.2022.131061
83. Alshurideh M, Al Kurdi B, Salloum SA, Arpaci I, Al-Emran M (2023) A comparative approach using PLS-SEM and machine learning algorithms. Interact Learn Environ 31:1214–1228. https://doi.org/10.1080/10494820.2020.1826982
84. Lowe M, Qin R, Mao X (2022) A review on machine learning, artificial intelligence, and smart technology in water treatment and monitoring. Water 14:1384. https://doi.org/10.3390/w14091384
85. Ye Z, Yang J, Zhong N, Tu X, Jia J, Wang J (2020) A review. Sci Total Environ 699:134279. https://doi.org/10.1016/j.scitotenv.2019.134279
86. 86. Ayodele BV, Alsaffar MA, Mustapa SI, Vo D-VN (2020) Backpropagation neural networks modelling of photocatalytic degradation of organic pollutants using TiO_2-based photocatalysts. J Chem Technol Biotechnol 95:2739–2749. https://doi.org/10.1002/jctb.6407
87. Gheytanzadeh M, Baghban A, Habibzadeh S, Jabbour K, Esmaeili A, Mohaddespour A, Abida O (2022) An insight into tetracycline photocatalytic degradation by MOFs using the artificial intelligence technique. Sci Rep 12:6615. https://doi.org/10.1038/s41598-022-10563-8
88. Kitchamsetti N, de Barros ALF (2023) Synthesis, properties and photocatalytic removal of organic contaminants from wastewater. ChemCatChem 15:e202300690. https://doi.org/10.1002/cctc.202300690
89. Mohammadzadeh Kakhki R, Zirjanizadeh S, Mohammadpoor M (2023) In time of artificial intelligence. J Mater Sci 58:10555–10575. https://doi.org/10.1007/s10853-023-08643-9
90. 90. Yadav S, Shakya K, Gupta A, Singh D, Chandran AR, Varayil Aanappalli A, Goyal K, Rani N, Saini K (2023) A review on degradation of organic dyes by using metal oxide semiconductors. Environ Sci Pollut Res 30:71912–71932. https://doi.org/10.1007/s11356-022-20818-6
91. Zhao L, Dai T, Qiao Z, Sun P, Hao J, Yang Y (2020) Application of artificial intelligence to wastewater treatment: a bibliometric analysis and systematic review of technology, economy, management, and wastewater reuse. Process Saf Environ Prot 133:169–182. https://doi.org/10.1016/j.psep.2019.11.014
92. Sundui B, Ramirez Calderon OA, Abdeldayem OM, Lázaro-Gil J, Rene ER, Sambuu U (2021) Applications of machine learning algorithms for biological wastewater treatment: updates and perspectives. Clean Technol Environ Policy 23:127–143. https://doi.org/10.1007/s10098-020-01993-x

93. Pattnaik A, Sahu JN, Poonia AK, Ghosh P (2023) Current perspective of nano-engineered metal oxide based photocatalysts in advanced oxidation processes for degradation of organic pollutants in wastewater. Chem Eng Res Des 190:667–686. https://doi.org/10.1016/j.cherd.2023.01.014
94. 94. Martini S, Roni KA (2021) The existing technology and the application of digital artificial intelligent in the wastewater treatment area: A review paper. J Phys: Conf Ser 1858:012013.
95. Frontistis Z, Lykogiannis G, Sarmpanis A (2023) Machine learning implementation in membrane bioreactor systems: progress, challenges, and future perspectives: a review. Environments 10:127. https://doi.org/10.3390/environments10070127
96. Ren G, Han H, Wang Y, Liu S, Zhao J, Meng X, Li Z (2021) Recent advances of photocatalytic application in water treatment: a review. Nanomaterials 11:1804. https://doi.org/10.3390/nano11071804
97. Anandhi G, Iyapparaja M (2024) Photocatalytic degradation of drugs and dyes using a maching learning approach. RSC Adv 14:9003–9019. https://doi.org/10.1039/D4RA00711E
98. Zulkifli SN, Rahim HA, Lau W-J (2018) Detection of contaminants in water supply: a review on state-of-the-art monitoring technologies and their applications. Sensors and Actuators B: Chemical 255:2657–2689. https://doi.org/10.1016/j.snb.2017.09.078
99. Uwamungu JY, Kumar P, Alkhayyat A, Younas T, Capangpangan RY, Alguno AC, Ofori I (2022) Future of water/wastewater treatment and management by industry 4.0 integrated nanocomposite manufacturing. J Nanomater 2022:5316228. https://doi.org/10.1155/2022/5316228
100. Altowayti WA, Shahir S, Othman N, Eisa TA, Yafooz WMS, Al-Dhaqm A, Soon CY, Yahya IB, Che Rahim NA, Abaker M, Ali A (2022) The role of conventional methods and artificial intelligence in the wastewater treatment: a comprehensive review. Processes 10:1832. https://doi.org/10.3390/pr10091832
101. Zhou P, Wang M, Tang F, Ling L, Yu H, Chen X (2024) Machine learning accelerates the screening of efficient metal-oxide catalysts for photocatalytic water splitting. Mater Res Bull 179:112956. https://doi.org/10.1016/j.materresbull.2024.112956
102. Masood H, Toe CY, Teoh WY, Sethu V, Amal R (2019) Machine learning for accelerated discovery of solar photocatalysts. ACS Catal 9:11774–11787. https://doi.org/10.1021/acscatal.9b02531
103. Kumar R, Singh AK (2021) Chemical hardness-driven interpretable machine learning approach for rapid search of photocatalysts. NPJ Comput Mater 7:197. https://doi.org/10.1038/s41524-021-00669-4
104. Wang Y, Sorkun MC, Brocks G, Er S (2024) ML-aided computational screening of 2D materials for photocatalytic water splitting. J Phys Chem Lett 15:4983–4991. https://doi.org/10.1021/acs.jpclett.4c00425
105. Wen X, Geng X, Su G, Li Y, Li Q, Yi Y, Liu L (2025) Machine learning-driven design of single-atom catalysts for carbon dioxide valorization to high-value chemicals: a review of photocatalysis, electrocatalysis, and thermocatalysis. Green Chem 27:4898–4925. https://doi.org/10.1039/D5GC00739A
106. Mai H, Li X, Le TC, Russo SP, Winkler DA, Chen D, Caruso RA (2025) Rapid design of efficient Mn_3O_4-based photocatalysts by machine learning and density functional theory calculations. Adv Energy Sustain Res 6:2400397. https://doi.org/10.1002/aesr.202400397
107. Allam O, Maghsoodi M, Jang SS, Snow SD (2024) Unveiling competitive adsorption in TiO_2 photocatalysis through machine-learning-accelerated molecular dynamics, DFT, and experimental methods. ACS Appl Mater Interfaces 16:36215–36223. https://doi.org/10.1021/acsami.4c02334
108. K C A, Rao CS, Nair V (2024) Combination of ensemble machine learning models in photocatalytic studies using nano TiO_2 - Lignin based biochar. Chemosphere 352:141326. https://doi.org/10.1016/j.chemosphere.2024.141326
109. Al-Gheethi A, Sundram N, Crane R, Alburihi A, Mohamed RMSR, Al-Shaibani MM, Noman EA, Ponnusamy SK, Kamil NAFM (2022) Metronidazole photocatalytic degradation by zinc oxide nanoparticles synthesized in watermelon peel extract; advanced optimization, simulation and numerical models using machine learning applications. Environ Res 212:113537. https://doi.org/10.1016/j.envres.2022.113537
110. Akyildiz HI, Yigit E, Arat AB, Islam S (2024) A machine learning approach for the estimation of photocatalytic activity of ALD ZnO thin films on fabric substrates. J Photochem Photobiol A Chem 448:115308. https://doi.org/10.1016/j.jphotochem.2023.115308
111. Chelghoum H, Nasrallah N, Tahraoui H, Seleiman MF, Bouhenna MM, Belmeskine H, Zamouche M, Djema S, Zhang J, Mendil A, Dergal F, Kebir M, Amrane A (2024) Eco-friendly synthesis of ZnO nanoparticles for quinoline dye photodegradation and antibacterial applications using advanced machine learning models. Catalysts 14:831. https://doi.org/10.3390/catal14110831
112. A G, T M, S N (2024) Machine learning, a powerful tool for the prediction of $BiVO_4$ nanoparticles efficiency in photocatalytic degradation of organic dyes. J Environ Sci Health A 59:15–24. https://doi.org/10.1080/10934529.2024.2319510
113. Yurova VY, Potapenko KO, Aliev TA, Kozlova EA, Skorb EV (2024) Optimization of g-C_3N_4 synthesis parameters based on machine learning to predict the efficiency of photocatalytic hydrogen production. Int J Hydrog Energy 81:193–203. https://doi.org/10.1016/j.ijhydene.2024.07.245
114. Song C, Shi Y, Li M, He Y, Xiong X, Deng H, Xia D (2024) Prediction of g–C_3N_4–based photocatalysts in tetracycline degradation based on machine learning. Chemosphere 362:142632. https://doi.org/10.1016/j.chemosphere.2024.142632
115. Arabacı B, Bakır R, Orak C, Yüksel A (2025) Predictive modeling of photocatalytic hydrogen production: integrating experimental insights with machine learning on Fe/g-C_3N_4 catalysts. Ind Eng Chem Res 64:5184–5199. https://doi.org/10.1021/acs.iecr.4c03919
116. Liang X, Yu S, Meng B, Ju Y, Wang S, Wang Y (2025) Machine-learning-guided design of nanostructured metal oxide photoanodes for photoelectrochemical water splitting: from material discovery to performance optimization. Nanomaterials 15:948. https://doi.org/10.3390/nano15120948
117. Daneshvar N, Salari D, Khataee AR (2004) Photocatalytic degradation of azo dye acid red 14 in water on ZnO as an alternative catalyst to TiO_2. J Photochem Photobiol A Chem 162:317–322. https://doi.org/10.1016/S1010-6030(03)00378-2
118. Zhang H, Zong R, Zhu Y (2009) Photocorrosion inhibition and photoactivity enhancement for zinc oxide via hybridization with monolayer polyaniline. J Phys Chem C 113:4605–4611. https://doi.org/10.1021/jp810748u
119. Belver C, Bedia J, Gómez-Avilés A, Peñas-Garzón M, Rodriguez JJ (2019) Chap. 22 - Semiconductor Photocatalysis for Water Purification. In: Thomas S, Pasquini D, Leu S-Y, Gopakumar DA (eds) Nanoscale Materials in Water Purification. Elsevier, pp 581–651
120. Jandaghian F, Ebrahimian Pirbazari A, Tavakoli O, Asasian-Kolur N, Sharifian S (2023) Comparison of the performance of Ag-deposited ZnO and TiO_2 nanoparticles in levofloxacin degradation under UV/visible radiation. J Hazard Mater Adv 9:100240. https://doi.org/10.1016/j.hazadv.2023.100240
121. Sanusi I, Almquist CB (2023) ZnO/TiO_2 composite thin-film photocatalysts for gas-phase oxidation of ethanol. Catalysts 13:1203. https://doi.org/10.3390/catal13081203
122. Li X, Yu J, Jaroniec M (2016) Hierarchical photocatalysts. Chem Soc Rev 45:2603–2636. https://doi.org/10.1039/C5CS00838G

123. Sakthivel S, Neppolian B, Shankar MV, Arabindoo B, Palanichamy M, Murugesan V (2003) Solar photocatalytic degradation of azo dye: comparison of photocatalytic efficiency of ZnO and TiO_2. Sol Energy Mater Sol Cells 77:65–82. https://doi.org/10.1016/S0927-0248(02)00255-6
124. Zagorac D, Schön J, Stojanović N, Matovic B (2018) ZnO/ZnS (hetero)structures: ab initio investigations of polytypic behavior of mixed ZnO and ZnS compounds. Acta Crystallogr B Struct Sci Cryst Eng Mater 74:628–642. https://doi.org/10.1107/S2052520618014099
125. Özgür Ü, Alivov YI, Liu C, Teke A, Reshchikov MA, Doğan S, Avrutin V, Cho SJ, Morkoç H (2005) A comprehensive review of ZnO materials and devices. J Appl Phys 98:041301. https://doi.org/10.1063/1.1992666
126. Lee KM, Lai CW, Ngai KS, Juan JC (2016) Recent developments of zinc oxide based photocatalyst in water treatment technology: a review. Water Res 88:428–448. https://doi.org/10.1016/j.watres.2015.09.045
127. Jiang J, Pi J, Cai J (2018) The advancing of zinc oxide nanoparticles for biomedical applications. Bioinorg Chem Appl 2018:18. https://doi.org/10.1155/2018/1062562
128. Tiwari V, Mishra N, Gadani K, Solanki PS, Shah NA, Tiwari M (2018) Mechanism of anti-bacterial activity of zinc oxide nanoparticle against carbapenem-resistant *Acinetobacter baumannii*. Front Microbiol 9:1218. https://doi.org/10.3389/fmicb.2018.01218
129. Mahmoud SA, Fouad OA (2015) Synthesis and application of zinc/tin oxide nanostructures in photocatalysis and dye sensitized solar cells. Sol Energy Mater Sol Cells 136:38–43. https://doi.org/10.1016/j.solmat.2014.12.035
130. Cun T, Dong C, Huang Q (2016) Ionothermal precipitation of highly dispersive ZnO nanoparticles with improved photocatalytic performance. Appl Surf Sci 384:73–82. https://doi.org/10.1016/j.apsusc.2016.05.008
131. Abbas KN, Bidin N (2017) Morphological driven photocatalytic activity of ZnO nanostructures. Appl Surf Sci 394:498–508. https://doi.org/10.1016/j.apsusc.2016.10.080
132. Espitia P, Soares N, Coimbra J, Andrade N, Cruz R, Medeiros E (2012) Zinc oxide nanoparticles: synthesis, antimicrobial activity and food packaging applications. Food Bioprocess Technol 5:1447–1464. https://doi.org/10.1007/s11947-012-0797-6
133. Fan B, Zhang Y, Yan R, Fan J (2016) Multistage growth of monocrystalline ZnO nanowires and twin-nanorods: oriented attachment and role of the spontaneous polarization force. CrystEngComm 18:6492–6501. https://doi.org/10.1039/C6CE01337F
134. Ashrafi A, Jagadish C (2007) Review of zincblende ZnO: stability of metastable ZnO phases. J Appl Phys 102:071101. https://doi.org/10.1063/1.2787957
135. Rajbongshi BM, Samdarshi SK (2014) Cobalt-doped zincblende–wurtzite mixed-phase ZnO photocatalyst nanoparticles with high activity in visible spectrum. Appl Catal B Environ Energy 144:435–441. https://doi.org/10.1016/j.apcatb.2013.07.048
136. Cataño FA, Valencia S, Hincapié EA, Restrepo G, Marín JM (2012) A comparative study between TiO_2 and ZnO photocatalysis: photocatalytic degradation of cibacron yellow FN-2R dye. Lat Am Appl Res 42:33–38
137. Djilali T, Lebouachera SEI, Dechir S, Chekir N, Benhabiles O, Bentahar F (2016) Comparison between TiO_2 and ZnO photocatalytic efficiency for the degradation of tartrazine contaminant in water. Int J Environ Sci Technol 1:357–364
138. Shinde D, Tambade P, Chaskar M, Gadave K (2017) Photocatalytic degradation of dyes in water by analytical reagent grades ZnO, TiO_2 and SnO_2: a comparative study. Drink Water Eng Sci 10:109–117. https://doi.org/10.5194/dwes-10-109-2017
139. Raliya R, Avery C, Chakrabarti S, Biswas P (2017) Photocatalytic degradation of methyl orange dye by pristine titanium dioxide, zinc oxide, and graphene oxide nanostructures and their composites under visible light irradiation. Appl Nanosci 7:253–259. https://doi.org/10.1007/s13204-017-0565-z
140. Kusaba K, Syono Y, Kikegawa T (1999) Phase transition of ZnO under high pressure and temperature. Proceedings of the Japan Academy, Series B 75:1–6. https://doi.org/10.2183/pjab.75.1
141. Razavi-Khosroshahi H, Edalati K, Wu J, Nakashima Y, Arita M, Ikoma Y, Sadakiyo M, Inagaki Y, Staykov A, Yamauchi M, Horita Z, Fuji M (2017) High-pressure zinc oxide phase as visible-light-active photocatalyst with narrow band gap. J Mater Chem A 5:20298–20303. https://doi.org/10.1039/C7TA05262F
142. Gonzalez J, Marquina J, Rodríguez F, Valiente R (2009) Nanocrystals of ZnO formed by the hot isostatic pressure method. High Press Res 29:594–599. https://doi.org/10.1080/08957950903417451
143. Decremps F, Zhang J, Liebermann RC (2000) New phase boundary and high-pressure thermoelasticity of ZnO. EPL 51:268–274
144. Baranov AN, Sokolov PS, Tafeenko VA, Lathe C, Zubavichus YV, Veligzhanin AA, Chukichev MV, Solozhenko VL (2013) Nanocrystallinity as a route to metastable phases: rock salt ZnO. Chem Mater 25:1775–1782. https://doi.org/10.1021/cm400293j
145. Koster RS, Fang CM, Dijkstra M, van Blaaderen A, van Huis MA (2015) Stabilization of rock salt ZnO nanocrystals by low-energy surfaces and Mg additions: a first-principles study. J Phys Chem C 119:5648–5656. https://doi.org/10.1021/jp511503b
146. Jiang JZ, Olsen JS, Gerward L, Frost D, Rubie D, Peyronneau J (2000) Structural stability in nanocrystalline ZnO. Europhysics Letters (EPL) 50:48–53
147. Yuan HT, Liu YZ, Mei ZX, Zeng ZQ, Guo Y, Du XL, Jia JF, Zhang Z, Xue QK (2010) Metastable rocksalt ZnO interfacial layer and its influence on polarity selection of Zn-polar ZnO films. J Cryst Growth 312:263–266. https://doi.org/10.1016/j.jcrysgro.2009.10.054
148. Goyal A, Stevanović V (2018) Metastable rocksalt ZnO is p-type dopable. Phys Rev Mater 2:084603. https://doi.org/10.1103/PhysRevMaterials.2.084603
149. Shundo Y, Tam Nguyen T, Akrami S, Edalati P, Itagoe Y, Ishihara T, Arita M, Guo Q, Fuji M, Edalati K (2024) Oxygen vacancy-rich high-pressure rocksalt phase of zinc oxide for enhanced photocatalytic hydrogen evolution. J Colloid Interface Sci 666:22–34. https://doi.org/10.1016/j.jcis.2024.04.010
150. Muñoz-Aguirre N, Martínez-Pérez L, Muñoz-Aguirre S, Flores-Herrera LA, Vergara Hernández E, Zelaya-Angel O (2019) Luminescent properties of (004) highly oriented cubic zinc blende ZnO thin films. Materials 12:3314. https://doi.org/10.3390/ma12203314
151. Ong CB, Ng LY, Mohammad AW (2018) A review of ZnO nanoparticles as solar photocatalysts: synthesis, mechanisms and applications. Renew Sustain Energy Rev 81:536–551. https://doi.org/10.1016/j.rser.2017.08.020
152. Gautam P, Gupta S, Siddiqui I, Lin W-Z, Sharma D, Ranjan A, Tai N-H, Lu M-Y, Jou J-H (2024) 0, 1, 2, and 3-dimensional zinc oxides enabling high-efficiency OLEDs. Chem Eng J 495:153220. https://doi.org/10.1016/j.cej.2024.153220
153. Mekuye B, Abera B (2023) Nanomaterials: an overview of synthesis, classification, characterization, and applications. Nano Select 4:486–501. https://doi.org/10.1002/nano.202300038
154. Goh PS, Wong KC, Ismail AF (2020) Nanocomposite membranes for liquid and gas separations from the perspective of nanostructure dimensions. Membranes 10:297. https://doi.org/10.3390/membranes10100297
155. Moshfegh AZ (2009) Nanoparticle catalysts. J Phys D: Appl Phys 42:233001
156. Sangpour P, Roozbehi M, Akhavan O, Moshfegh A (2009) *ZnO* nanowires from nanopillars: influence of growth time. Curr

Nanosci 5:479–484. https://doi.org/10.2174/157341309789377998
157. Byakodi M, Shrikrishna NS, Sharma R, Bhansali S, Mishra Y, Kaushik A, Gandhi S (2022) Emerging 0D, 1D, 2D, and 3D nanostructures for efficient point-of-care biosensing. Biosens Bioelectron: X 12:100284. https://doi.org/10.1016/j.biosx.2022.100284
158. Samadi M, Zirak M, Naseri A, Kheirabadi M, Ebrahimi M, Moshfegh AZ (2019) Design and tailoring of one-dimensional *ZnO* nanomaterials for photocatalytic degradation of organic dyes: a review. Res Chem Intermed 45:2197–2254. https://doi.org/10.1007/s11164-018-03729-5
159. Anh D, Phuong H, Hoang Thi Huong T, Ha N, Nguyen Xuan H (2011) Crystal structures and properties of *ZnO* nanopowders prepared by ultrasonic method. e-J Surf Sci Nanotech 9:482–485
160. Shende P, Kasture P, Gaud RS (2018) Nanoflowers: the future trend of nanotechnology for multi-applications. Artif Cells Nanomed Biotechnol 46:413–422. https://doi.org/10.1080/21691401.2018.1428812
161. Qu Y, Huang R, Qi W, Shi M, Su R, He Z (2019) Controllable synthesis of *ZnO* nanoflowers with structure-dependent photocatalytic activity. Catal Today 355:397–407. https://doi.org/10.1016/j.cattod.2019.07.056
162. Esbergenova A, Yusupov M, Ghasemitarei M, Jalolov R, Hojamberdiev M, Shaislamov U (2023) Understanding the effect of morphological change on photocatalytic activity of *ZnO* nanostructures and reaction mechanism by molecular dynamics. Colloids Surf A Physicochem Eng Asp 677:132386. https://doi.org/10.1016/j.colsurfa.2023.132386
163. Mourya AK, Singh RP, Kumar T, Talmale AS, Gaikwad GS, Wankhade AV (2023) Tuning the morphologies of ZnO for enhanced photocatalytic activity. Inorg Chem Commun 154:110850. https://doi.org/10.1016/j.inoche.2023.110850
164. Kedruk YY, Contestabile A, Zeng J, Fontana M, Laurenti M, Gritsenko LV, Cicero G, Pirri CF, Abdullin KA (2023) Morphology effects on electro- and photo-catalytic properties of zinc oxide nanostructures. Nanomaterials 13:2527. https://doi.org/10.3390/nano13182527
165. Tuc Altaf C, Colak TO, Rostas AM, Popa A, Toloman D, Suciu M, Demirci Sankir N, Sankir M (2023) Impact on the photocatalytic dye degradation of morphology and annealing-induced defects in zinc oxide nanostructures. ACS Omega 8:14952–14964. https://doi.org/10.1021/acsomega.2c07412
166. Samadi M, Zirak M, Naseri A, Khorashadizade E, Moshfegh AZ (2016) Recent progress on doped ZnO nanostructures for visible-light photocatalysis. Thin Solid Films 605:2–19. https://doi.org/10.1016/j.tsf.2015.12.064
167. Sanakousar FM, Vidyasagar CC, Jiménez-Pérez VM, Prakash K (2022) Recent progress on visible-light-driven metal and non-metal doped ZnO nanostructures for photocatalytic degradation of organic pollutants. Mater Sci Semicond Process 140:106390. https://doi.org/10.1016/j.mssp.2021.106390
168. Nguyen LTT, Nguyen LTH, Duong ATT, Nguyen BD, Quang Hai N, Chu VH, Nguyen TD, Bach LG (2019) Preparation, characterization and photocatalytic activity of La-doped zinc oxide nanoparticles. Materials 12:1195. https://doi.org/10.3390/ma12081195
169. Samadi M, Shivaee HA, Zanetti M, Pourjavadi A, Moshfegh A (2012) Visible light photocatalytic activity of novel MWCNT-doped ZnO electrospun nanofibers. J Mol Catal A Chem 359:42–48. https://doi.org/10.1016/j.molcata.2012.03.019
170. Rezaei M, Habibi-Yangjeh A (2013) Simple and large scale refluxing method for preparation of Ce-doped ZnO nanostructures as highly efficient photocatalyst. Appl Surf Sci 265:591–596. https://doi.org/10.1016/j.apsusc.2012.11.053
171. Mohan R, Krishnamoorthy K, Kim S-J (2012) Enhanced photocatalytic activity of Cu-doped ZnO nanorods. Solid State Commun 152:375–380. https://doi.org/10.1016/j.ssc.2011.12.008
172. Kadam AN, Kim TG, Shin DS, Garadkar KM, Park J (2017) Morphological evolution of Cu doped ZnO for enhancement of photocatalytic activity. J Alloys Compd 710:102–113. https://doi.org/10.1016/j.jallcom.2017.03.150
173. Pandian L, Rajasekaran R, Govindan P (2018) Synthesis, characterization and application of Cu doped ZnO nanocatalyst for photocatalytic ozonation of textile dye and study of its reusability. Mater Res Express 5:115505
174. Abdel-wahab MS, Jilani A, Yahia IS, Al-Ghamdi AA (2016) Enhanced the photocatalytic activity of Ni-doped ZnO thin films: morphological, optical and XPS analysis. Superlattices Microstruct 94:108–118. https://doi.org/10.1016/j.spmi.2016.03.043
175. Sridevi D, Rajendran KV (2011) Photocatalytic activity of pure and Ni-doped ZnO nanoparticles. Int J Nanoparticles 4:381–388. https://doi.org/10.1504/IJNP.2011.043500
176. Zhao J, Wang L, Yan X, Yang Y, Lei Y, Zhou J, Huang Y, Gu Y, Zhang Y (2011) Structure and photocatalytic activity of Ni-doped ZnO nanorods. Mater Res Bull 46:1207–1210. https://doi.org/10.1016/j.materresbull.2011.04.008
177. Putri NA, Fauzia V, Iwan S, Roza L, Umar AA, Budi S (2018) Mn-doping-induced photocatalytic activity enhancement of ZnO nanorods prepared on glass substrates. Appl Surf Sci 439:285–297. https://doi.org/10.1016/j.apsusc.2017.12.246
178. Voicu G, Oprea O, Vasile B, Andronescu E (2013) Photoluminescence and photocatalytic activity of Mn-doped ZnO nanoparticles. Dig J Nanomater Biostruct 8:667–675
179. Achouri F, Corbel S, Balan L, Mozet K, Girot E, Medjahdi G, Said MB M, Ghrabi A, Schneider R (2016) Porous Mn-doped ZnO nanoparticles for enhanced solar and visible light photocatalysis. Mater Des 101:309–316. https://doi.org/10.1016/j.matdes.2016.04.015
180. Nguyen SN, Truong TK, You S-J, Wang Y-F, Cao TM TM, Pham VV VV (2019) Investigation on photocatalytic removal of NO under visible light over Cr-doped ZnO nanoparticles. ACS Omega 4:12853–12859. https://doi.org/10.1021/acsomega.9b01628
181. Xuan Sang N, Minh Quan N, Huu Tho N, Tri Tuan N, Thanh Tung T (2019) Mechanism of enhanced photocatalytic activity of Cr-doped ZnO nanoparticles revealed by photoluminescence emission and electron spin resonance. Semicond Sci Technol 34:025013
182. Shen L, Zhang Y-C, Huang Q (2011) Solvothermal synthesis of Cr-doped ZnO nanowires with visible light-driven photocatalytic activity. Mater Lett 65:1794–1796. https://doi.org/10.1016/j.matlet.2011.03.070
183. Chang C-J, Yang T-L, Weng Y-C (2014) Synthesis and characterization of Cr-doped ZnO nanorod-array photocatalysts with improved activity. J Solid State Chem 214:101–107. https://doi.org/10.1016/j.jssc.2013.09.039
184. Rokhsat E, Khayatian A (2018) Enhanced photocatalytic activity of Fe doped ZnO hierarchical nanosheets on the degradation of p-nitrophenol under visible light. Inorg Nano-Met Chem 48:203–209. https://doi.org/10.1080/24701556.2018.1505908
185. Bousslama W, Elhouichet H, Férid M (2017) Enhanced photocatalytic activity of Fe doped ZnO nanocrystals under sunlight irradiation. Optik 134:88–98. https://doi.org/10.1016/j.ijleo.2017.01.025
186. Liu L, Liu Z, Yang Y, Geng M, Zou Y, Shahzad MB, Dai Y, Qi Y (2018) Photocatalytic properties of Fe-doped ZnO electrospun nanofibers. Ceram Int 44:19998–20005. https://doi.org/10.1016/j.ceramint.2018.07.268
187. Satheesan MK, Baiju KV, Kumar V (2017) Influence of defects on the photocatalytic activity of Niobium-doped ZnO nanoparticles.

J Mater Sci Mater Electron 28:4719–4724. https://doi.org/10.1007/s10854-016-6114-9
188. 188. Rakesh, Ananda S, Gowda NMM, Raksha KR (2014) Synthesis of niobium doped ZnO nanoparticles by electrochemical method: Characterization, photodegradation of indigo carmine dye and antibacterial study. Advances in Nanoparticles 3:133–147. https://doi.org/10.4236/anp.2014.34018
189. Satpal SB, Athawale AA (2018) Synthesis of ZnO and Nd doped ZnO polyscales for removal of rhodamine 6G dye under UV light irradiation. Mater Res Express 5:085501
190. 190. Sutka A, Käämbre T, Pärna R, Juhnevica I, Maiorov M, Joost U, Kisand V (2016) Co doped ZnO nanowires as visible light photocatalysts. Solid State Sci 56:54–62. https://doi.org/10.1016/j.solidstatesciences.2016.04.008
191. Kuriakose S, Satpati B, Mohapatra S (2014) Enhanced photocatalytic activity of Co doped ZnO nanodisks and nanorods prepared by a facile wet chemical method. Phys Chem Chem Phys 16:12741–12749. https://doi.org/10.1039/C4CP01315H
192. Lu Y, Lin Y, Wang D, Wang L, Xie T, Jiang T (2011) A high performance cobalt-doped ZnO visible light photocatalyst and its photogenerated charge transfer properties. Nano Res 4:1144–1152. https://doi.org/10.1007/s12274-011-0163-4
193. Rehman S, Ullah R, Butt AM, Gohar ND (2009) Strategies of making TiO_2 and ZnO visible light active. J Hazard Mater 170:560–569. https://doi.org/10.1016/j.jhazmat.2009.05.064
194. Li W, Wang G, Chen C, Liao J, Li Z (2017) Enhanced visible light photocatalytic activity of ZnO nanowires doped with Mn2+ and Co2+ ions. Nanomaterials 7:20. https://doi.org/10.3390/nano7010020
195. Thennarasu G, Sivasamy A (2018) Mn doped ZnO nano material: a highly visible light active photocatalyst for environmental abatment. Inorg Nano-Met Chem 48:239–246. https://doi.org/10.1080/24701556.2018.1504073
196. Yang Y, Li Y, Zhu L, He H, Hu L, Huang J, Hu F, He B, Ye Z (2013) Shape control of colloidal Mn doped ZnO nanocrystals and their visible light photocatalytic properties. Nanoscale 5:10461–10471. https://doi.org/10.1039/C3NR03160H
197. Qiu X, Li L, Li G (2006) Nature of the abnormal band gap narrowing in highly crystalline $Zn_{1-x}Co_xO$ nanorods. Appl Phys Lett 88:114103. https://doi.org/10.1063/1.2185617
198. 198. Rodionovs P, Jankovica D, Grabis J (2019) Characteristics and photocatalytic activity of Sm doped ZnO nanoparticles. Key Eng Mater 799:179–184. https://doi.org/10.4028/www.scientific.net/KEM.799.179
199. 199. Sukriti, Chand P, Singh V (2020) Enhanced visible-light photocatalytic activity of samarium-doped zinc oxide nanostructures. J Rare Earths 38:29–38. https://doi.org/10.1016/j.jre.2019.02.009
200. Faraz M, Naqvi FK, Shakir M, Khare N (2018) Synthesis of samarium-doped zinc oxide nanoparticles with improved photocatalytic performance and recyclability under visible light irradiation. New J Chem 42:2295–2305. https://doi.org/10.1039/C7NJ03927A
201. Bhatia S, Verma N, Bedi RK (2016) Optical application of Er-doped ZnO nanoparticles for photodegradation of direct red − 31 dye. Opt Mater 62:392–398. https://doi.org/10.1016/j.optmat.2016.10.013
202. Divya NK, Pradyumnan PP (2016) Solid state synthesis of erbium doped ZnO with excellent photocatalytic activity and enhanced visible light emission. Mater Sci Semicond Proc 41:428–435. https://doi.org/10.1016/j.mssp.2015.10.004
203. Yu K-s, Shi J-y, Zhang Z-l, Liang Y-m, Liu W (2013) Synthesis, characterization, and photocatalysis of ZnO and Er-doped ZnO. J Nanomater 2013:372951. https://doi.org/10.1155/2013/372951
204. Kumar S, Sahare PD (2012) Nd-doped ZnO as a multifunctional nanomaterial. J Rare Earths 30:761–768. https://doi.org/10.1016/S1002-0721(12)60126-4
205. Zhao Z, Song J-l, Zheng J-h, Lian J-s (2014) Optical properties and photocatalytic activity of Nd-doped ZnO powders. Trans Nonferrous Met Soc China 24:1434–1439. https://doi.org/10.1016/S1003-6326(14)63209-X
206. Zhang J, Deng S, Liu S, Chen J, Han B, Wang Y, Wang Y (2014) Preparation and photocatalytic activity of Nd doped ZnO nanoparticles. Mater Technol 29:262–268. https://doi.org/10.1179/1753555713Y.0000000122
207. Kumar R, Umar A, Kumar G, Akhtar MS, Wang Y, Kim SH (2015) Ce-doped ZnO nanoparticles for efficient photocatalytic degradation of direct red-23 dye. Ceram Int 41:7773–7782. https://doi.org/10.1016/j.ceramint.2015.02.110
208. Ahmad M, Ahmed E, Zafar F, Khalid NR, Niaz NA, Hafeez A, Ikram M, Khan MA, Hong Z (2015) Enhanced photocatalytic activity of Ce-doped ZnO nanopowders synthesized by combustion method. J Rare Earths 33:255–262. https://doi.org/10.1016/S1002-0721(14)60412-9
209. Faisal M, Ismail A, Ibrahim A, Bouzid H, Al-Sayari S (2013) Highly efficient photocatalyst based on Ce doped ZnO nanorods: controllable synthesis and enhanced photocatalytic activity. Chem Eng J 229:225–233. https://doi.org/10.1016/j.cej.2013.06.004
210. 210. Aisah N, Gustiono D, Fauzia V, Sugihartono I, Nuryadi R (2017) Synthesis and enhanced photocatalytic activity of Ce-doped zinc oxide nanorods by hydrothermal method. IOP Conf Ser: Mater Sci Eng 172:012037.
211. Pascariu P, Homocianu M, Cojocaru C, Samoila P, Airinei A, Suchea M (2019) Preparation of La doped ZnO ceramic nanostructures by electrospinning–calcination method: effect of La^{3+} doping on optical and photocatalytic properties. Appl Surf Sci 476:16–27. https://doi.org/10.1016/j.apsusc.2019.01.077
212. Sordello F, Berruti I, Gionco C, Paganini MC, Calza P, Minero C (2019) Photocatalytic performances of rare earth element-doped zinc oxide toward pollutant abatement in water and wastewater. Appl Catal B: Environ Energy 245:159–166. https://doi.org/10.1016/j.apcatb.2018.12.053
213. Ahmad I, Akhtar MS, Ahmed E, Ahmad M (2020) Facile synthesis of Pr-doped ZnO photocatalyst using sol–gel method and its visible light photocatalytic activity. J Mater Sci: Mater Electron 31:1084–1093. https://doi.org/10.1007/s10854-019-02620-2
214. Vaiano V, Matarangolo M, Sacco O, Sannino D (2017) Photocatalytic treatment of aqueous solutions at high dye concentration using praseodymium-doped ZnO catalysts. Appl Catal B: Environ Energy 209:621–630. https://doi.org/10.1016/j.apcatb.2017.03.015
215. Chen J-L, Devi N, Li N, Fu D-J, Ke X-W (2018) Synthesis of Pr-doped ZnO nanoparticles: their structural, optical, and photocatalytic properties. Chin Phys B 27:086102
216. Alam U, Khan A, Ali D, Bahnemann D, Muneer M (2018) Comparative photocatalytic activity of sol–gel derived rare earth metal (La, Nd, Sm and Dy)-doped ZnO photocatalysts for degradation of dyes. RSC Adv 8:17582–17594. https://doi.org/10.1039/C8RA01638K
217. Khataee A, Darvishi Cheshmeh Soltani R, Hanifehpour Y, Safarpour M, Gholipour Ranjbar H, Joo SW (2014) Synthesis and characterization of dysprosium-doped ZnO nanoparticles for photocatalysis of a textile dye under visible light irradiation. Ind Eng Chem Res 53:1924–1932. https://doi.org/10.1021/ie402743u
218. Sanchez Rayes RM, Kumar Y, Cortes-Jácome MA, Toledo Antonio JA, Mathew X, Mathews NR (2017) Effect of Eu doping on the physical, photoluminescence, and photocatalytic characteristics of ZnO thin films grown by sol–gel method. physica status solidi (a) 214:1700229. https://doi.org/10.1002/pssa.201700229

219. Luo LC, Zhu L, Wang X (2015) Study on Eu doped ZnO photocatalytic degradation of pharmaceutical wastewater. Appl Mech Mater 700:482–486. https://doi.org/10.4028/www.scientific.net/AMM.700.482
220. Phuruangrat A, Yayapao O, Thongtem T, Thongtem S (2014) Synthesis and characterization of europium-doped zinc oxide photocatalyst. J Nanomater 2014:367529. https://doi.org/10.1155/2014/367529
221. Yousefi M, Amiri M, Azimirad R, Moshfegh AZ (2011) Enhanced photoelectrochemical activity of Ce doped ZnO nanocomposite thin films under visible light. J Electroanal Chem 661:106–112. https://doi.org/10.1016/j.jelechem.2011.07.022
222. Pascariu P, Cojocaru C, Olaru N, Samoila P, Airinei A, Ignat M, Sacarescu L, Timpu D (2019) Novel rare earth (RE-La, Er, Sm) metal doped ZnO photocatalysts for degradation of congo-red dye: synthesis, characterization and kinetic studies. J Environ Manag 239:225–234. https://doi.org/10.1016/j.jenvman.2019.03.060
223. Ba-Abbad MM, Takriff MS, Benamor A, Nasser MS, Mahmoudi E, Mohammad AW (2018) Synthesis and characterization of Sm^{3+}-doped ZnO nanoparticles via a sol–gel method and their photocatalytic application. J Sol-Gel Sci Technol 85:178–190. https://doi.org/10.1007/s10971-017-4503-z
224. Mandor H, Amin NK, Abdelwahab O, El-Ashtoukhy E-S (2022) Preparation and characterization of N-doped ZnO and N-doped TiO_2 beads for photocatalytic degradation of phenol and ammonia. Environ Sci Pollut Res 29:56845–56862. https://doi.org/10.1007/s11356-022-19421-6
225. Karakaya S, Kaba L (2024) Effect of fluorine doping on the improvement of electrical and photocatalytic properties of ZnO films. Appl Phys A 130:167. https://doi.org/10.1007/s00339-024-07312-1
226. Luu TVH, Tho NTM, Thuy TTT, Thong LN, Dung NT, Dang PH (2024) Synthetization pill-like C-doped ZnO nano-photocatalyst for removing ofloxacin and methylene blue under visible light. J Sol-Gel Sci Technol 110:204–220. https://doi.org/10.1007/s10971-024-06348-2
227. Ng Z-N, Chan K-Y, Muslimin S, Knipp D (2018) P-type characteristic of nitrogen-doped ZnO films. J Electron Mater 47:5607–5613. https://doi.org/10.1007/s11664-018-6468-2
228. Yu Z, Yin L-C, Xie Y, Liu G, Ma X, Cheng H-M (2013) Crystallinity-dependent substitutional nitrogen doping in ZnO and its improved visible light photocatalytic activity. J Colloid Interface Sci 400:18–23. https://doi.org/10.1016/j.jcis.2013.02.046
229. Peter CN, Anku WW, Sharma R, Joshi GM, Shukla SK, Govender PP (2019) N-doped ZnO/graphene oxide: a photostable photocatalyst for improved mineralization and photodegradation of organic dye under visible light. Ionics 25:327–339. https://doi.org/10.1007/s11581-018-2571-x
230. 230. Ayu DG, Gea S, Andriayani, Telaumbanua DJ, Piliang AFR, Harahap M, Yen Z, Goei R, Tok AIY (2023) Photocatalytic degradation of methylene blue using N-doped ZnO/carbon dot (N-ZnO/CD) nanocomposites derived from organic soybean. ACS Omega 8:14965–14984. https://doi.org/10.1021/acsomega.2c07546
231. Sacco O, Mancuso A, Venditto V, Pragliola S, Vaiano V (2022) Behavior of N-doped TiO_2 and N-doped ZnO in photocatalytic azo dye degradation under UV and visible light irradiation: a preliminary investigation. Catalysts 12:1208. https://doi.org/10.3390/catal12101208
232. Pigosso T, Melo BAA, Evangelista LL, Gómez González SY, Binder C (2023) Rapid synthesis of in situ nitrogen-doped ZnO nanoparticles for visible-light-driven photocatalytic removal of emerging contaminants. Mater Today Chem 33:101753. https://doi.org/10.1016/j.mtchem.2023.101753
233. Prabakaran E, Pillay K (2019) Synthesis of N-doped ZnO nanoparticles with cabbage morphology as a catalyst for the efficient photocatalytic degradation of methylene blue under UV and visible light. RSC Adv 9:7509–7535. https://doi.org/10.1039/C8RA09962F
234. Suykens JAK, Vandewalle J (1999) Least squares support vector machine classifiers. Neural Process Lett 9:293–300. https://doi.org/10.1023/A:1018628609742
235. Eslamimanesh A, Gharagheizi F, Illbeigi M, Mohammadi AH, Fazlali A, Richon D (2012) Phase equilibrium modeling of clathrate hydrates of methane, carbon dioxide, nitrogen, and hydrogen+water soluble organic promoters using Support Vector Machine algorithm. Fluid Phase Equilib 316:34–45. https://doi.org/10.1016/j.fluid.2011.11.029
236. Eslamimanesh A, Gharagheizi F, Mohammadi AH, Richon D (2011) Phase equilibrium modeling of structure H clathrate hydrates of methane + water "insoluble" hydrocarbon promoter using QSPR molecular approach. J Chem Eng Data 56:3775–3793. https://doi.org/10.1021/je200444f
237. Gharagheizi F, Eslamimanesh A, Farjood F, Mohammadi AH, Richon D (2011) Solubility parameters of nonelectrolyte organic compounds: determination using quantitative structure–property relationship strategy. Ind Eng Chem Res 50:11382–11395. https://doi.org/10.1021/ie200962w
238. 238. Pelckmans K, Suykens J, Van Gestel T, De Brabanter J, Lukas L, Hamers B, De Moor B, Vandewalle J (2002) LS-SVMlab: a Matlab/C toolbox for Least Squares Support Vector Machines. Internal Report ESAT-SISTA
239. Xavier-de-Souza S, Suykens JAK, Vandewalle J, Bolle D (2010) Coupled simulated annealing. IEEE Trans Syst Man Cybern B (Cybern) 40:320–335
240. Elmaz F, Yücel Ö, Mutlu AY (2020) Predictive modeling of biomass gasification with machine learning-based regression methods. Energy 191:116541. https://doi.org/10.1016/j.energy.2019.116541
241. Geurts P, Irrthum A, Wehenkel L (2009) Supervised learning with decision tree-based methods in computational and systems biology. Mol Biosyst 5:1593–1605. https://doi.org/10.1039/B907946G
242. Wang Y, Liao Z, Mathieu S, Bin F, Tu X (2021) Prediction and evaluation of plasma arc reforming of naphthalene using a hybrid machine learning model. J Hazard Mater 404:123965. https://doi.org/10.1016/j.jhazmat.2020.123965
243. 243. Liaw A, Wiener M (2002) Classification and regression by randomforest. R News 2/3:18–22.
244. Wu L, Huang G, Fan J, Zhang F, Wang X, Zeng W (2019) Potential of kernel-based nonlinear extension of Arps decline model and gradient boosting with categorical features support for predicting daily global solar radiation in humid regions. Energy Convers Manag 183:280–295. https://doi.org/10.1016/j.enconman.2018.12.103
245. Wu LF, Li N, Zhao T (2019) Using the seasonal FGM(1,1) model to predict the air quality indicators in Xingtai and Handan. Environ Sci Pollut Res 26:14683–14688. https://doi.org/10.1007/s11356-019-04715-z
246. Breiman L (2001) Random forests. Mach Learn 45:5–32. https://doi.org/10.1023/A:1010933404324
247. 247. Chen T, Guestrin C (2016) XGBoost: A scalable tree boosting system. Proceedings of the 22nd ACM SIGKDD International Conference on Knowledge Discovery and Data Mining Association for Computing Machinery, San Francisco, California, USA, pp. 785–794.
248. Jerome HF (2001) Greedy function approximation: a gradient boosting machine. Ann Stat 29:1189–1232. https://doi.org/10.1214/aos/1013203451

249. 249. Chen T, He T, Benesty M, Khotilovich V, Tang Y, Cho H, Chen K, Mitchell R, Cano I, Zhou T (2015) Xgboost: Extreme gradient boosting. R package version 0.4-2 1:1–4.
250. Natekin A, Knoll A (2013) Gradient boosting machines, a tutorial. Front Neurorobot 7:21. https://doi.org/10.3389/fnbot.2013.00021
251. Asadi Shamsabadi E, Salehpour M, Zandifaez P, Dias-da-Costa D (2023) Data-driven multicollinearity-aware multi-objective optimisation of green concrete mixes. J Clean Prod 390:136103. https://doi.org/10.1016/j.jclepro.2023.136103
252. 252. Lundberg SM, Lee S-I (2017) A unified approach to interpreting model predictions. Proceedings of the 31st International Conference on Neural Information Processing Systems Curran Associates Inc., Long Beach, California, USA, pp. 4768–4777.
253. Feng L, Zhu J, Jiang Z (2024) Numerical investigation of carbon dioxide capture using nanofluids via machine learning. J Clean Prod 450:141916. https://doi.org/10.1016/j.jclepro.2024.141916
254. Wu J, Chen X-Y, Zhang H, Xiong L-D, Lei H, Deng S-H (2019) Hyperparameter optimization for machine learning models based on bayesian optimization. J Electron Sci Technol 17:26–40. https://doi.org/10.11989/JEST.1674-862X.80904120
255. Shafqat W, Malik S, Lee K-T, Kim D-H (2021) PSO based optimized ensemble learning and feature selection approach for efficient energy forecast. Electronics 10:2188. https://doi.org/10.3390/electronics10182188
256. Kennedy J (2010) Particle Swarm Optimization. In: Sammut C, Webb GI (eds) Encyclopedia of Machine Learning. Springer US, Boston, MA, pp 760–766
257. Pavel M, Anastasescu C, State R-N, Vasile A, Papa F, Balint I (2023) Photocatalytic degradation of organic and inorganic pollutants to harmless end products: assessment of practical application potential for water and air cleaning. Catalysts 13:380. https://doi.org/10.3390/catal13020380
258. Gamelas SRD, Tomé JPC, Tomé AC, Lourenço LMO (2023) Advances in photocatalytic degradation of organic pollutants in wastewaters: harnessing the power of phthalocyanines and phthalocyanine-containing materials. RSC Adv 13:33957–33993. https://doi.org/10.1039/D3RA06598G
259. Kumar A, Pandey G (2017) A review on the factors affecting the photocatalytic degradation of hazardous materials. Mater Sci Eng Int J 1:106–114
260. Le AT, Samsuddin NSB, Chiam S-L, Pung S-Y (2021) Synergistic effect of pH solution and photocorrosion of ZnO particles on the photocatalytic degradation of Rhodamine B. Bull Mater Sci 44:5. https://doi.org/10.1007/s12034-020-02281-6
261. Baig A, Siddique M, Panchal S (2025) A review of visible-light-active zinc oxide photocatalysts for environmental application. Catalysts 15:100. https://doi.org/10.3390/catal15020100